

Oil & Natural Gas Technology

Detection and Production of Methane Hydrate

Semi-annual Progress Report

Reporting Period: April-September, 2010

Submitted by:

Rice University, University of Texas, and Oklahoma State University

George J. Hirasaki and Walter Chapman, Chemical and Biomolecular Engineering
Gerald R. Dickens, Colin A. Zelt, and Brandon E. Dugan, Earth Science
Kishore K. Mohanty, University of Texas
Priyank Jaiswal, Oklahoma State University

November, 2010

DOE Award No.: DE-FC26-06NT42960
John Terneus, Program Officer

Rice University – MS 362
6100 Main St.
Houston, TX 77251-1892
Phone: 713-348-5416; FAX: 713-348-5478; Email: gjh@rice.edu

Prepared for:
United States Department of Energy
National Energy Technology Laboratory



Office of Fossil Energy

Table of Contents

Disclaimer	4
Executive Summary	5
Background.....	8
A. Objective	8
B. Scope of Work	8
Task 6: Numerical Models for Quantification of Hydrate and Free Gas Accumulations.....	9
Subtask 6.3. Compositional Effect on BSR, Synthetic Seismic Response	9
Subtask 6.4. Blanking and chaotic zones due to hydrate distribution.....	14
Subtask 6.6: Concentrated hydrate and free gas	20
Conference abstracts	49
Task 7: Analysis of Production Strategy	51
Results	51
Horizontal reservoir.....	51
Dipping reservoirs	56
Task 8: Seafloor and Borehole Stability	62
Summary	62
Milestone Status.....	62
Subtask 8.2: Modeling (In)stability.....	62
Results	65
Conclusions.....	67
Ongoing and future work	67
Presentations and Abstracts	68
Publications.....	68
References.....	68
Task 9.0: Geophysical Imaging.....	79
Milestone Chart	79
Summary	79
Study Area	80
Observation in wells 10D, 12A, and 13A	80
Traveltime Inversion and Pre-Stack Depth Migration	80
Waveform Inversion	85

Ongoing work	88
References	89
COST PLAN / STATUS	90
Milestone Plan/Status	91

Disclaimer

This report was prepared as an account of work sponsored by an agency of the United States Government. Neither the United States Government nor any agency thereof, nor any of their employees, makes any warranty, express or implied, or assumes any legal liability or responsibility for the accuracy, completeness, or usefulness of any information, apparatus, product, or process disclosed, or represents that its use would not infringe privately owned rights. Reference herein to any specific commercial product, process, or service by trade name, trademark, manufacturer, or otherwise does not necessarily constitute or imply its endorsement, recommendation, or favoring by the United States Government or any agency thereof. The views and opinions of authors expressed herein do not necessarily state or reflect those of the United States Government or any agency thereof.

Executive Summary

Task 6: Numerical Models for Quantification of Hydrate and Free Gas Accumulations

Subtask 6.3, Compositional Effect on BSR. Data show that a thick transition zone, where saturations vary gradually, is not unique only in the previous reported case where the overall water-free propane molar fraction is constant, but common in different cases with different compositional gradients. Especially in Case II (see Section 6.3.), which is more reasonable in real geological settings, the saturation profiles vary smoothly in the transition zone, which is around 300m in thickness. Even in the worst case, Case III (see Section 6.3.), where propane is depleted in shallower sediment, the transition zone is still as thick as 200m. So these data further confirm our hypothesis that compositional effect may induce gradual change of saturations in a thick transition zone.

Subtask 6.4. Blanking and chaotic zones due to hydrate distribution. Our study indicates that hydrate accumulation does not guarantee a blanking zone, and the blanking zone does not mean hydrate accumulates, neither. Only in limited parameter space, the blanking zone can be regarded due to hydrate accumulation.

Subtask 6.6: Concentrated hydrate and free gas. We develop numerical models to simulate gas hydrate and free gas accumulation in lithologically heterogeneous marine sediments over geologic time scales. Simulations with a vertical fracture network, which extends through the gas hydrate stability zone and has permeability 100 times greater than the surrounding shale, show that focused fluid flow causes higher hydrate (20-30%) and free gas saturation (40-50%) within the fracture network compared to the surrounding, lower permeability shale. Systems with dipping, high permeability sand layers also show localized, elevated saturations of hydrate and free gas within the high permeability conduits. Permeability anisotropy, with a ratio of vertical to horizontal permeability (order of 10^{-2}) show even higher hydrate concentrations within the high permeability conduits because anisotropy focuses more methane-charged fluid into the high permeability conduits. These 2-D, heterogeneous models quantify how focused fluid flow through high permeability zones affects regional and local hydrate accumulation and saturation. Simulations are being extended with specified fluid flux and methane input from deeper sources, which allows comparison of local methanogenesis and deeper methane sources on flow pathways and hydrate/free gas accumulation. We show that increased fluid flux from external sources would result in enhanced concentrations of hydrate and free gas. This builds on our previous one-dimensional work that shows hydrate saturation is dependent on Peclet number, the ratio of advective flux to the diffusive flux of methane. In our two-dimensional work, we show it is the local advective flux relative to diffusion (local Peclet number) that influences the hydrate and free gas saturation. We relate average local Peclet numbers and

average hydrate flux ($Pe_1 < S_h >$) within high permeability conduits which compare favorably with our previously published 1-D results.

Task 7: Analysis of Production Strategy

In previous studies, we have shown that depressurization is ineffective in unconfined reservoirs; horizontal wells are more effective than vertical wells. In this study, we consider reservoirs with a limited aquifer. We assume that the unconfined of the aquifer is not at the bottom but on one side of the aquifer. For the limited aquifer case we study only horizontal wells, and that makes the reservoir translationally symmetric. So, for this case we study the reservoir in 2 dimensions but the total amount of hydrates and hydrate to water ratio are same as in our previous case of unconfined reservoir. The initial conditions and rock properties are the same as in the previous case. The injection well conditions are also same with injection pressure of 50MPa, and injection temperature of 50°C. Production well pressure is 4MPa. Circle shows the producer and X shows the injector in the figures.

Task 8: Seafloor and Borehole Stability

Our efforts have been entirely on Subtask 8.2: Sediment (In)Stability. The two-dimensional geological accumulations models (Task 6) include stability calculations and we are ready to begin simulating the general conditions for failure and apply them to field cases. We have benchmarked our 2D accumulations against 1D solutions, so a parameter study on stability is the next step. Our advancements on instability have isolated the effects of fracturing on hydrate accumulation via 1D models based on fluid flux, multi-phase fluid flow, sediment properties (Subtask 8.1). We are now looking at transient effects of fracturing and will soon start looking at how fracturing mechanisms may contribute to geophysical anomalies because of their effects on heterogeneous hydrate accumulations. We continue to collaborate with colleagues, especially those with field data, to allow integration of our models with field studies (Subtask 8.3). This includes collaborations with the University of Texas at Austin Institute for Geophysics (UTIG) in an effort to understand transient fluid flow, instability, and gas discharge at Hydrate Ridge and with the University of Victoria and Geological Survey of Canada to look at hydrate-related failures (Lopez slide, Slipstream slide) at Cascadia.

Task 9: Geophysical Imaging of Gas Hydrate and Free Gas Accumulations

We have performed full-waveform inversion in this period. Although we had completed traveltimes inversion and depth migration in Year 1, we found it necessary to revisit the model and re-create it with 20% more traveltimes picks to improve its overall resolution. The resolution improvement enabled us to a) reconcile observations in three wells that were drilled near the seismic line; and b) start the waveform inversion from the lowest usable frequency of 8 Hz. The waveform inversion was implemented in frequency domain. Five groups of frequencies, each group comprising 3 frequencies separated by 0.4 Hz, were

inverted beginning from 8Hz up to 15Hz. In an ongoing study, the preferred waveform model is being assessed using checkerboard tests and their overall geological sensibility. For interpretation purposes velocities within the hydrate stability zone are considered proportional to hydrate concentration; higher velocities imply higher hydrate concentration. The preferred waveform model show lateral velocity variation within the hydrate stability zone probably due to variation in hydrate concentration. A combination of waveform model and depth image indicates that in parts of model that have structural discontinuities, hydrates may have a preferred orientation. The reasons for a preferred orientation are currently unknown and under investigation.

Background

A. Objective

This project seeks to understand regional differences in gas hydrate systems from the perspective of as an energy resource, geohazard, and long-term climate influence. Specifically, the effort will: (1) collect data and conceptual models that targets causes of gas hydrate variance, (2) construct numerical models that explain and predict regional-scale gas hydrate differences in 2- and 3-dimensions with minimal “free parameters”, (3) simulate hydrocarbon production from various gas hydrate systems to establish promising resource characteristics, (4) perturb different gas hydrate systems to assess potential impacts of hot fluids on seafloor stability and well stability, and (5) develop geophysical approaches that enable remote quantification of gas hydrate heterogeneities so that they can be characterized with minimal costly drilling. Our integrated program takes advantage of the fact that we have a close working team comprised of experts in distinct disciplines.

The expected outcomes of this project are improved exploration and production technology for production of natural gas from methane hydrates and improved safety through understanding of seafloor and well bore stability in the presence of hydrates.

B. Scope of Work

The scope of this project is to more fully characterize, understand, and appreciate fundamental differences in the amount and distribution of gas hydrate and how this affects the production potential of a hydrate accumulation in the marine environment. The effort will combine existing information from locations in the ocean that are dominated by low permeability sediments with small amounts of high permeability sediments, one permafrost location where extensive hydrates exist in reservoir quality rocks and other locations deemed by mutual agreement of DOE and Rice to be appropriate. The initial ocean locations are Blake Ridge, Hydrate Ridge, Peru Margin and GOM. The permafrost location is Mallik. Although the ultimate goal of the project is to understand processes that control production potential of hydrates in marine settings, Mallik will be included because of the extensive data collected in a producible hydrate accumulation. To date, such a location has not been studied in the oceanic environment. The project will work closely with ongoing projects (e.g. GOM JIP and offshore India) that are actively investigating potentially economic hydrate accumulations in marine settings.

The overall approach is fivefold: (1) collect key data concerning hydrocarbon fluxes which is currently missing at all locations to be included in the study, (2) use this and existing data to build numerical models that can explain gas hydrate variance at all four locations, (3) simulate how natural gas could be produced from each location with different production strategies, (4) collect new sediment property data at these locations that are required for constraining fluxes, production simulations and assessing sediment stability, and (5) develop a method for remotely quantifying heterogeneities in gas hydrate and free gas distributions. While we generally restrict our efforts to the locations where key parameters can be measured or constrained, our ultimate aim is to make our efforts universally applicable to any hydrate accumulation.

Task 6: Numerical Models for Quantification of Hydrate and Free Gas Accumulations

Subtask 6.3. Compositional Effect on BSR, Synthetic Seismic Response *Guangsheng Gu*

(1) Hydrate/Gas distribution with different compositional gradients in CH₄-C₃H₈-H₂O hydrate system

From the work we have finished, we can find out existence of another gas component in marine hydrate system, can affect the hydrate and gas distribution greatly. In a CH₄-C₃H₈-H₂O hydrate system, by assuming a constant water-free C₃H₈ fraction at 5%, there can exist a transition region in which Aq, H (sII) and V can co-exist, and S_H and S_V can change gradually. The transition zone can be as thick as 300 m.

However, whether this scenario still appears in some other profiles of water-free C₃H₈ fraction, is also very important to this study. We performed simulation with some other profiles.

We devised the following situation. We have several ideal cases, for the physical condition, we assume the following:

Seafloor pressure: $P_{sf} = 5 \text{ MPa}$;
Seafloor Temperature: $T_{sf} = 276.15 \text{ K}$;
Geothermal gradient = 0.04 K/m ;

We assume a water composition of 98% in mole ratio, the rest 2% is methane-propane mixture. Salinity is not considered.

Within that frame, we devised three idea cases:

Case I: Water-free mole fraction of methane remains constant (methane: 95%, propane:5%) everywhere.

Case II: Water-free mole fraction of propane increases from 0 to 5%, varying uniformly with respect to depth.

Case III: Water-free mole fraction of propane decreases from 5% to 0, varying uniformly with respect to depth.

Case II is more reasonable in real geological sites because propane is more possible from thermogenic gas sources which come below the BHSZ, and propane may be depleted when passing through the HSZ where sII hydrate will form to absorb propane. Case I and III are used for comparison purpose.

Extracting the phase fraction and molar ratio from the flash result we calculated saturation profile of different phase with respect to depth. And the diagrams are attached as the following.

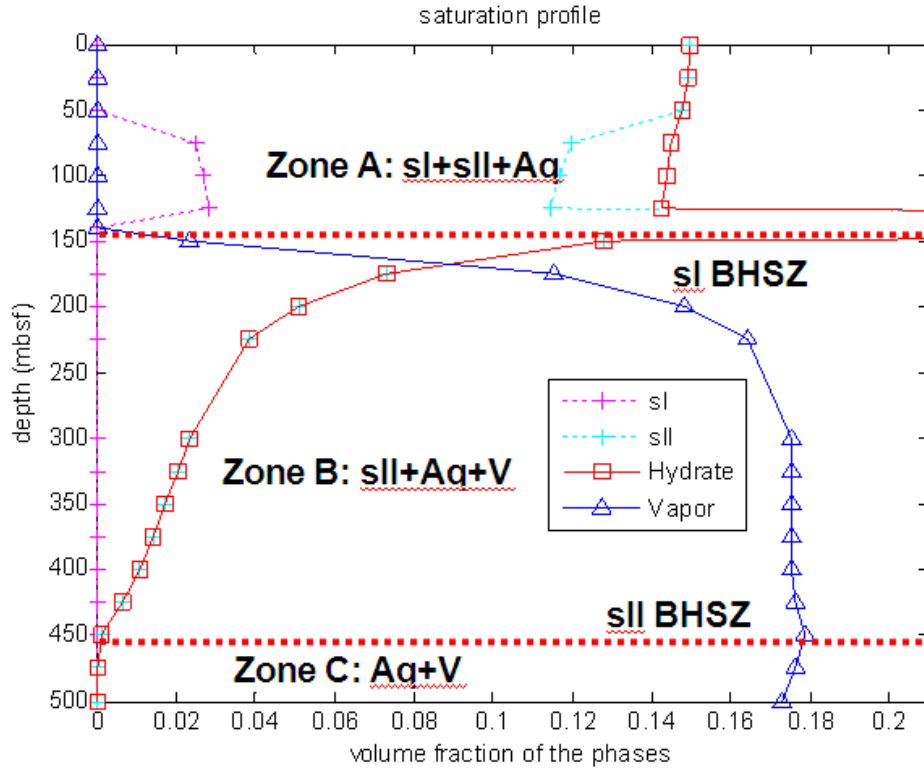


Figure 6.3.1. An example calculation of a CH₄-C₃H₈-H₂O System, Case I, with constant overall composition everywhere (water-free propane molar fraction is 5% everywhere; Overall composition $x_{CH_4} + x_{C_3H_8} = 0.02$, $x_{H_2O} = 0.98$). Zone B is the transition zone.

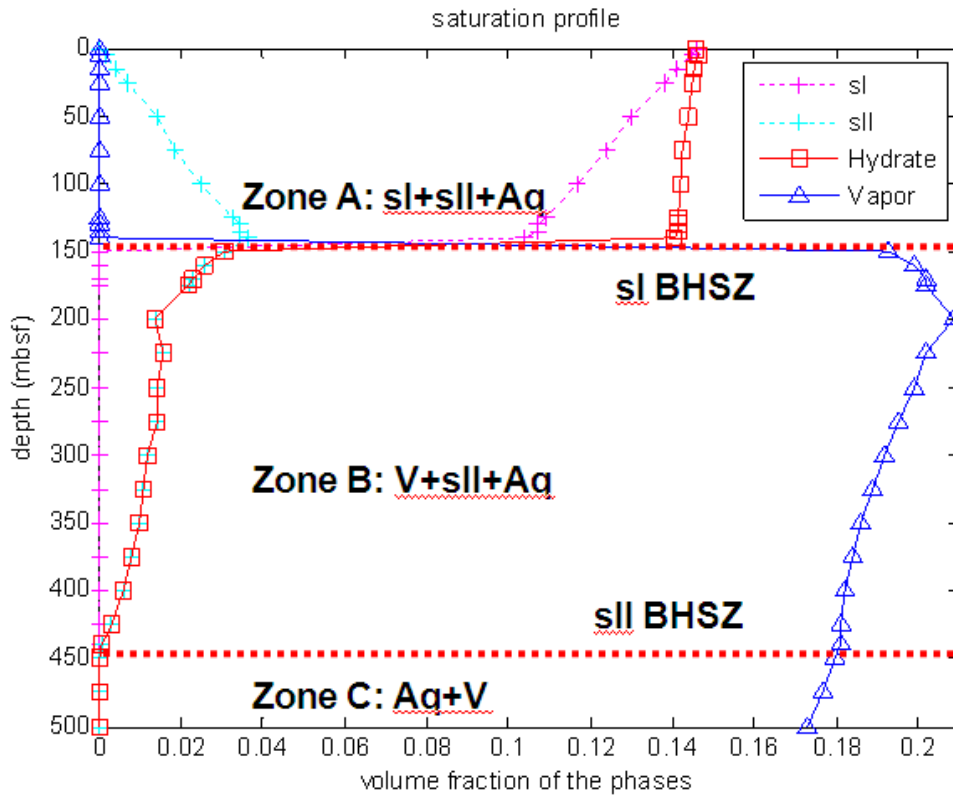


Figure 6.3.2. An example calculation of a CH_4 - C_3H_8 - H_2O System, Case II, with increasing water-free fraction of propane (water-free propane molar fraction increases from 0 to 5% linearly from 0 to 500 mbsf; Overall composition $x_{CH_4} + x_{C_3H_8} = 0.02$, $x_{H_2O} = 0.98$). Zone B is the transition zone.

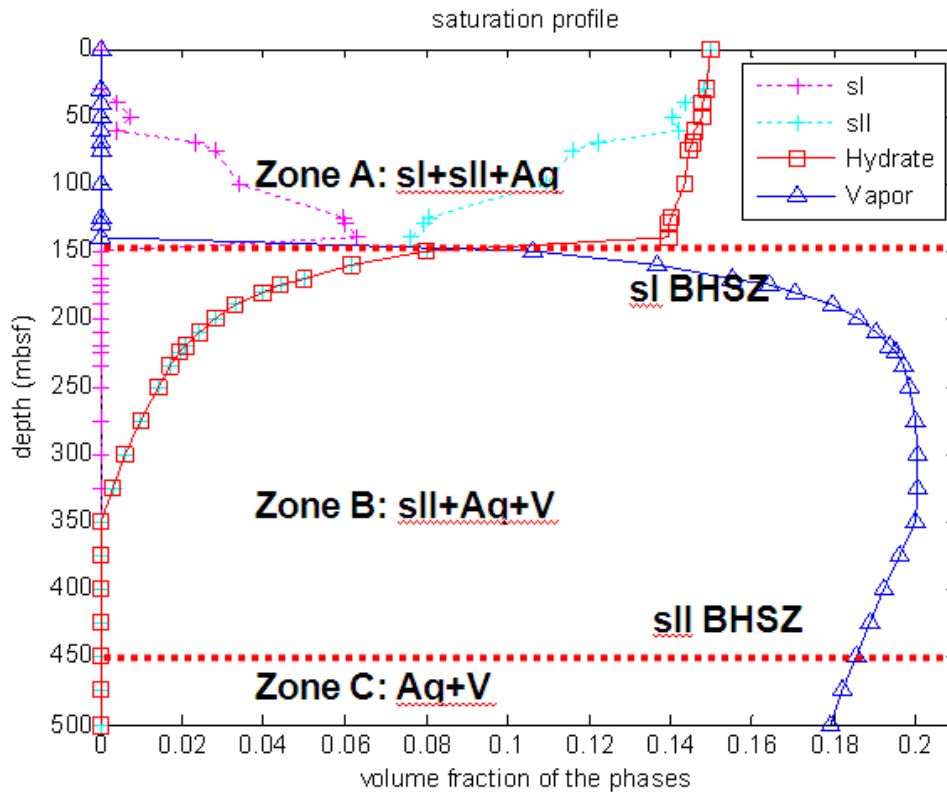


Figure 6.3.3. An example calculation of a $\text{CH}_4\text{-C}_3\text{H}_8\text{-H}_2\text{O}$ System, Case III, with decreasing water-free fraction of propane (water-free propane molar fraction decreases from 5% to 0 linearly from 0 to 500 mbsf; Overall composition $x_{\text{CH}_4} + x_{\text{C}_3\text{H}_8} = 0.02$, $x_{\text{H}_2\text{O}} = 0.98$). Zone B is the transition zone.

The red, dotted lines indicate the Base of Hydrate Stability Zone (for sl or slI as marked in figures). We noticed from the graph that the three lines from the three graphs take place at the same depth. Therefore we have reached that the Base of Hydrate Stability Line is a thermodynamic property, which only depends on temperature and pressure while it is compositional-free.

The transition appears to happen a lot shallower in the third graph, where on the graph it seems like the upper boundary of Zone C appears as shallow as 350 mbsf. However, it is probably because of the lack of propane that contributes to the early depletion of the methane. However thermodynamically, the transition of the three diagrams should happen at the same depth.

We have seen similar patterns of zone distribution, first we have a zone where structure I hydrate and structure II hydrate coexist, then we move onto the transitional zone where structure II hydrate and Vapor are both present, and eventually we move onto the region where only Vapor is present. The curve within each zone is always smooth as we have smooth variations of all the

variables. Inconsistency only occurs when Zone transition happens when we have a sudden disappearance of a phase.

Data in these figures show that the thick transition zone (Zone B) is not unique only in Case I, but common in different cases with different compositional gradients. Especially in Case II, which is more reasonable in real geological settings, the saturation profiles vary smoothly in the transition zone, which is around 300m in thickness. Even in the worst case, Case III, where propane is depleted in shallower sediment, the transition zone is still as thick as 200m. So these data further confirm our hypothesis that compositional effect may induce gradual change of saturations in a thick transition zone.

Subtask 6.4. Blanking and chaotic zones due to hydrate distribution.

Guangsheng Gu

(1) Sediment Acoustic impedance analysis:

We have started working on acoustic velocity profiles in different types of sediment layers. Due to hydrate accumulation, the velocity in different types of sediment layers can become similar with each other.

Geological settings:

We set several horizontal layers with different properties, from seafloor to deeper sediment. These layers are in 2 types: sandstone or clay/shale. Sandstone layers have higher porosity (20%~30%), and shale layers with some porosity values varying with depth. Assume hydrate saturation increases gradually. Then we estimated the Vp density, and seismic impedance profiles of these two different types of layers, and made comparison between them.

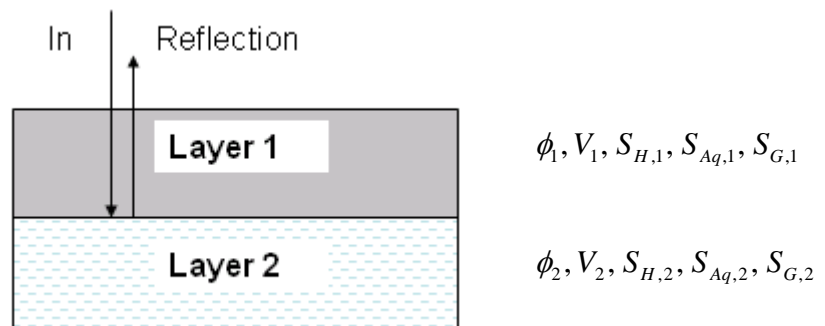


Figure 6.4.1. Geological Setting

Two layers, with different acoustic properties and saturations. Assign the Layer 1 as sand layer, and Layer 2 as shale (clay) layer.

Parameters:

Table 6.4.1: Acoustic properties of components

Component	Vp (m/s)	ρ (kg/m ³)
Sea Water (w)	1500	1030
Hydrate (H)	3300	900
Mineral1 (m1, sandstone)	2000~4000	2500
Mineral2 (m2, shale)	2400	2600

Table 6.4.2: other parameters

Parameter	Value	
Porosity1 (in sandstone layer)	0.2 ~ 0.3	
Porosity2 (in shale layer)	Up: 0.6; Low: 0.2~0.4	
Sh	0~1	

The ranges of porosity were obtained from Hirasaki (lecture note, 2006), Jenyon (2006), Magara (1980); and those of acoustic velocities from W.J. Winters and W.F. Waite (2007).

Equations:

Estimation of average velocity is via a revised form of the Time-average Equation (Pearson *et al.*, 1983):

$$\frac{1}{V_p} = \frac{\phi(1 - S_H - S_V)}{V_w} + \frac{\phi S_H}{V_H} + \frac{(1 - \phi)}{V_m} + \frac{\phi S_V}{V_V}$$

V_p --- average compressional velocity of the sediment;

V_H --- compressional velocity of the pure hydrate;

V_w --- compressional velocity of the fluid;

V_m --- compressional velocity of the mineral;

ϕ --- porosity (as a fraction);

S_H --- Hydrate saturation

S_V --- Vapor (Gas) saturation

Average density is estimated via:

$$\bar{\rho} = (1 - \phi)\rho_m + \phi \sum_i S_i \rho_i$$

phase $i = w, H, V$.

Impedance is: $Z = \rho V_p$

Result:

Our study indicates that hydrate accumulation does not guarantee a blanking zone, and the blanking zone does not mean hydrate accumulates,

neither. Only in limited parameter space, the blanking zone can be regarded due to hydrate accumulation.

Figure 6.4.2 shows an example where hydrate accumulation induces seismic blanking zone. The acoustic impedance of sand layer, at $S_h=0$, is possible to be lower than that of a shale layer; therefore when hydrate saturation S_h increases, it's possible for impedance of sand layer to increase to higher values than that of a shale layer. In these situations, it's possible that a blanking can be achieved during the hydrate accumulation process.

However, this situation is heavily dependent on the parameters applied. These parameters include but not limited to: the intrinsic (i.e., without hydrate, water, or gas) velocity in sand layer, V_{p_sand} , and that in shale (clay) layer, V_{p_clay} , and also the porosities in these layer will contribute much to the seismic impedance contrast.

For example, if the parameters change a little bit, from those listed in Figure 6.4.3, to those listed in Figure 6.4.4., the $V_{p_sand}=2000$ m/s changed to 2500 m/s, then the average impedance in sand layer, Z_{sand} , will be higher than that in shale (clay) layer, Z_{clay} , only except that at $S_{h,sand}=0$. This situation means that the seismic blanking will only happen when there is no hydrate in sand layer. So it's called a blanking - just-happen case.

What's more, in Figure 6.4.5. comparing with Figure 6.4.4., the porosity of clay layer changed from $\phi_2=0.3$ to $\phi_2=0.2$, then seismic blanking won't happen anymore. Because whatever hydrate saturation in the sand layer $S_{h,sand}$ is, the average impedance in sand layer, Z_{sand} , will be higher than that in shale (clay) layer, Z_{clay} . So blanking won't happen.

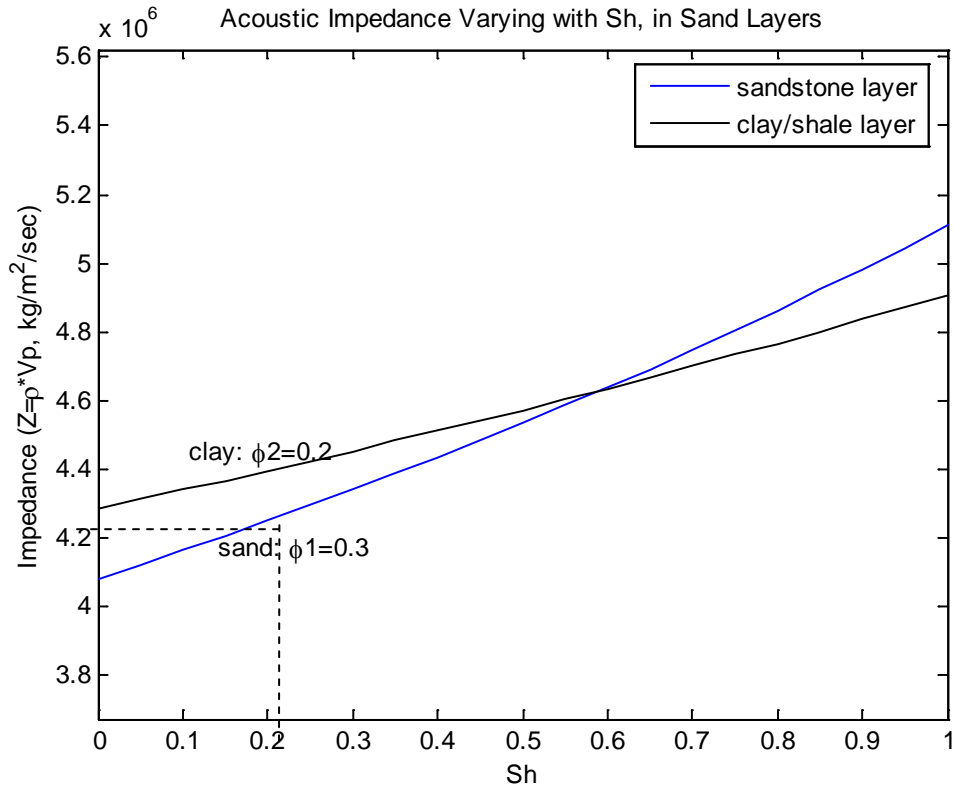


Figure 6.4.2: Impedance increase of sandstone layer due to S_h increase, where blanking is possible. Parameters: $\phi_1=0.3$; $\phi_2=0.2$; intrinsic sand velocity $V_{p_sand}=2300$ m/s; intrinsic shale (or clay) velocity $V_{p_clay}=2000$ m/s. If S_{h_sand} (hydrate saturation in sand layer) increases to around 0.23, the impedance would be comparable to that in clay layer. Assume $S_{h_clay} = 0$, since hydrate saturation in clay layer is often very close to 0.

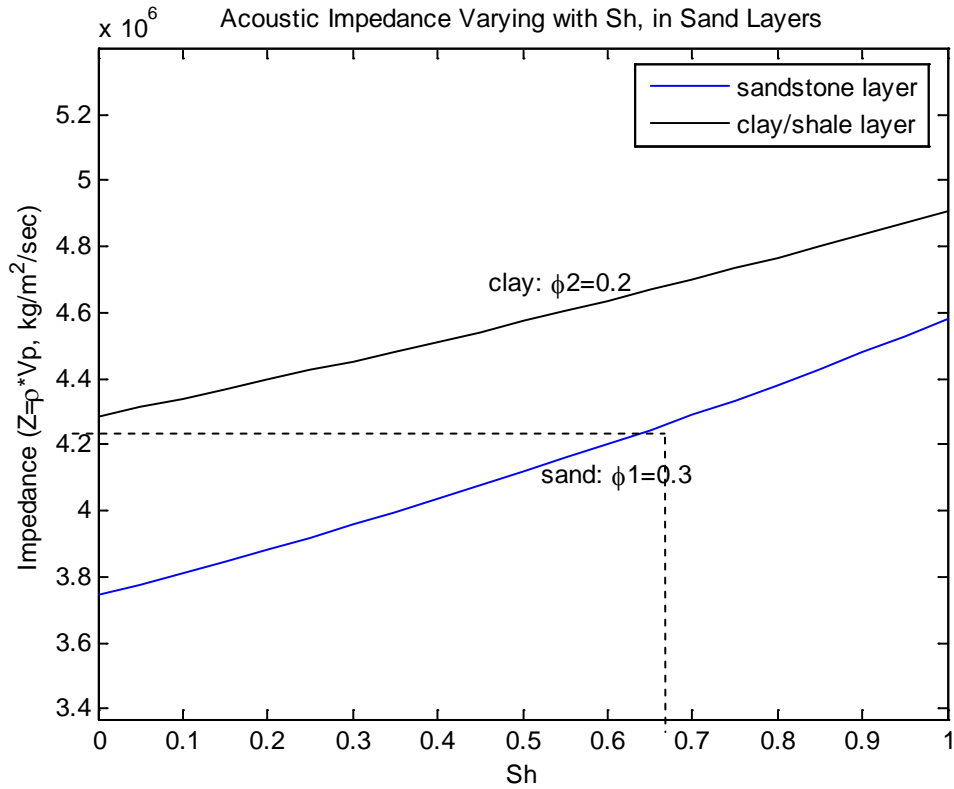


Figure 6.4.3: Impedance increase of sandstone layer due to S_h increase, where blanking is possible Parameters: $\phi_1=0.3$; $\phi_2=0.2$; $V_{p_sand}=2000$ m/s; $V_{p_clay}=2000$ m/s. If S_{h_sand} (hydrate saturation in sand layer) increases to around 0.69, the impedance would be comparable to that in clay layer. Assume $S_{h_clay} = 0$, since hydrate saturation in clay layer is often very close to 0.

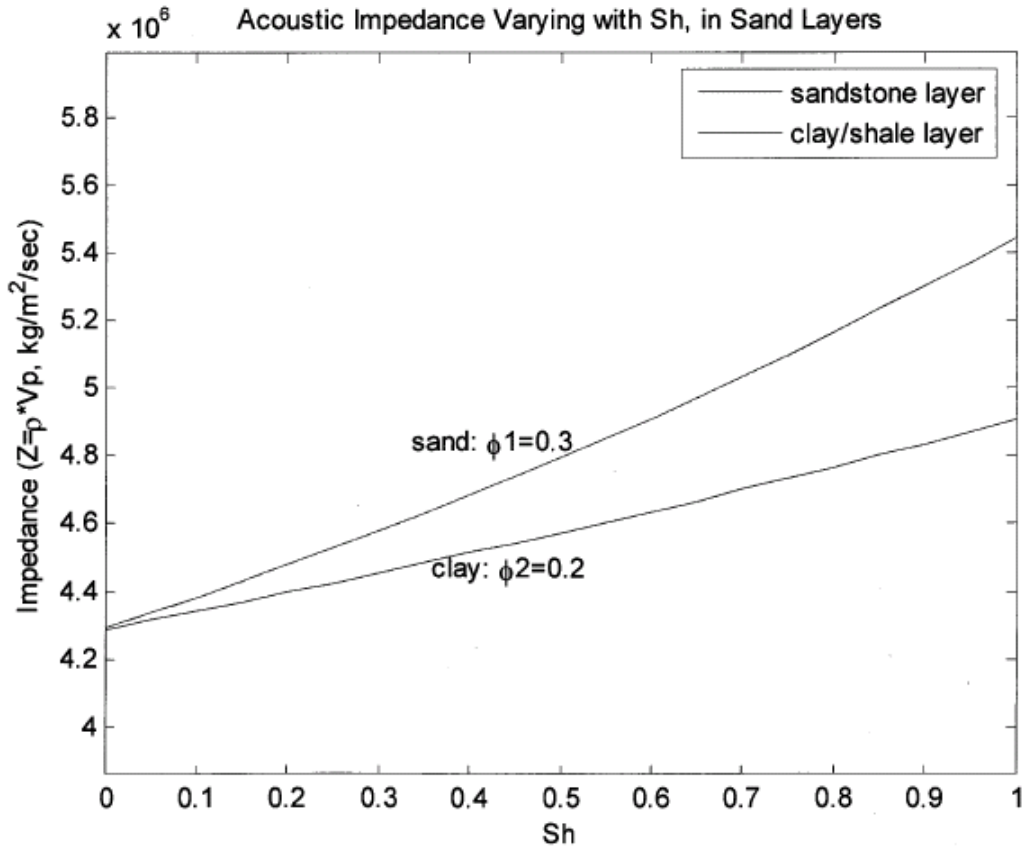


Figure 6.4.4: Impedance increase of sandstone layer due to S_h increase, where blanking is just possible, only at $S_{h,sand}=0$. Parameters: $\phi_1=0.3$; $\phi_2=0.2$; $V_{p,sand}=2500$ m/s; $V_{p,clay}=2000$ m/s. In this figure, only at $S_{h,sand} = 0$, the average impedance in sand layer is equal than that in shale (clay) layer, otherwise, will be always higher.

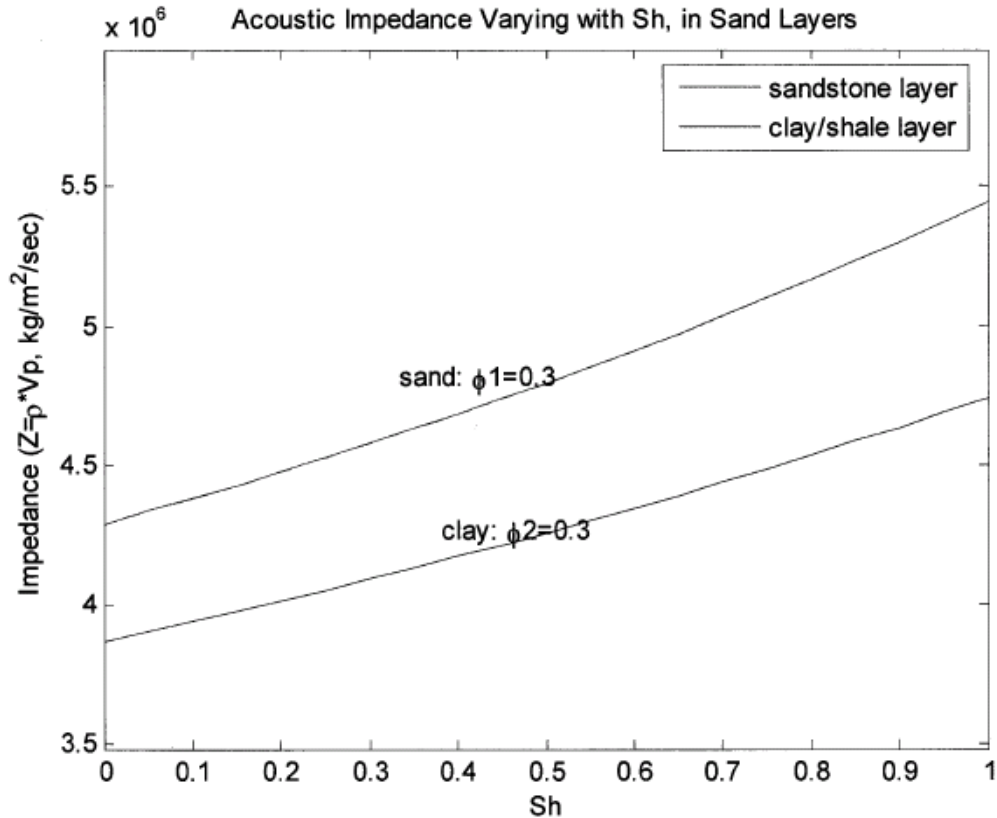


Figure 6.4.5: Impedance increase of sandstone layer due to S_h increase, where blanking is impossible. Parameters: $\phi_1=0.3$; $\phi_2=0.3$; $V_{p_sand}=2500$ m/s; $V_{p_clay}=2000$ m/s. In this figure, whatever S_{h_sand} (hydrate saturation in sand layer) is, the average impedance in sand layer is always higher than that in shale (clay) layer.

Conclusion:

Our study indicates that hydrate accumulation does not guarantee a blanking zone, and the blanking zone does not mean hydrate accumulates, neither. Only in limited parameter space, the blanking zone can be regarded due to hydrate accumulation.

Subtask 6.6: Concentrated hydrate and free gas (Sayantan Chatterjee)

Abstract

We develop numerical models to simulate gas hydrate and free gas accumulation in lithologically heterogeneous marine sediments over geologic time scales. Simulations with a vertical fracture network, which extends through the gas hydrate stability zone and has permeability 100 times greater than the surrounding shale, show that focused fluid flow causes higher hydrate (20-30%)

and free gas saturation (40-50%) within the fracture network compared to the surrounding, lower permeability shale. Systems with dipping, high permeability sand layers also show localized, elevated saturations of hydrate and free gas within the high permeability conduits. Permeability anisotropy, with a ratio of vertical to horizontal permeability (order of 10^{-2}) show even higher hydrate concentrations within the high permeability conduits because anisotropy focuses more methane-charged fluid into the high permeability conduits. These 2-D, heterogeneous models quantify how focused fluid flow through high permeability zones affects regional and local hydrate accumulation and saturation. Simulations are being extended with specified fluid flux and methane input from deeper sources, which allows comparison of local methanogenesis and deeper methane sources on flow pathways and hydrate/free gas accumulation. We show that increased fluid flux from external sources would result in enhanced concentrations of hydrate and free gas. This builds on our previous one-dimensional work that shows hydrate saturation is dependent on Peclet number, the ratio of advective flux to the diffusive flux of methane. In our two-dimensional work, we show it is the local advective flux relative to diffusion (local Peclet number) that influences the hydrate and free gas saturation. We relate average local Peclet numbers and average hydrate flux ($Pe_1 < S_h >$) within high permeability conduits which compare favorably with our previously published 1-D results.

6.6.1 Introduction

Gas hydrate accumulation modeling in homogeneous, one-dimensional (1-D) systems has been developed as part of subtasks 6.1 and 6.2 [Bhatnagar *et al.*, 2007]. However, natural gas hydrate systems are more complex than the homogeneous 1-D models. To understand lateral fluid flow and heterogeneity in lithology, it is imperative that the one-dimensional model is extended to a two-dimensional numerical model. The 1-D simulator of geological timescale accumulation of hydrate and free gas has been extended to 2-D and example simulations of heterogeneous systems are demonstrated.

The proposed two-dimensional model incorporates deposition and compaction of heterogeneous sediment, methane generation, and migration of water with dissolved gas. Heterogeneities in the form of fracture network and/or high permeability sand layers result in regions of focused fluid flux. Higher saturations of hydrate and free gas are observed in the higher permeability regions as a result of the increased fluid flux. Example simulations of heterogeneous systems are demonstrated to understand lateral fluid flow in this report. We formulate the two-dimensional numerical model, derive component mass balances and present them in the following section.

6.6.2 Component Mass Balances

The two-dimensional mass balances for water, sediment and organic carbon and methane are illustrated as follows [Bhatnagar, 2008]:

6.6.2.1 Water mass balance

$$\frac{\partial}{\partial t} [\phi S_w c_w^l \rho_w + \phi S_h c_w^h \rho_h] + \nabla \cdot [\phi S_w c_w^l \rho_w \mathbf{v}_w + \phi S_h c_w^h \rho_h \mathbf{v}_h] = 0 \quad (6.6.1)$$

6.6.2.2 Sediment mass balance

$$\frac{\partial}{\partial t} [(1-\phi)\rho_s] + \nabla \cdot [(1-\phi)\rho_s \mathbf{v}_s] = 0 \quad (6.6.2)$$

6.6.2.3 Organic mass balance

$$\frac{\partial}{\partial t} [(1-\phi)\rho_s \alpha] + \nabla \cdot [(1-\phi)\rho_s \mathbf{v}_s \alpha] = -\rho_s \lambda (1-\phi) \alpha \quad (6.6.3)$$

6.6.2.4 Methane mass balance

$$\begin{aligned} & \frac{\partial}{\partial t} [\phi S_w c_m^l \rho_w + \phi S_h c_m^h \rho_h + \phi S_g c_m^g \rho_g] + \nabla \cdot [\phi S_w c_m^l \rho_w \mathbf{v}_w + \phi S_h c_m^h \rho_h \mathbf{v}_s + \phi S_g c_m^g \rho_g \mathbf{v}_g] \\ & = \nabla \cdot [\phi S_w \rho_w D_m \nabla \cdot c_m^l] + \frac{M_{CH_4}}{M_{org}} \rho_s \lambda (1-\phi) \alpha \end{aligned} \quad (6.6.4)$$

where c_i^j denotes mass fraction of component i in phase j , S_j denotes saturation of phase j , \mathbf{v}_j denotes velocity vector of phase j , ρ_j denotes density of phase j . The kinetic rate constant for methanogenesis reaction is represented by λ , porosity is denoted by ϕ , D_m is the diffusivity of methane and α is the organic carbon content in the sediment formation. Subscripts s correspond to sediment, w to water, m to methane, h to hydrate, and g to free gas components, respectively. Superscripts l correspond to water, h to hydrate and g to free gas phases, respectively.

6.6.3 Constitutive Relationships

The constitutive relationships used in the following formulation are listed as follows:

Water flux

Water flux in a compacting medium is given by Darcy's law [Bear, 1988]

$$S_w \phi (\mathbf{v}_w - \mathbf{v}_s) = -\frac{\mathbf{k} k_{rw}}{\mu_w} (\nabla p_w - \rho_w g \nabla z) \quad (6.6.5)$$

where \mathbf{v}_w and \mathbf{v}_s denote water and sediment velocities, respectively; \mathbf{k} is the absolute sediment permeability tensor; k_{rw} is the relative permeability of water; μ_w is viscosity of water; and p_w is pore water pressure.

Gas flux

Free gas flux is also given by Darcy's law [Bear, 1988]:

$$S_g \phi (\mathbf{v}_g - \mathbf{v}_s) = -\frac{k k_{rg}}{\mu_g} (\nabla p_g - \rho_g g \nabla z) \quad (6.6.6)$$

where \mathbf{v}_g is the gas velocity, k_{rg} is the relative permeability of gas, μ_g is viscosity of gas, and p_g is gas pressure.

Sediment velocity

The Darcy fluid fluxes are expressed as a product of porosity, saturation and net fluid velocity. Net fluid velocities in the Darcy flux is written as a difference of water and gas velocities denoted by \mathbf{v}_w and \mathbf{v}_g respectively with respect to the sediment velocity \mathbf{v}_s in equations 6.6.5 and 6.6.6. The sediment velocity vector \mathbf{v}_s is the velocity with which the sediment moves in the downward direction. The gas hydrate within the formation and immobile free gas below critical saturation moves downward with the sediment with the same velocity.

Absolute sediment permeability

Absolute sediment permeability is defined as a power law function of porosity [Smith, 1971]

$$k = k_o \left(\frac{\phi}{\phi_o} \right)^8 \quad (6.6.7)$$

where k_o and ϕ_o are the initial sediment permeability and porosity at the seafloor $\tilde{z} = 0$. Reduction in absolute sediment permeability due to formation of gas hydrates as a pore-filling structure is modeled by [Kleinberg et al., 2003]:

$$k(\phi, S_h) = k_o(\phi) \left(1 - S_h^2 + \frac{2(1 - S_h)^2}{\ln(S_h)} \right) \quad (6.6.8)$$

where S_h is the saturation of hydrates within the pores.

Relative permeability of water

Relative permeability of water in the presence of free gas is modeled as [Bear, 1988]:

$$k_{rw} = k_{rw}^o (S_w^*)^4 \quad (6.6.9)$$

where S_w^* is normalized water saturation and is defined as:

$$S_w^* = \frac{S_w - S_{wr}}{1 - S_{wr}} \quad (6.6.10)$$

and k_{rw}^o is the end-point relative permeability of water, and S_{wr} is the residual water saturation.

Relative permeability of gas

Relative permeability of gas in the presence of water is given as [Bear, 1988]:

$$k_{rg} = k_{rg}^o (S_g^*)^2 \quad (6.6.11)$$

where S_g^* is normalized gas saturation and is defined as:

$$S_g^* = \frac{S_g - S_{gr}}{1 - S_{wr} - S_{gr}} \quad (6.6.12)$$

and k_{rg}^o is the end-point relative permeability of gas, and S_{gr} is the residual gas saturation.

The water, hydrate and gas saturations sum up to unity. The phase saturations are related as:

$$S_w + S_h + S_g = 1 \quad (6.6.13)$$

Capillary pressure

Capillary pressure P_c is defined as the difference between gas and water pressure:

$$P_c = p_g - p_w \quad (6.6.14)$$

The Leverett J-function $J(S_w)$, is useful for normalizing capillary pressure profiles for different lithologies with different porosities and permeabilities as:

$$J(S_w) = \frac{P_{c,o}(S_w)}{\sigma_{gw} \cos \theta} \sqrt{\frac{k_o}{\phi_o}} \quad (6.6.15)$$

where $P_{c,o}(S_w)$ is the capillary pressure at reference absolute permeability k_o , porosity ϕ_o ; σ_{gw} is the interfacial tension at the gas-water interface, and θ is the angle of contact. Assuming σ_{gw} and θ to be constant, capillary pressure profile for any given porosity ϕ and permeability tensor k can be computed from the above J-function as:

$$P_c(S_w) = J(S_w) \sigma_{gw} \cos \theta \sqrt{\frac{\phi}{k}} = P_{c,o}(S_w) \sqrt{\frac{k_o \phi}{k \phi_o}} \quad (6.6.16)$$

The capillary pressure curve is defined as a function of normalized water saturation S_w^* by the Brooks-Corey model [Bear, 1988]:

$$P_{c,0}(S_w) = P_{ce,0} (S_w^*)^{-1/n} \quad (6.6.17)$$

where $P_{ce,0}$ is the capillary entry pressure at ϕ_o and k_o , and n is the pore-size distribution index.

Effective stress-porosity relationship

Effective stress-porosity relationship is defined by [Rubey and Hubbert, 1959]:

$$\phi = \phi_{\infty} + (\phi_0 - \phi_{\infty}) e^{-\frac{\sigma_v - p_w}{\sigma_{\phi}}} \quad (6.6.18)$$

where ϕ_{∞} is the minimum porosity achieved at the greatest depth, σ_v is vertical effective stress, and σ_{ϕ} is a constant characteristic stress.

Lithostatic stress gradient

Lithostatic stress gradient is defined as a function of densities and porosity as:

$$\frac{\partial \sigma_v}{\partial z} = [(1 - \phi) \rho_s + \phi \rho_w] g \quad (6.6.19)$$

6.6.4 Normalized Variables and Key Dimensionless Groups

The variables and the model parameters are now normalized with the help of a specific scaling scheme discussed below [Bhatnagar et al, 2007]. This normalization technique leads us to defining a few key dimensionless groups.

Porosity parameters

Reduced porosities are defined as follows:

$$\gamma = \frac{1 - \phi_{\infty}}{\phi_{\infty}} \quad \eta = \frac{\phi_0 - \phi_{\infty}}{1 - \phi_{\infty}} \quad \tilde{\phi} = \frac{\phi - \phi_{\infty}}{1 - \phi_{\infty}} \quad (6.6.20)$$

Peclet numbers

The dimensionless group Peclet number Pe_1 is characterized by the ratio of sedimentation-compaction driven fluid flux to methane diffusion.

$$Pe_1 = \frac{U_{f, sed} L_t}{D_m} \quad (6.6.21)$$

Similarly, Pe_2 is characterized by the ratio of external fluid flux from deeper sediment relative to methane diffusion.

$$Pe_2 = \frac{U_{f, ext} L_t}{D_m} \quad (6.6.22)$$

where $U_{f, sed}$ is the fluid flux due to sedimentation-compaction at hydrostatic pore pressure, $U_{f, ext}$ is the fluid flux due to external sources from deeper sediment, L_t is depth to the base of the GHSZ, and \dot{S} is the sedimentation rate at the seafloor. The fluid flux $U_{f, sed}$ due to sedimentation and compaction can be expressed as a combination of seafloor sedimentation rate \dot{S} and the porosities as shown [Bhatnagar et al, 2007].

$$U_{f, sed} = \frac{1 - \phi_0}{1 - \phi_{\infty}} \dot{S} \phi_{\infty} \quad (6.6.23)$$

The sedimentation rate at the seafloor \dot{S} can be defined as:

$$\dot{S} = v_s |_{\bar{z}=0} \quad (6.6.24)$$

Damkohler number

The Damkohler number is defined as the ratio of the methanogenesis reaction to the methane diffusion by:

$$Da = \frac{\lambda L_t^2}{D_m} \quad (6.6.25)$$

where λ is the rate of methanogenesis reaction, and D_m is the diffusivity of methane.

Other dimensionless parameters

A dimensionless group N_{sc} is defined as the ratio of absolute permeability to the sedimentation rate quantifying the effects of sedimentation and compaction as:

$$N_{sc} = \frac{k_0 \rho_w g}{\mu_w \dot{S}} \quad (6.6.26)$$

Large values of N_{sc} implies large sediment permeability and/or low sedimentation rate, further implying pore water pressures close to hydrostatic pressures. Conversely, smaller values of N_{sc} imply low absolute permeability and/or high sedimentation rate, thereby having pore pressures much greater than hydrostatic conditions. Dimensionless groups similar to N_{sc} have been defined in earlier one-dimensional compaction models [Yang and Fowler, 1998; Gutierrez and Wangen, 2005]. Bhatnagar explains the overpressure in hydrate bearing sediments with the help of this dimensionless group N_{sc} [Bhatnagar et al, 2008].

The ratio of characteristic depth of compaction to the depth to the base of GHSZ is defined by the dimensionless group:

$$N'_{t\phi} = \frac{L_\phi}{L_t} = \frac{\sigma_\phi / \rho_w g}{L_t} \quad (6.6.27)$$

Note the new dimensionless group $N'_{t\phi}$ is slightly different from the old definition $N_{t\phi}$ [Bhatnagar et al, 2007].

$$N_{t\phi} = \frac{L_t}{L_\phi} = \frac{L_t}{\sigma_\phi / (1 - \phi_\infty)(\rho_s - \rho_w)g} \quad (6.6.28)$$

Normalized variables

The normalized methane concentrations are defined as:

$$\tilde{c}_m^l = \frac{c_m^l}{c_{m,eqb}^l} \quad \tilde{c}_m^h = \frac{c_m^h}{c_{m,eqb}^l} \quad \tilde{c}_m^g = \frac{c_m^g}{c_{m,eqb}^l} \quad (6.6.29)$$

Lithostatic stress σ_v , water, gas and capillary pressures are normalized by hydrostatic water pressure at the base of the GHSZ:

$$\tilde{\sigma}_v = \frac{\sigma_v}{\rho_w g L_t} \quad \tilde{P}_c = \frac{P_c}{\rho_w g L_t} \quad \tilde{P}_w = \frac{P_w}{\rho_w g L_t} \quad \tilde{P}_g = \frac{P_g}{\rho_w g L_t} \quad (6.6.30)$$

The vertical depth and lateral distance are scaled to the depth to the base of GHSZ:

$$\tilde{z} = \frac{z}{L_t} \quad \tilde{x} = \frac{x}{L_t} \quad (6.6.31)$$

The dimensionless time is defined as:

$$\tilde{t} = \frac{t}{L_t^2 / D_m} \quad (6.6.32)$$

All phase densities are scaled by the density of water as:

$$\tilde{\rho}_h = \frac{\rho_h}{\rho_w} \quad \tilde{\rho}_g = \frac{\rho_g}{\rho_w} \quad \tilde{\rho}_s = \frac{\rho_s}{\rho_w} \quad (6.6.33)$$

Sedimentation and compaction in this model is assumed to be one dimensional with zero lateral strain. This enables the sediment formation to move in vertical direction only, with no movement in the lateral direction. Furthermore, gas hydrate within the formation and immobile free gas below critical saturation moves downward with the sediment. Water and mobile gas, however, can move in both vertical and horizontal directions. Therefore, the sediment velocity vector v_s is replaced in the following equations by the z-direction velocity v_z . The sediment velocity v_z is normalized by the sedimentation rate at the seafloor S .

$$\tilde{v}_z = \frac{v_z}{S} \quad (6.6.34)$$

Finally, organic carbon content and initial TOC are scaled as:

$$\tilde{\alpha} = \frac{\alpha}{\alpha_0} \quad \beta = \frac{\alpha_0}{c_{m,eqb}^l} \quad (6.6.35)$$

where α_0 is the TOC content at the seafloor and $c_{m,eqb}^l$ is the solubility of methane in water at the base of the GHSZ.

6.6.5 Dimensionless Mass Balance Equations and Boundary Conditions

The four mass balance equations and their corresponding initial and boundary conditions are now expressed in a dimensionless form scaling it with the normalized variables defined above. The accumulation term is also expanded so that porosity can be expressed as a function of changing pore pressure and lithostatic stress.

6.6.5.1 Time derivative term expansion

The accumulation terms in the mass balance equations are basically a product of primary variables like saturation (S_i), porosity (ϕ) and mass fraction (c_i^j) of component i in phase j . The time derivative can be expanded as shown:

$$\Delta_t(\phi S_i c_i^j) = \phi^{n+1} S_i^{n+1} c_i^{j,n+1} - \phi^n S_i^n c_i^{j,n} \quad (6.6.36)$$

where Δ_t represents the change in time and superscripts $n+1$ and n represents different time steps. On adding and subtracting a term $\phi^{n+1} S_i^n c_i^{j,n}$, we get:

$$\Delta_t(\phi S_i c_i^j) = \phi^{n+1} S_i^{n+1} c_i^{j,n+1} - \phi^n S_i^n c_i^{j,n} + \phi^{n+1} S_i^n c_i^{j,n} - \phi^{n+1} S_i^n c_i^{j,n} \quad (6.6.37)$$

On rearranging, we get:

$$\Delta_t(\phi S_i c_i^j) = \phi^{n+1} (S_i^{n+1} c_i^{j,n+1} - S_i^n c_i^{j,n}) + S_i^n c_i^{j,n} (\phi^{n+1} - \phi^n) \quad (6.6.38)$$

which can be expressed as:

$$\Delta_t(\phi S_i c_i^j) = \phi^{n+1} \Delta_t(S_i c_i^j) + S_i^n c_i^{j,n} \Delta_t(\phi) \quad (6.6.39)$$

Porosity is a function of effective stress as shown in equation (6.6.18) and is normalized using the scaling scheme shown in equations 6.6.20 through 6.6.35. Dimensionless reduced porosity $\tilde{\phi}$ is related to the dimensionless lithostatic stress $\tilde{\sigma}_v$ and pore pressure \tilde{p}_w .

$$\tilde{\phi} = \eta e^{\left[-\frac{\tilde{\sigma}_v - \tilde{p}_w}{N'_{\phi}} \right]} \quad (6.6.40)$$

Time derivative of porosity as a function of pore pressure can be written as follows:

$$\Delta_t(\phi S_i c_i^j) = \phi^{n+1} \Delta_t(S_i c_i^j) + S_i^n c_i^{j,n} \frac{\partial \phi}{\partial p_w} \Delta_t p_w \quad (6.6.41)$$

From the effective stress-porosity relationship, porosity was differentiated with respect to pore pressure.

$$\Delta_t(\phi S_i c_i^j) = \phi^{n+1} \Delta_t(S_i c_i^j) + S_i^n c_i^{j,n} \left[\frac{\phi - \phi_{\infty}}{\sigma_{\phi}} \right] \left[1 - \frac{\sigma_v^{n+1} - \sigma_v^n}{p_w^{n+1} - p_w^n} \right] \Delta_t p_w \quad (6.6.42)$$

The time derivative expansion for accumulation terms in the following mass balance equations can be expanded using the same technique. These time derivative terms are now put back in the mass balance equations (6.6.1 – 6.6.4) and then normalized with the help of different normalized variables discussed above in equations 6.6.20 through 6.6.35.

6.6.5.2 Water balance

$$\begin{aligned}
& \left(\frac{1+\gamma\tilde{\phi}}{\gamma} \right) \frac{\partial}{\partial \tilde{t}} [S_w \tilde{c}_w^l + S_h \tilde{c}_w^h \tilde{\rho}_h] + \frac{\tilde{\phi}}{N'_{t\phi}} [S_w \tilde{c}_w^l + S_h \tilde{c}_w^h \tilde{\rho}_h] \frac{\partial}{\partial \tilde{t}} (\tilde{p}_w - \tilde{\sigma}_v) \\
& + Pe_1 \left(\frac{1+\gamma}{1-\eta} \right) \frac{\partial}{\partial \tilde{z}} \left[\left(\frac{1+\gamma\tilde{\phi}}{\gamma} \right) (S_w \tilde{c}_w^l + S_h \tilde{c}_w^h \tilde{\rho}_h) \tilde{v}_s - N_{sc} \left(\frac{1+\gamma}{\gamma} \right) \left(\frac{1+\gamma\tilde{\phi}}{1+\gamma\eta} \right)^8 k_{rw} \left(\frac{\partial \tilde{p}_w}{\partial \tilde{z}} - 1 \right) \tilde{c}_w^l \right] \\
& + Pe_1 \left(\frac{1+\gamma}{1-\eta} \right) \frac{\partial}{\partial \tilde{x}} \left[-N_{sc} \left(\frac{1+\gamma}{\gamma} \right) \left(\frac{1+\gamma\tilde{\phi}}{1+\gamma\eta} \right)^8 k_{rw} \left(\frac{\partial \tilde{p}_w}{\partial \tilde{x}} \right) \tilde{c}_w^l \right] = 0 \tag{6.6.43}
\end{aligned}$$

The initial condition (I.C.) is assumed to be hydrostatic. The boundary condition (B.C.) at the seafloor is assumed hydrostatic, and the left and right extremes of the domain are considered as no-flow boundaries. The initial and boundary conditions are expressed as follows:

$$\text{I.C.: } \tilde{p}_w(\tilde{z}, \tilde{x}, 0) = \frac{\rho_w g L_o + \rho_w g z}{\rho_w g L_t} = \frac{L_o + z}{L_t} = \frac{L_o}{L_t} + \tilde{z}, \text{ (Hydrostatic conditions)} \tag{6.6.44}$$

$$\text{B.C.: } \tilde{p}_w(0, \tilde{x}, \tilde{t}) = \frac{L_o}{L_t}, \text{ (Seafloor conditions)} \tag{6.6.45}$$

$$\frac{\partial \tilde{p}_w}{\partial \tilde{x}}(\tilde{z}, 0, \tilde{t}) = \frac{\partial \tilde{p}_w}{\partial \tilde{x}}(\tilde{z}, L_x, \tilde{t}) = 0, \text{ (No-flow conditions)} \tag{6.6.46}$$

The bottommost boundary has been modeled to have a specified fluid flux thereby specifying a constant non-hydrostatic pressure gradient. The specified fluid flux is equal to $U_{f, sed}$ for biogenic sources and equal to a sum $U_{f, sed} + U_{f, ext}$ for thermogenic sources at greater depths. The pressure gradient at the lowermost boundary was earlier defined as a hydrostatic pressure gradient where $\frac{\partial \tilde{p}_w}{\partial \tilde{z}}(L_z, \tilde{x}, \tilde{t}) = 1$ was not consistent with our generalized 2-D model because our pore pressures are no longer hydrostatic pressures when we simulate hydrate and free gas accumulation in heterogeneous sediment.

To resolve this inconsistency, we rewrite our boundary condition at the lowermost boundary as shown below. We specify a flux at the lowermost boundary equal to $U_{f, sed} + U_{f, ext}$ and rewrite our Darcy water flux (equation 6.6.5) for the lowermost boundary as follows:

$$v_w S_w \phi = v_s S_w \phi - \frac{k k_{rw}}{\mu_w} (\nabla p_w - \rho_w g \nabla z) = U_{f, sed} + U_{f, ext} \quad (6.6.47)$$

On normalizing equation 6.6.47, we get:

$$\tilde{v}_w S_w \frac{1+\gamma\tilde{\phi}}{\gamma} = \tilde{v}_s S_w \frac{1+\gamma\tilde{\phi}}{\gamma} - k_{rw} \left(\frac{1+\gamma}{\gamma} \right) \left(\frac{k_o \rho_w g}{\dot{S} \mu_w} \right) \left(\frac{k}{k_o} \right) (\nabla \tilde{p}_w - \nabla \tilde{z}) = \frac{1+\gamma}{\gamma} \frac{[U_{f, sed} + U_{f, ext}]}{\dot{S}} \quad (6.6.48)$$

Substituting, $U_{f, sed} = \frac{1-\phi_o}{1-\phi_\infty} \dot{S} \phi_\infty$ (Eq. 6.6.23), $\frac{k_o \rho_w g}{\dot{S} \mu_w} = N_{sc}$ (Eq. 6.6.26), normalizing the flux sum term on the right, and rearranging, we get:

$$-N_{sc} \left(\frac{1+\gamma}{\gamma} \right) \left(\frac{k}{k_o} \right) k_{rw} (\nabla \tilde{p}_w - \nabla \tilde{z}) = \frac{[Pe_1 + Pe_2]}{Pe_1 \gamma / 1 - \eta} - \left(\frac{1+\gamma\tilde{\phi}}{\gamma} \right) S_w \tilde{v}_s \quad (6.6.49)$$

The above equation (6.6.49) can now be expressed in the finite difference form as:

$$\frac{\partial \tilde{p}_w}{\partial \tilde{z}} (L_z, \tilde{x}, \tilde{t}) = 1 - \frac{\frac{[Pe_1 + Pe_2]}{Pe_1 \gamma / 1 - \eta} - \left(\frac{1+\gamma\tilde{\phi}}{\gamma} \right) S_w \tilde{v}_s}{N_{sc} \left(\frac{1+\gamma}{\gamma} \right) \left(\frac{1+\gamma\tilde{\phi}}{1+\gamma\eta} \right) k_{rw} (L_z)} \quad (\text{Non-hydrostatic pressure gradient}) \quad (6.6.50)$$

(6.6.50)

where L_o is the seafloor depth, L_x is the width of the domain, and L_z is the depth to the bottom of the domain. Also note that the relative permeability of water at the bottom boundary $k_{rw}(L_z) = 1$.

A non-hydrostatic boundary condition at the lowermost boundary (Eq. 6.6.50) is actually derived by specifying a finite fluid flux at the boundary. Infinite N_{sc} represents infinite permeability, which implies hydrostatic conditions. For $N_{sc} = \infty$, equation 6.6.50 reduces the pressure gradient to unity which corresponds to a hydrostatic pressure gradient at the lowermost boundary of our simulation domain.

6.6.5.3 Sediment mass balance

$$-\frac{\tilde{\phi}}{N'_{t\phi}} \frac{\partial}{\partial \tilde{t}} (\tilde{p}_w - \tilde{\sigma}_v) + Pe_1 \left(\frac{1+\gamma}{1-\eta} \right) \frac{\partial}{\partial \tilde{z}} [(1-\tilde{\phi})\tilde{v}_s] = 0 \quad (6.6.51)$$

The initial sediment velocity profile is evaluated assuming hydrostatic pressure, whereas the boundary condition for velocity of sediment at the seafloor is the normalized sedimentation rate and equal to unity.

$$\text{I.C.:} \quad \tilde{v}_s(\tilde{z}, \tilde{x}, 0) = \left(\frac{1-\eta}{1-\tilde{\phi}} \right), \quad (\text{Hydrostatic condition}) \quad (6.6.52)$$

$$\text{B.C.:} \quad \tilde{v}_s(0, \tilde{x}, \tilde{t}) = 1 \quad (\text{Seafloor conditions}) \quad (6.6.53)$$

6.6.5.4 Organic mass balance

$$-\frac{\tilde{\phi}\tilde{\alpha}}{N'_{t\phi}}\frac{\partial}{\partial\tilde{t}}(\tilde{p}_w - \tilde{\sigma}_v) + (1-\tilde{\phi})\left(\frac{\partial\tilde{\alpha}}{\partial\tilde{t}}\right) + Pe_1\left(\frac{1+\gamma}{1-\eta}\right)\frac{\partial}{\partial\tilde{z}}[(1-\tilde{\phi})\tilde{v}_s\tilde{\alpha}] = -Da(1-\tilde{\phi})\tilde{\alpha} \quad (6.6.54)$$

There is no organic carbon present within the sediment, whereas the boundary condition of organic carbon concentration at the seafloor is normalized to unity.

$$\text{I.C.: } \tilde{\alpha}(\tilde{z}, \tilde{x}, 0) = 0 \quad (6.6.55)$$

$$\text{B.C.: } \tilde{\alpha}(0, \tilde{x}, \tilde{t}) = 1 \quad (\text{Seafloor conditions}) \quad (6.6.56)$$

6.6.5.5 Methane mass balance

$$\begin{aligned} & \left(\frac{1+\gamma\tilde{\phi}}{\gamma}\right)\frac{\partial}{\partial\tilde{t}}[S_w\tilde{c}_m^l + S_h\tilde{c}_m^h\tilde{\rho}_h + S_g\tilde{c}_m^g\tilde{\rho}_g] + \frac{\tilde{\phi}}{N'_{t\phi}}[S_w\tilde{c}_m^l + S_h\tilde{c}_m^h\tilde{\rho}_h + S_g\tilde{c}_m^g\tilde{\rho}_g]\left(\frac{\partial\tilde{p}_w}{\partial\tilde{t}} - \frac{\partial\tilde{\sigma}_v}{\partial\tilde{t}}\right) \\ & + Pe_1\left(\frac{1+\gamma}{1-\eta}\right)\frac{\partial}{\partial\tilde{z}}\left[\left(\frac{1+\gamma\tilde{\phi}}{\gamma}\right)(S_w\tilde{c}_m^l + S_h\tilde{c}_m^h\tilde{\rho}_h + S_g\tilde{c}_m^g\tilde{\rho}_g)\tilde{v}_s - N_{sc}k_{rw}\left(\frac{1+\gamma}{\gamma}\right)\left(\frac{1+\gamma\tilde{\phi}}{1+\gamma\eta}\right)^8\left(\frac{\partial\tilde{p}_w}{\partial\tilde{z}} - 1\right)\tilde{c}_m^l\right] \\ & + Pe_1\left(\frac{1+\gamma}{1-\eta}\right)\frac{\partial}{\partial\tilde{z}}\left[-N_{sc}\left(\frac{1+\gamma}{\gamma}\right)\left(\frac{1+\gamma\tilde{\phi}}{1+\gamma\eta}\right)^8k_{rg}\left(\frac{\partial\tilde{p}_g}{\partial\tilde{z}} - \tilde{\rho}_g\right)\left(\frac{\mu_w}{\mu_g}\right)\tilde{\rho}_g\tilde{c}_m^g\right] \\ & + Pe_1\left(\frac{1+\gamma}{1-\eta}\right)\frac{\partial}{\partial\tilde{x}}\left[-N_{sc}\left(\frac{1+\gamma}{\gamma}\right)\left(\frac{1+\gamma\tilde{\phi}}{1+\gamma\eta}\right)^8k_{rw}\left(\frac{\partial\tilde{p}_w}{\partial\tilde{x}}\right)\tilde{c}_m^l - N_{sc}\left(\frac{1+\gamma}{\gamma}\right)\left(\frac{1+\gamma\tilde{\phi}}{1+\gamma\eta}\right)^8k_{rg}\left(\frac{\partial\tilde{p}_g}{\partial\tilde{x}}\right)\left(\frac{\mu_w}{\mu_g}\right)\tilde{\rho}_g\tilde{c}_m^g\right] \\ & = \frac{\partial}{\partial\tilde{z}}\left[\left(\frac{1+\gamma\tilde{\phi}}{\gamma}\right)S_w\frac{\partial\tilde{c}_m^l}{\partial\tilde{z}}\right] + \frac{\partial}{\partial\tilde{x}}\left[\left(\frac{1+\gamma\tilde{\phi}}{\gamma}\right)S_w\frac{\partial\tilde{c}_m^l}{\partial\tilde{x}}\right] + \frac{M_{CH_4}}{M_{org}}\tilde{\rho}_sDa(1-\tilde{\phi})\tilde{\alpha}\beta \quad (6.6.57) \end{aligned}$$

Initially, there is no methane in the system. At the seafloor, methane concentration is equal to zero; methane flux is set to zero at the right and left extremes of the domain; the bottom boundary has a choice of boundary condition, depending on the methane source. The methane concentration gradient (Neumann) is equal to zero for a system with biogenic *in-situ* sources only, whereas the methane concentration (Dirichlet) is set a constant value $c_{m,ext}^l$ for a system with deeper thermogenic sources.

$$\text{I.C.: } \tilde{c}_m(\tilde{z}, \tilde{x}, 0) = 0, \quad (6.6.58)$$

$$\text{B.C.: } \tilde{c}_m(0, \tilde{x}, \tilde{t}) = 0, \quad (\text{Seafloor conditions}) \quad (6.6.59)$$

$$\frac{\partial\tilde{c}_m^l}{\partial\tilde{x}}(\tilde{z}, 0, \tilde{t}) = \frac{\partial\tilde{c}_m^l}{\partial\tilde{x}}(\tilde{z}, L_x, \tilde{t}) = 0, \quad (\text{No-flow conditions}) \quad (6.6.60)$$

$$\frac{\partial\tilde{c}_m^l}{\partial\tilde{z}}(L_z, \tilde{x}, \tilde{t}) = 0 \quad (\text{Biogenic } in-situ \text{ sources only}) \quad (6.6.61)$$

$$\tilde{c}_m^l(L_z, \tilde{x}, \tilde{t}) = \tilde{c}_{m,ext}^l \quad (\text{Thermogenic sources only}) \quad (6.6.62)$$

6.6.6 Numerical algorithm

The four coupled equations are solved numerically using a fully implicit scheme, with the primary variables being p_w, v_s, α and one of the three from the following (c_m, S_h, S_g) depending on local thermodynamic conditions of the grid block at any given time. All the mass balance equations are rewritten in their residual form and Newton-Raphson method is implemented to iterate on them to converge to the solution.

6.6.7 Two-dimensional Model Development with Correct Boundary Conditions

Accumulation of gas hydrate and free gas is modeled in heterogeneous marine sediment over geologic time scales. The two-dimensional numerical model is useful to illustrate how focused fluid flow through vertical fracture network systems and/or high permeability sand layers affects regional and local hydrate accumulation and saturation.

Fracture network systems, dipping sediment beds are common heterogeneities and fluid flow within natural gas hydrate systems are predominated primarily in these local fracture systems and high permeability sand layers, resulting in concentrated hydrate deposits. To incorporate these heterogeneous features and simulate realistic geologic systems, it was pertinent to extend the existing 1-D model [Bhatnagar et al, 2007] to 2-D model. The 2-D model developed in this report has been used to simulate example cases presented in the subsequent sections. However, before simulating heterogeneities, we wanted to compare our 2-D results with our previously published hydrostatic 1-D results [Bhatnagar et al, 2007].

The 2-D numerical model is benchmarked with our hydrostatic 1-D model to make sure it is consistent with our previously published results. We reduced our 2D code to a 1-D (removed x-dimension dependencies), homogeneous transport model and set our model parameters same as hydrostatic 1-D code to be able to duplicate our previous results. We compared methane concentration, hydrate and free gas saturation to find out that there was inconsistency in our 1-D and 2-D model results. We simplified the 2-D model further to one-phase (aqueous) only by removing hydrate and gas phases to be able to identify the reason for this discrepancy. We compared fluid fluxes, phase (fluid and sediment) velocities, porosities, pore-water pressures and observed the fluid fluxes computed in our 2-D model did not match our analytical solution derived earlier [Bhatnagar et al, 2007] as shown in Figure 6.6.1. On attempting to match our hydrostatic 1-D results, we discovered that the current 2-D code has a hydrostatic pressure gradient (Neumann type) boundary condition at the bottom of our simulation domain. According to equation 6.6.50, a hydrostatic pressure gradient $\frac{\partial \tilde{p}_w}{\partial \tilde{z}}(L_z, \tilde{x}, \tilde{t}) = 1$ would imply $N_{sc} = \infty$ which was not what we were simulating. On setting a hydrostatic pressure gradient at the lowermost boundary, we set the Darcy flux equal to zero and according to equation 6.6.5, the fluid and sediment velocities equal at the last grid block (Figure 6.6.2). This need not be a necessary

case if the porosity is still changing and the sediment is still compacting. This imposed an incorrect pressure gradient at the base of our domain which resulted in an incorrect fluid flux. On investigation, we realized that we tried to compare our results with a hydrostatic code, by using a hydrostatic pressure gradient. However, we were not able to match since we were actually simulating non-hydrostatic conditions using finite permeability. We corrected our boundary condition (at the bottom of our domain) as shown in 6.6.50 and was able to duplicate our hydrostatic 1-D for high values of finite N_{sc} (of order 10^4). Our generalized 2-D code now has a specified non-hydrostatic pressure gradient which in turn specifies the fluid flux at the lowermost boundary.

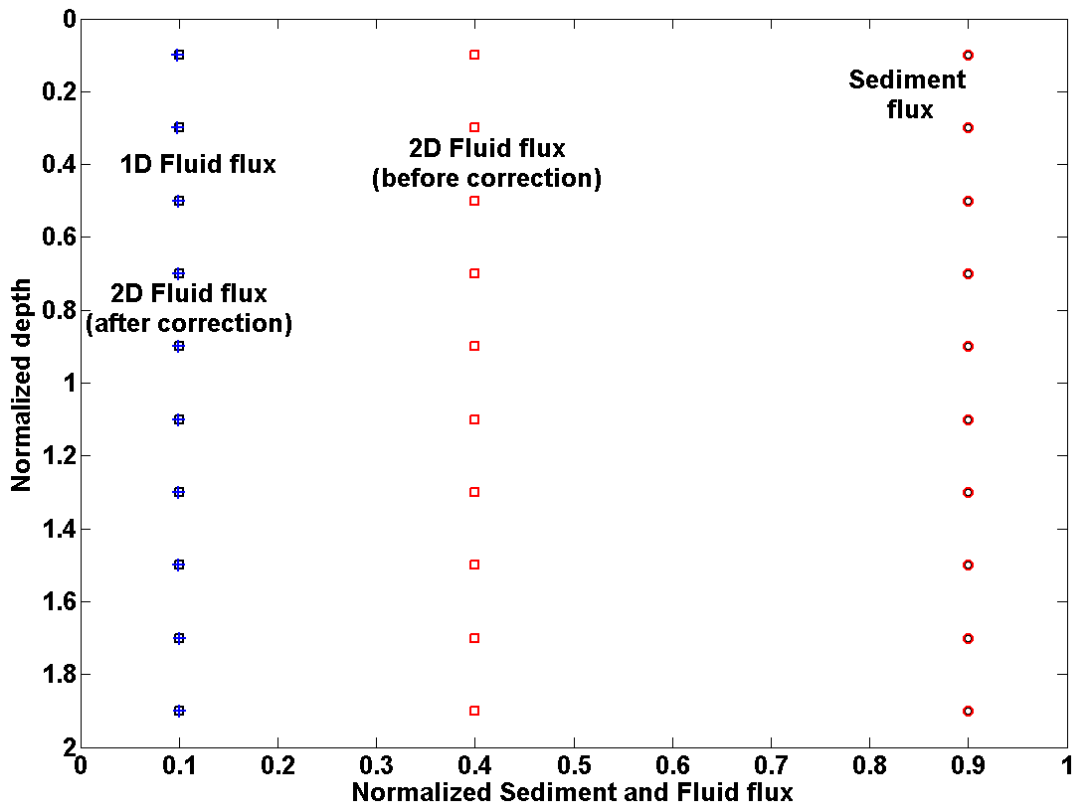


Figure 6.6.1: Normalized sediment and fluid fluxes for 1-D and 2-D simulations. Sediment fluxes (circles) lie right on top of each other. However, the 2-D code fluid fluxes (red squares) were a factor 4 higher than the corresponding 1-D results (black squares). We identified this difference is due to our incorrect hydrostatic pressure gradient at the boundary. We re-derive our boundary condition equations and specify a fluid flux as shown below. This helps us correct our fluid fluxes (blue cross) and benchmark our 2-D code.

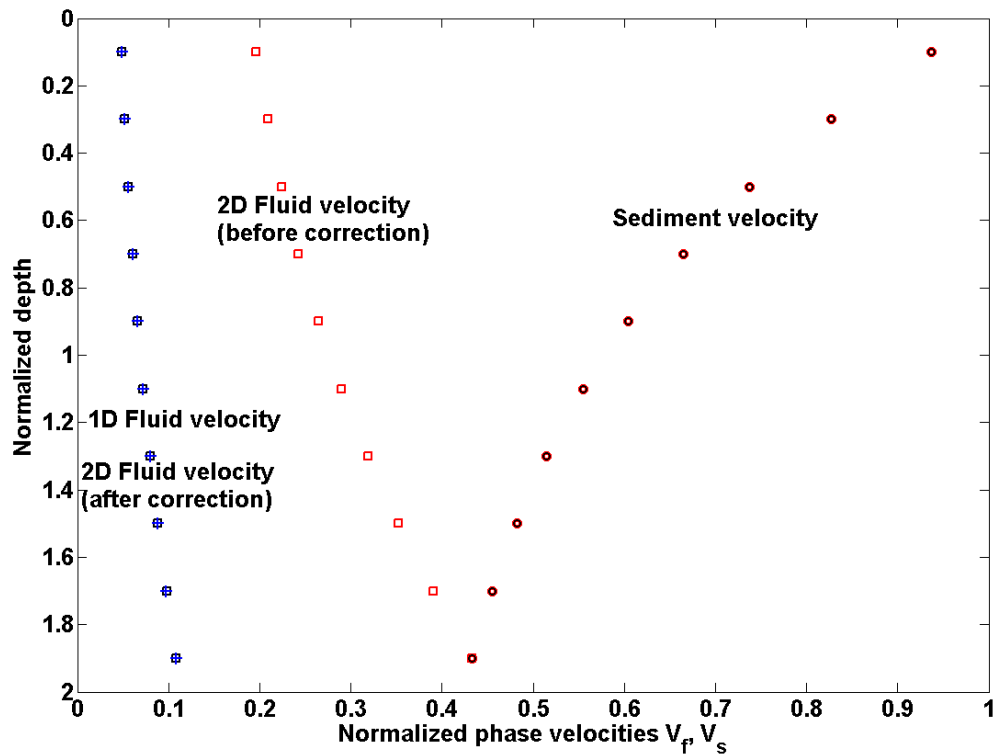


Figure 6.6.2: Normalized fluid and sediment velocities for 1-D and 2-D simulations plotted against normalized depth. The 1-D and 2-D sediment velocities (circles) match exactly, however, the 2-D fluid velocity (red squares) is greater than our previous 1-D fluid velocity (black squares). We recognized this discrepancy is due to the incorrect boundary condition at the lowermost boundary and correct this boundary condition as explained below. The fluid velocities from our corrected 2-D code match our 1-D velocities as plotted (blue cross).

We used our corrected 2-D code to simulate and match our results with the 1-D hydrostatic code as shown in Figures 6.6.3 and 6.6.4. The seafloor parameters used are for the Blake ridge area, same as used in [Bhatnagar *et al*, 2007]. Seafloor depth = 2700m, seafloor temperature = 3°C, and geothermal gradient = 0.04°C/m. We refer to these seafloor parameters as base case values.

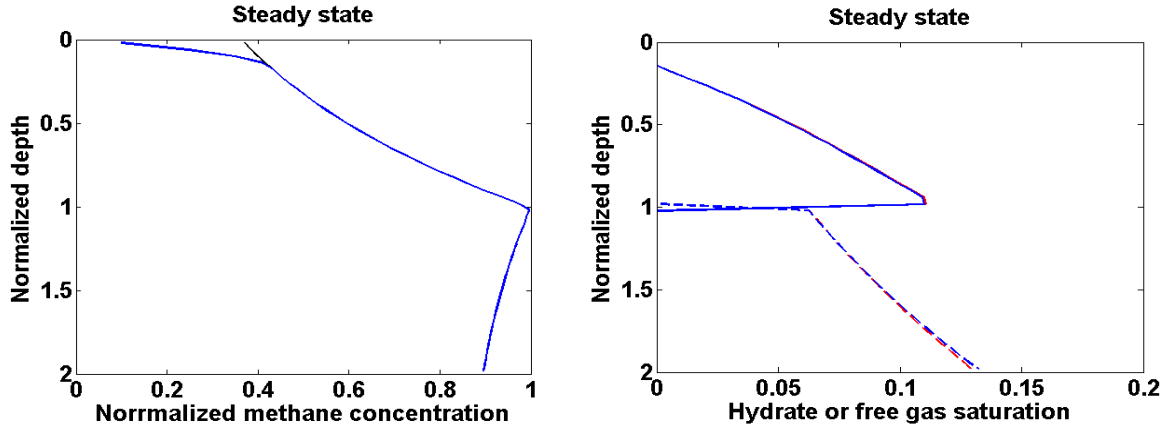


Figure 6.6.3: Steady state simulations showing dissolved methane concentration (left) and the gas hydrate and free gas saturations in the sediment (right). The results shown above are for methane generated from biogenic in-situ source only. The red lines correspond to 2-D simulations and the blue lines to 1-D hydrostatic code. The following parameters were used for this simulation: $Pe_1 = 0.1$, $Pe_2 = 0$, $Da = 10$, $\beta = 6$, $\gamma = 9$, $\eta = 6/9$, $N'_{t\phi} = 1.485$, and $N_{sc} = 10^4$.

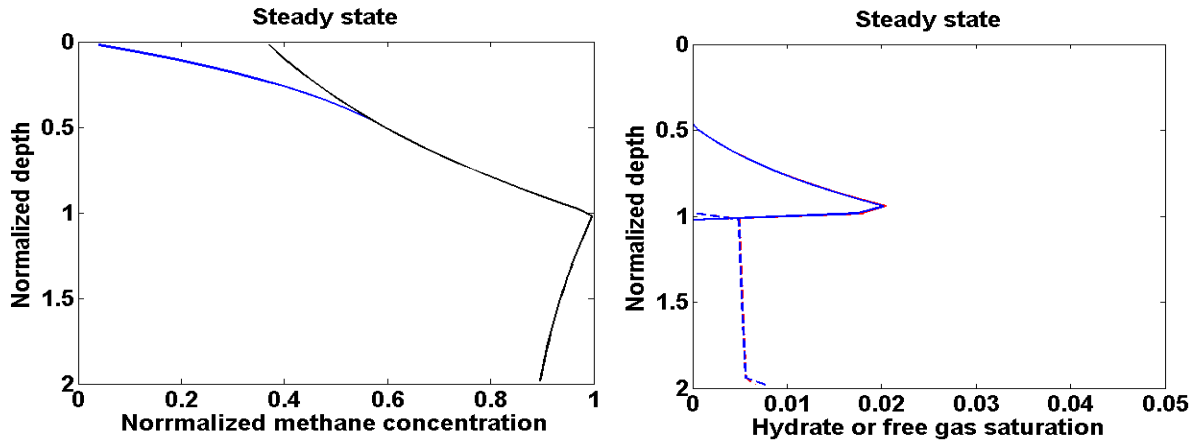


Figure 6.6.4: Steady state simulations showing dissolved methane concentration and the gas hydrate and free gas saturations in the sediment (similar to Fig 6.6.1), except that the methane is transported by an upward external flux from deeper source. The red lines correspond to 2-D simulations and the blue lines to 1-D hydrostatic code. The following parameters were used for this simulation: $Pe_1 = 0.1$, $Pe_2 = -2$, $Da = 0$, $\beta = 0$, $\tilde{c}_{m,ext} = 0.9$, $\gamma = 9$, $\eta = 6/9$, $N'_{t\phi} = 1.485$, and $N_{sc} = 10^4$.

For 1-D systems, average gas hydrate saturation contours are shown as a function of Pe_1 and the net amount of organic carbon converted within the GHSZ [Bhatnagar et al., 2007]. Steady state analytical solution of the organic mass balance is used to compute the normalized organic content at the base of the GHSZ [Bhatnagar et al., 2007] as shown in Figure 6.6.5.

$$\tilde{\alpha} |_{\tilde{z}=1} = \left[\eta + (1-\eta)e^{N_{i\phi}} \right]^{-1} \frac{1}{N_{i\phi}(1+\gamma)Pe_1/Da} \quad (6.6.63)$$

$$\text{Organic carbon converted within GHSZ is } = (1 - \tilde{\alpha} |_{\tilde{z}=1})\beta \quad (6.6.64)$$

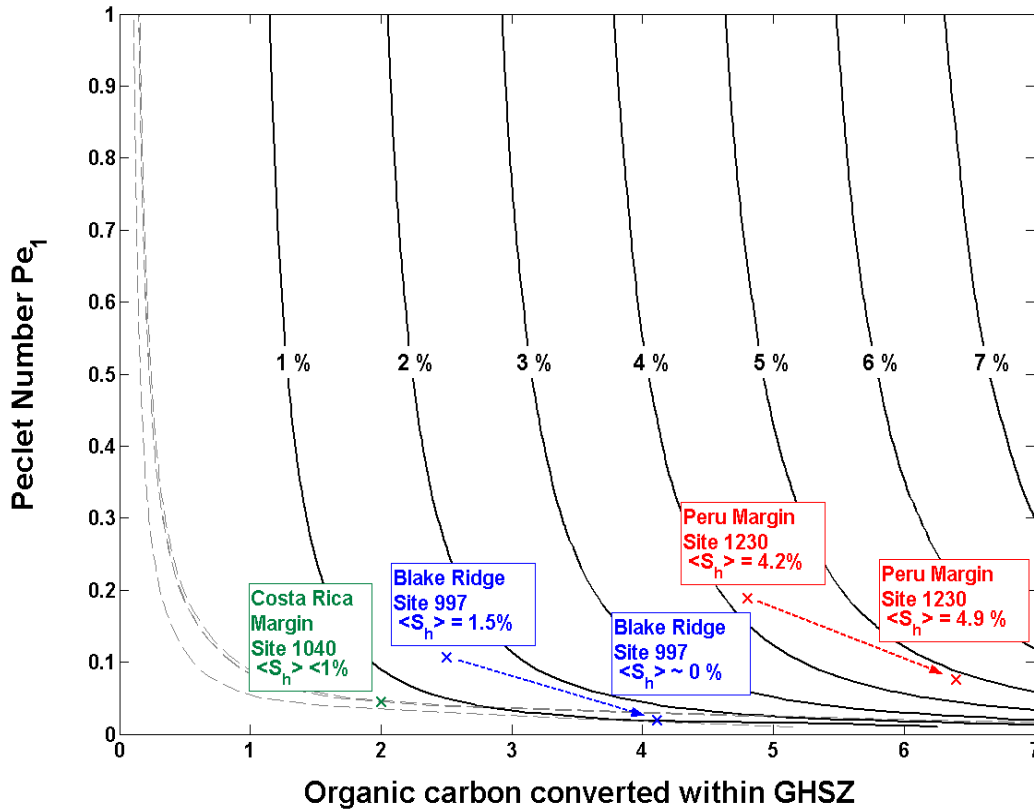


Figure 6.6.5: A single contour map representing average gas hydrate saturation at different gas hydrate settings as a function of organic carbon converted within the GHSZ and Peclet number Pe_1 [from *Bhatnagar et al.*, 2007].

For the transport parameters defined above (in figure 6.6.3), organic carbon converted within GHSZ is 5.93 (from Equation 6.6.64). For corresponding values of $Pe_1 = 0.1$ and the organic carbon converted, average hydrate saturation is ~5% from figure 6.6.5.

The first 2-D simulation run was assuming homogeneous sediment permeability to duplicate the 1-D results previously published [*Bhatnagar et al.*, 2007]. Gas hydrate and free gas saturation contours are shown in Figure 6.6.6.

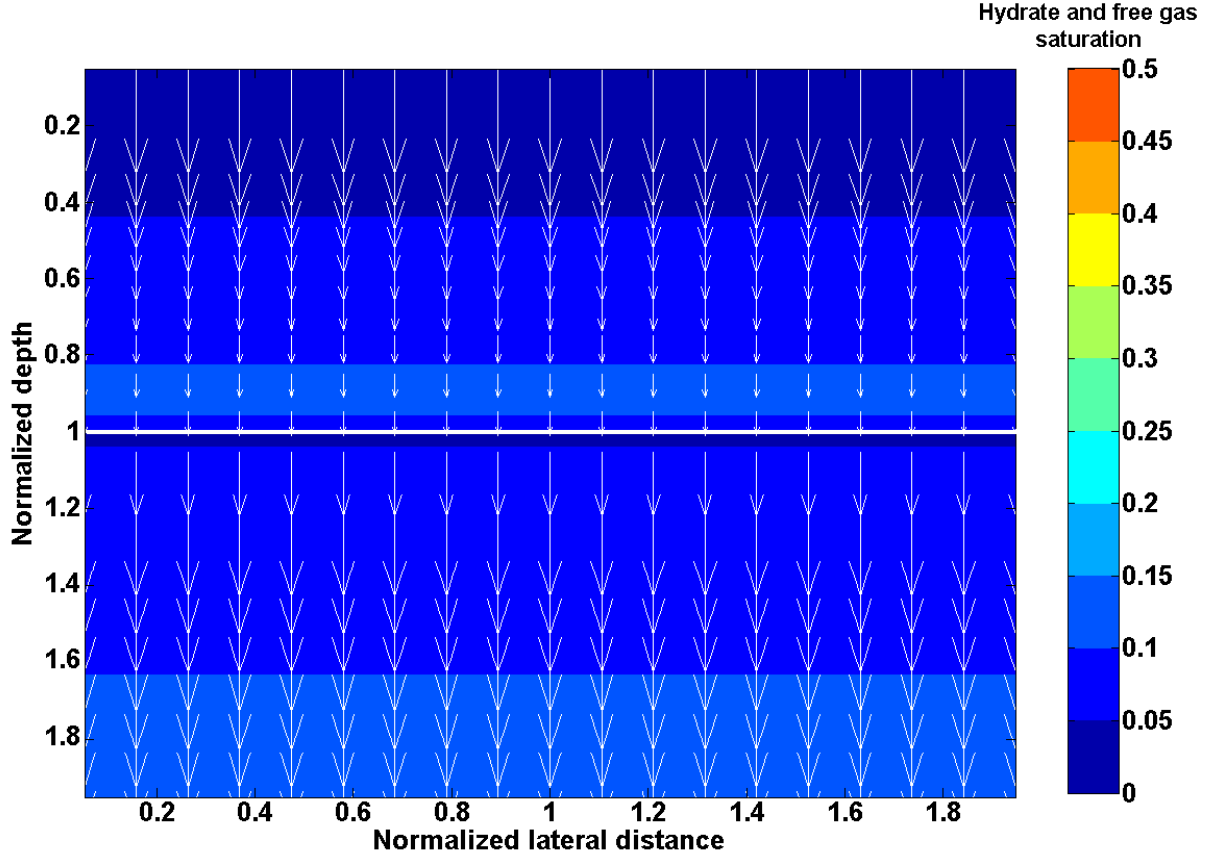


Figure 6.6.6: Steady state gas hydrate and free gas saturation contours at dimensionless time $\tilde{t} = 3.0$ for an isotropic, homogeneous system. Parameters: $Pe_1 = 0.1$, $Pe_2 = 0$, $Da = 10$, $\beta = 6$, $\tilde{c}_{m,ext} = 0$, $\gamma = 9$, $\eta = 6/9$, $N'_{i\phi} = 1.485$, and $N_{sc} = 10^4$.

Average hydrate saturation for isotropic, homogeneous case is 5% (as obtained from contour map in figure 6.6.5) with peak hydrate saturation $\sim 11\%$ matches exactly with the 1-D results for biogenic sources shown in Figure 6.6.3. The physical domain of normalized depth for all the simulations is $\tilde{z} \in [0, 2]$ and normalized lateral distance $\tilde{x} \in [0, 2]$. The arrows represent fluid flux flowing in the downward direction relative to seafloor scaled by maximum flux values. The broad white line at normalized depth $\tilde{z} = 1$ represents the BHSZ. The color bars on the right represent gas hydrate and free gas saturations. Due to the laterally uniform deposition of the sediment, hydrate and free gas saturation also remain constant across the lateral direction. Thus, this system is essentially 1-D in nature. Since the lateral ends of the domain are no-flow boundaries, there is no lateral fluid flow in this system. Consequently, there is no fluid focusing or enhanced concentration of hydrate or free gas within the sediment due to absence of heterogeneities.

From equation 6.6.64, it is evident that the organic carbon converted within the GHSZ is a function of Pe_1 / Da . We plot the normalized organic carbon

content for different values of Pe_1 / Da . The organic content leaving the GHSZ is also observed to be dependent on the ratio Pe_1 / Da as shown in figure 6.6.7.

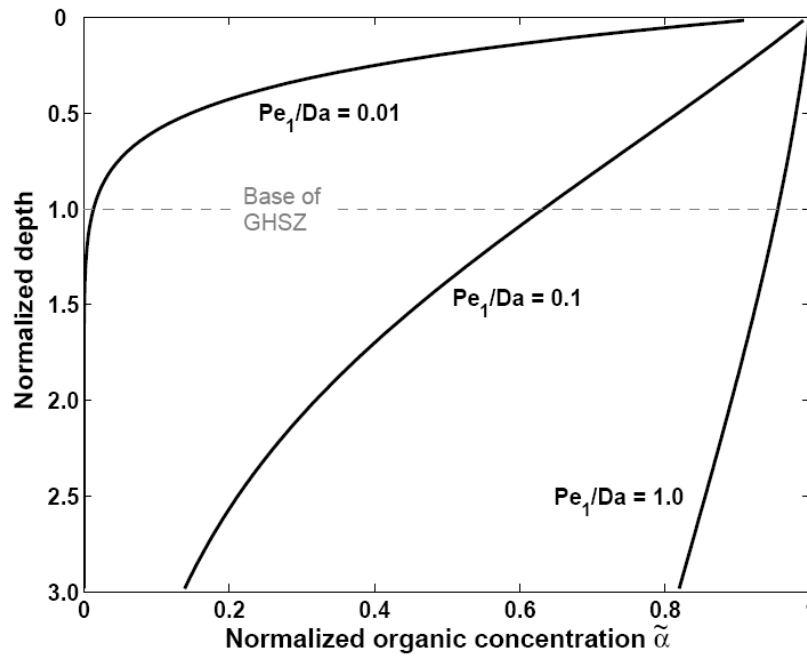


Figure 6.6.7: Normalized organic concentration profiles at steady state as a function of the ratio Pe_1/Da [from *Bhatnagar et al, 2007*].

$$\frac{Pe_1}{Da} = \frac{U_{f, sed}}{\lambda L_t} = \frac{\text{Sedimentation}}{\text{Reaction}} \quad (6.6.65)$$

By the time sediment reaches the base of the GHSZ, there is no organic material left that could be responsible for methane generation below the GHSZ for lower values of Pe_1 / Da (order of 10^{-2}). Larger values of Pe_1 / Da (order of 10^{-1}) result in a considerable amount of organic material leaving the base of the GHSZ. This provides a methane source at depth that can charge water and migrate upwards within the high permeability conduit to accumulate higher amounts of methane. In all our simulation results presented in this report, $Pe_1 / Da = 0.1$, so that more organic content leaves the GHSZ to generate higher amounts of methane below the GHSZ.

Now that we have validated and benchmarked the 2-D model with our 1-D code, we will simulate heterogeneities (e.g. vertical fracture network systems and dipping sand layers) to show how increased fluid flux within these high permeability conduits results in concentrated hydrate deposits. We will also extend the model to include higher pressure at the boundary to simulate higher fluid flux and methane input from deeper sources. We believe increased fluid flux would result in higher concentrations of hydrate and free gas.

6.6.8 Gas Hydrate Systems with Vertical Fracture Networks

Natural gas hydrate systems have several fracture networks, which are dominated by focused fluid flow, acting as high permeability conduits and cause localized high concentration of hydrate and free gas within these networks [Weinberger and Brown, 2006]. This particular lithologic heterogeneity is usually common in geologic settings such as Hydrate Ridge in the Cascadia Margin varying over different length scales [Trehu et al., 2004; Weinberger and Brown, 2006]. In spite of several past research studies having hypothesized the significance of fracture networks in gas hydrate systems, most of the existing state-of-the-art numerical models simulate simple 1-D hydrate accumulation in homogeneous sediment formations. We realized the importance lithologic heterogeneity and Bhatnagar extended his generalized 1-D numerical model [Bhatnagar, 2008] to two-dimensions and assigned different rock properties to different lithologies (such as sand, shales, fracture networks, etc.), thereby enabling the model to study the effect of heterogeneities. Vertical fracture network is simulated in the model by assigning higher permeability in different grid blocks along a single (or multiple) column(s) throughout the simulation domain. Vertical fracture networks are modeled since the time they are introduced at $\tilde{t} = 0$ in the system through steady state and transient gas hydrate and free gas accumulation are followed with sedimentation and deposition of the neighboring formation. The initial permeability distribution for the vertical fracture network is shown schematically in Figure 6.6.8.

Simulations with a vertical fracture network, 100 times more permeable than the surrounding shale formation that extends through the gas hydrate stability zone (GHSZ) up to the seafloor are presented using the 2-D model (i.e. $N_{sc} = 100$ for the shale formation and $N_{sc} = 10^4$ for the vertical fracture system). Once the fracture system is introduced, the transient gas hydrate and free gas accumulation are tracked through time. Simulations with a vertical fracture network, show focused fluid flow causing relatively higher hydrate and free gas saturation within the high permeability fracture system compared to the surrounding, lower permeability shale formation. The effect of the fracture in focusing flow along this high permeability conduit is clearly observed through the enhanced hydrate saturations within the fracture system. The primary dimensionless transport parameters defined in our model and used for all subsequent simulations representing a vertical fracture network system are: $Pe_1 = 0.1$, $Da = 1$, $\beta = 6$, $\gamma = 9$, $\eta = 6/9$, and $N'_{t\phi} = 1$. The critical gas saturation (S_{gr}) is set to 5% and saturation of free gas exceeding this critical value is mobile and free to migrate. Seafloor parameters, relative permeabilities, capillary pressure and physical properties of water, hydrate and free gas are same as the base case as in the Blake Ridge area and discussed above [Bhatnagar et al, 2007].

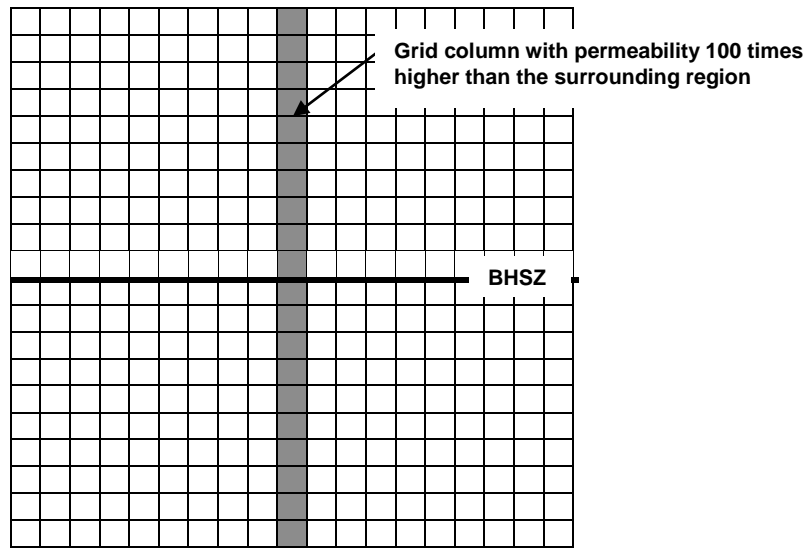


Figure 6.6.8: Permeability map showing initial location of a high permeability vertical fracture network system

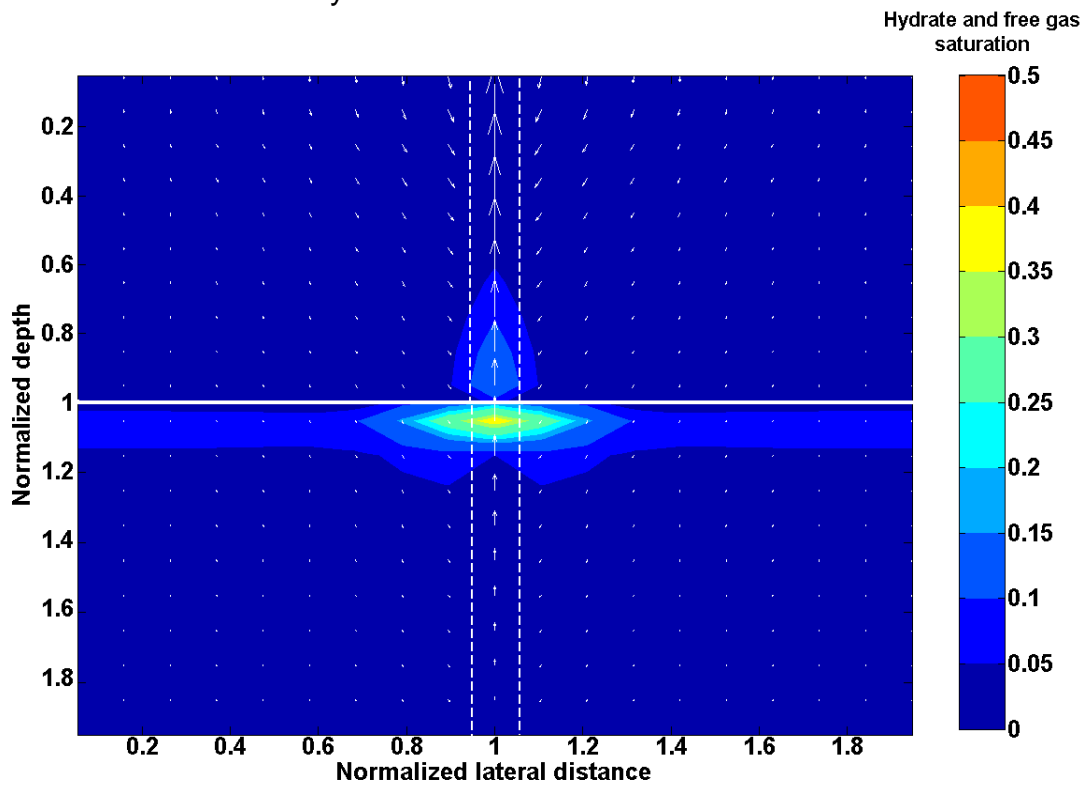


Figure 6.6.9: Steady state gas hydrate and free gas saturation contours at dimensionless time $\tilde{t} = 1.5$ for an isotropic system with a vertical fracture network. Parameters: $Pe_1 = 0.1$, $Pe_2 = 0$, $k_v / k_h = 1$, $Da = 1$, $\beta = 6$, $\tilde{c}_{m,ext} = 0$, $\gamma = 9$, $\eta = 6/9$, $N'_{i\phi} = 1$, and $N_{sc} = 10^2$.

In an isotropic system, with a vertical fracture network, peak gas hydrate saturation within the fracture system is about 15%, while peak hydrate saturation in the surrounding sediment is about 5% at steady state time $\tilde{t}=1.5$ (Figure 6.6.9). Free gas saturation at time $\tilde{t}=1.5$ as shown in figure 6.6.9 depicts peak gas saturation within the fracture network column right below the base of GHSZ. The low permeability hydrate caps the free gas to migrate into the hydrate zone, so this enables the free gas to migrate horizontally. Free gas is observed to migrate from the high permeability fracture system to the neighboring grid blocks (shale formation) laterally below the base of GHSZ. The location of the fracture in the above plot and all the subsequent contour plots, are shown by the set of vertical white dashed lines. The focused fluid flow is visualized by vector field plots shown by white arrows. The fluid flow is in the downward direction because it is plotted relative to the seafloor.

Table 6.6.1 is included which illustrates all the simulated cases along with their corresponding model parameters discussed in the report.

Table 6.6.1: Illustration of various simulated cases along with their model parameters.

Figure	Cases	N_{sc}	k_v/k_h	Da	Pe_1	Pe_2	Time	$N'_{t\phi}$
6.6.7	Homogeneous system	10^4	1	10	0.1	0	3.0	1.485
6.6.9	Vertical fracture system for biogenic sources only	10^2	1	1	0.1	0	1.5	1
6.6.10	Multiple vertical fracture systems	10^2	1	1	0.1	0	1.5	1
6.6.11	Vertical fracture system with external fluid flux	10^2	1	1	0.1	-1	1.5	1
6.6.12	Vertical fracture system with external fluid flux	10^2	1	1	0.1	-2	1.25	1

We extend the lithologic heterogeneity by including multiple vertical fracture systems in our model. We include three such fracture systems and track the hydrate and free gas saturations in these systems. As observed earlier, the hydrates and free gas accumulate in the high permeability conduits as opposed to the shale formation. In figure 6.6.10 we show how the fluid flux gets focused into these 3 high permeability fractures and accumulate hydrate and free gas. On including 3 parallel vertical fractures, peak hydrate saturation within these fracture system is 12-13% (figure 6.6.10) compared to 16% in figure 6.6.9. Figure 6.6.10 also shows free gas saturation contours at $\tilde{t}=1.5$. Buoyant free gas migrates upwards and gets sealed by the low permeability hydrate layer at the base of the GHSZ. Maximum free gas saturation (33%) occurs just below the GHSZ along the high permeability fracture system. At this enhanced saturation, free gas is mobile and migrates laterally, causing neighboring grid blocks just below the GHSZ to also have relatively higher saturations.

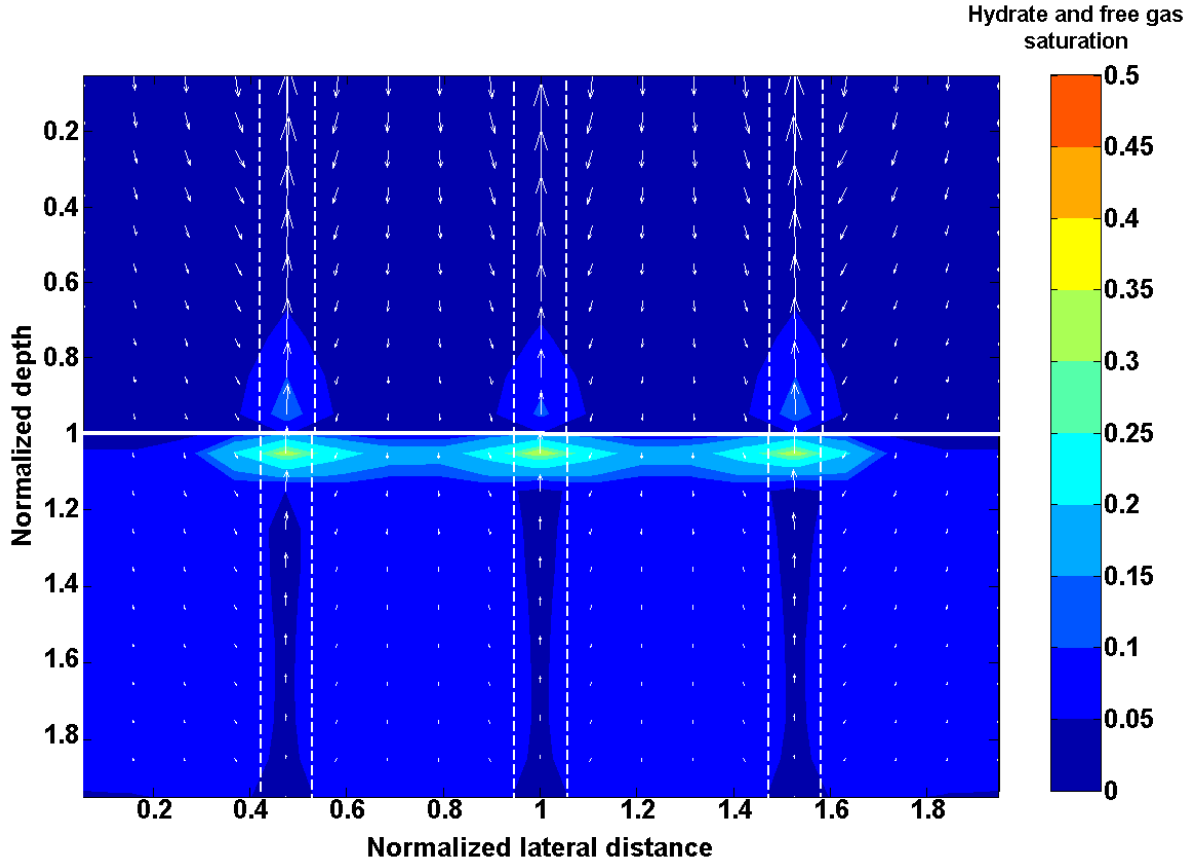


Figure 6.6.10: Steady state gas hydrate and free gas saturation contours at dimensionless time $\tilde{t} = 1.5$ for an isotropic system with multiple vertical fractures. Parameters: $Pe_1 = 0.1$, $Pe_2 = 0$, $k_v/k_h = 1$, $Da = 1$, $\beta = 6$, $\tilde{c}_{m,ext} = 0$, $\gamma = 9$, $\eta = 6/9$,

$$N'_{i\phi} = 1 \text{ and } N_{sc} = 10^2.$$

These above examples were simulated for isotropic systems where horizontal and vertical permeability are equal. For more geologically realistic anisotropic systems, ratio of vertical to horizontal permeability is less than unity. In such systems, greater horizontal permeability would focus more fluid from neighboring regions to the high permeability conduits by lateral migration.

Anisotropic cases with lower ratio of k_v/k_h (order 10^{-2}) are expected to show relatively higher hydrate saturations within the fracture network system because anisotropy focuses more of the fluid into the high permeability conduit. The flow is more prominent with lower realistic values of k_v/k_h . Results with varying ratio of vertical permeability to horizontal permeability (k_v/k_h) in the surrounding shale formation were performed previously (with a hydrostatic boundary condition at the bottom of our domain) and have to be redone with the correct non-hydrostatic boundary condition. However, these anisotropic case simulations are still ongoing and have not been presented in this report.

Our model also has the capability to simulate cases with a specified fluid flux from external sources in deeper sediment. This represents a geologic model with a thermogenic methane source in deeper sediment. We expect higher

hydrate and free gas due to increased fluid flux and methane input into the system from deeper sources. Our simulations allow compare of local methanogenesis and deeper methane sources on flow pathways and hydrate/free gas accumulation. We show that increased fluid flux from external sources result in increased concentrations of hydrate and free gas. In Figure 6.6.11, we simulate a simple case of external fluid flux which shows higher hydrate and free gas saturation in the vertical fracture network as compared to the biogenic *in-situ* methane source case shown in Figure 6.6.9.

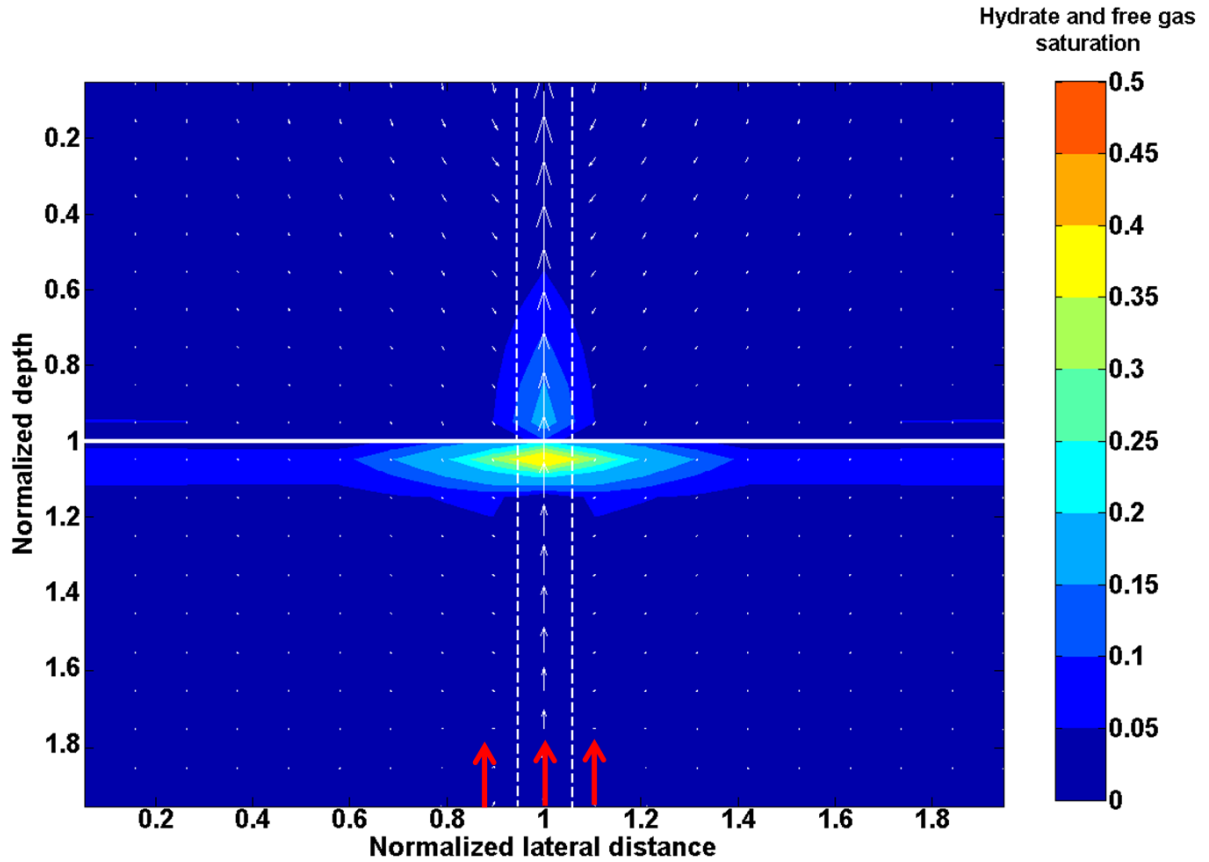


Figure 6.6.11: Steady state gas hydrate and free gas saturation contours at dimensionless time $\tilde{t} = 1.5$ for an isotropic system with a vertical fracture network and a specified external fluid flux specified at the lower boundary and a deeper source of methane. Parameters: $Pe_1 = 0.1$, $Pe_2 = -1$, $k_v / k_h = 1$, $Da = 1$, $\beta = 6$, $\tilde{c}_{m,ext} = 1$, $\gamma = 9$, $\eta = 6/9$, $N'_{t\phi} = 1$, and $N_{sc} = 10^2$.

Note, we specify external fluid flux $Pe_2 = -1$, in selected grid columns, in the fracture network and the neighboring grid columns on either side of the fracture network. The red arrows represent external fluid flux in selected grid columns. We would expect more hydrate and free gas saturation if we specify higher flux or same flux but throughout the lateral dimension. As we increase the fluid flux in this heterogeneous system, we charge more dissolved methane-charged water into these high permeability conduits which result in concentrated deposits of hydrates and free gas within these conduits.

Peak hydrate saturation within the fracture network is around 20% and peak gas saturation within the high permeability region is 44%. Free gas has started to migrate laterally and has high saturation (34%) in the neighboring shale formation adjacent to the fracture network. We now increase the external fluid flux from $Pe_2 = -1$ to $Pe_2 = -2$ and note the hydrate and free gas saturation as shown in Figure 6.6.12.

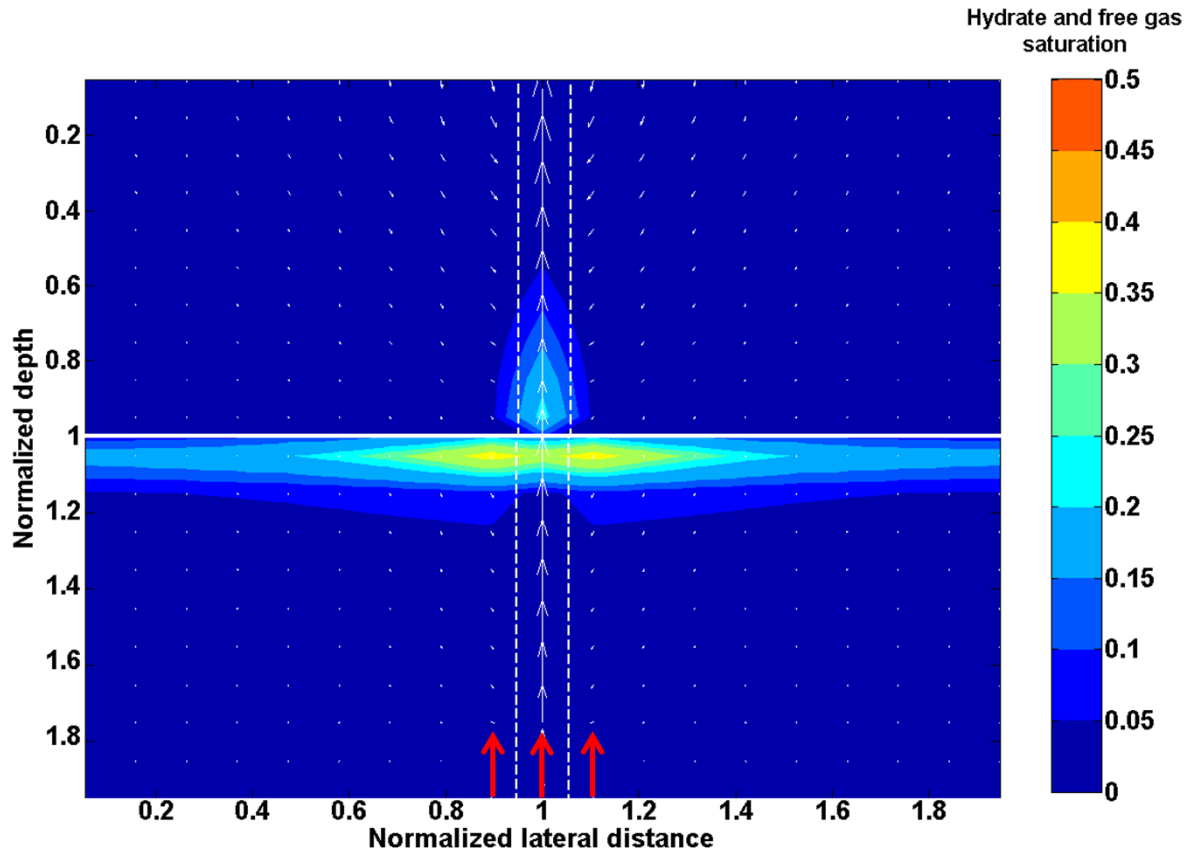


Figure 6.6.12: Steady state gas hydrate and free gas saturation contours at dimensionless time $\tilde{t}=1.25$ for an isotropic system with a vertical fracture network and a specified external fluid flux specified at the lower boundary and a deeper source of methane. Parameters: $Pe_1 = 0.1$, $Pe_2 = -2$, $k_v/k_h = 1$, $Da = 1$, $\beta = 6$, $\tilde{c}_{m,ext} = 1$, $\gamma = 9$, $\eta = 6/9$, $N'_{i\phi} = 1$, and $N_{sc} = 10^2$.

In Figure 6.6.12, peak hydrate saturation increases to 25% within the fracture network and due to increased fluid flux into the system and free gas

saturation is higher as compared to 6.6.11. Peak free gas saturation is 35-40% below the low permeability hydrate layer and migrates to greater distance in the lateral direction. This increased saturation of hydrate and free gas is due to increased fluid flux in the system.

This section of the report summarizes our findings that the presence of vertical fracture systems with higher permeability significantly affects gas, hydrate and free gas distribution by focusing fluid flow along these fracture systems due to biogenic and/or thermogenic sources of methane. Higher hydrate and free gas saturations are observed in the higher permeability fracture systems as a result of the increased fluid flux.

6.8.9 Gas Hydrate Systems with Dipping Sand Layers

In addition to vertical fracture systems, our model also incorporates stratigraphy of varying permeabilities, to simulate dipping sand layers between low permeability shale layers. To model a dipping sand layer, our simulator includes a pre-existing sand layer at a given angle within the sediment formation between two low permeability shale layers which is allowed to deposit and get buried through time. High permeability sand layers extend up to the end of the simulation domain. The downward movement of this sand layer and the corresponding transient hydrate/free gas evolution are then recorded through time. Similar to the fracture network case, high permeability is assigned to different grid blocks at a particular angle as shown below in figure 6.6.13. The initial permeability schematic illustrated in Figure 6.6.13 shows the initial location of this high permeability sand layer.

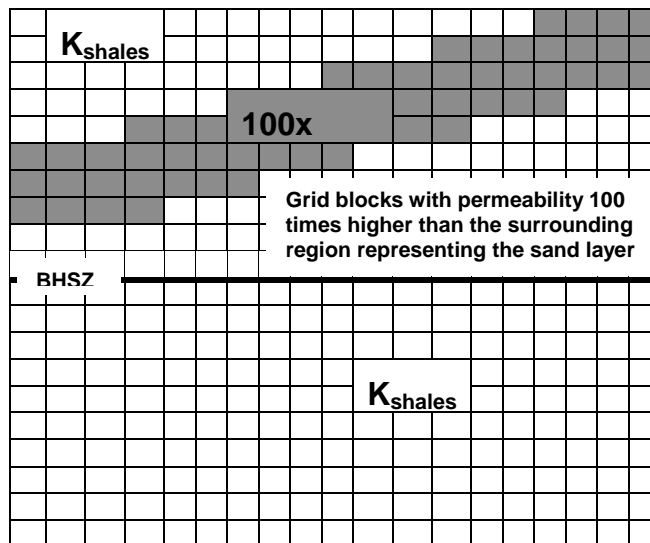


Figure 6.6.13: The initial permeability schematic representing initial high permeability sand layers with permeability 100 times greater than the surrounding shale formation

As shown in Figure 6.6.13, the sand layer is assigned an absolute permeability 100 times greater than the surrounding shale formation and sediment is allowed to bury and compact with time. Due to this burial, absolute permeability of any grid block can be computed by interpolation and therefore, interface between zones of different permeabilities are recorded over time. The interface position is used to compute the horizontal and vertical permeabilities when the sediment layers of varying permeabilities are buried with time. The physical domain of normalized depth for all the simulations is $\tilde{z} \in [0, 2]$ and normalized lateral distance $\tilde{x} \in [0, 10]$. The vertical exaggeration (VE) for all subsequent plots is 5:1. The dimensionless parameter $N_{sc} = 20$ for the low permeability shale formation; whereas $N_{sc} = 2000$ for the sand layer since sand permeability is 100 times that of shale.

The transport and seafloor parameters are similar to the simulations with vertical fracture network. Systems with dipping sand layers should show similar localized, enhanced concentrations of hydrate and free gas within the high permeability conduits. We are currently simulating the dipping sand layer examples and do not present them in this report. We expect to see focused fluid flow in high permeability sand layer and understand how enhanced fluid flux determines high hydrate and free gas saturations in the high permeability sand layers. We also anticipate that our simulation results would elucidate that lithology plays a significant role in accumulating gas hydrate and free gas in heterogeneous sediment in most natural systems.

6.6.10 Conclusions and Future Work

A dimensionless, two-dimensional (2-D) model was developed in this report to simulate gas hydrate and free gas accumulation in marine sediment over geologic time scales. Development of a 2-D model allows incorporation of lithologic heterogeneity and lateral fluid flow in the system. Simulation results shown above can be summarized with the following conclusions.

As the gas saturation exceeds critical gas saturation of ~5%, free gas migrates up into the GHSZ due to buoyancy. Migrated free gas precipitates as low permeability gas hydrate at the base of the GHSZ. Hydrate formation at the base of the GHSZ causes an increase in the capillary entry pressure for the gas column below the base of GHSZ and creates a hindrance for more gas to enter the GHSZ from below. This results in accumulation of free gas beneath the GHSZ into a connected gas column. The length of this connected gas column has been shown to be a function of the dimensionless group N_{sc} (absolute permeability) [Bhatnagar et al, 2008]. Lower values of N_{sc} (lower permeability) result in higher overpressure and development of a longer gas column before gas pressure at the base of the GHSZ exceeds the lithostatic stress. Fractures tend to open up and vent the free gas below the hydrate to towards the seafloor.

This process is not modeled in any of our simulations, and our simulations are terminated as soon as gas effective stress reaches vertical lithostatic stress.

Focused fluid flow through a vertical fracture network and/or high permeability sand layers affecting regional and local hydrate accumulation and saturation can be elucidated with the help of this 2-D model. Currently, relatively simple systems with fracture systems and/or dipping sand layers are simulated, whereas realistic geologic settings are characterized by much more heterogeneous stratigraphy in terms of vertical fracture networks, multiple sand layers embedded within shale layers and fracture connectivity of sand layers with vertical fracture systems. These preliminary results, however, serve as a starting point and demonstrate that the numerical model can be used to simulate systems with considerable heterogeneity to realize the natural gas hydrate systems more precisely.

Permeability anisotropy, with a ratio of vertical to horizontal permeability (order of 10^{-2}) show enhanced hydrate concentrations within the high permeability conduits because anisotropy focuses more methane-charged fluid into these conduits. We are also exploring how fracture connectivity of sand layers affects flow paths and hydrate saturation. Our 2-D model results quantify how focused fluid flow through high permeability zones affects regional and local hydrate accumulation and saturation. Simulations with specified fluid flux and methane input from deeper sources, allows comparison of local methanogenesis and deeper methane sources on flow pathways and hydrate/free gas accumulation. We show that increased fluid flux from external sources result in increased concentrations of hydrate and free gas.

In our previous one-dimensional work, we found that the accumulated hydrate saturation was dependent on Peclet number, Pe , the ratio of advective flux to the diffusive flux of methane. In our current two-dimensional work, we show that it is the local advective flux relative to diffusion (local Peclet number) that determines the magnitude of hydrate and free gas saturation. We relate average local Peclet numbers and average hydrate flux ($Pe_1 < S_h >$) within high permeability conduits which compare favorably with our previously published 1-D results. We intend to adapt our generalized model to specific field examples such as Walker Ridge in the Gulf of Mexico where enhanced hydrate saturation is noted in dipping sand layers.

References

- Bhatnagar G., PhD. Thesis (2008), Accumulation of gas hydrates in marine sediments, Rice University, p 192-236
- Bhatnagar, G., Chapman, W.G., Dickens, G.R., Dugan, B. and Hirasaki, G.J. (2008), Effect of Overpressure on Gas Hydrate Distribution, *Proceedings of the 6th International Conference on Gas Hydrates (ICGH 2008)*, Vancouver, British Columbia, Canada, July 6-10, 2008

- Bhatnagar, G., Chapman, W.G., Dickens, G.R., Dugan, B. and Hirasaki, G.J. (2007), Generalization of gas hydrate distribution and saturation in marine sediments by scaling of thermodynamic and transport processes, *Am. J. Sci.*, 307: p 861-900
- Trehu, A. M., Long, P. E., Torres, M. E., Bohrmann, G., Rack, F. R., Collett, T. S., Goldberg, D. S., Milkov, A. V., Riedel, M., Schultheiss, P., Bangs, N. L., Barr, S. R., Borowski, W. S., Claypool, G. E., Delwiche, M. E., Dickens, G. R., Gracia, E., Guerin, G., Holland, M., Johnson, J. E., Lee, Y. J., Liu, C. S., Su, X., Teichert, B., Tomaru, H., Vanneste, M., Watanabe, M., and Weinberger, J. L. (2004), Three-dimensional distribution of gas hydrate beneath southern Hydrate Ridge: Constraints from ODP Leg 204. *Earth Planet. Sci. Lett.*, 222:845-862
- Weinberger, J. L. and Brown, K. M. (2006), Fracture networks and hydrate distribution at Hydrate Ridge, Oregon. *Earth Planet. Sci. Lett.*, 245(1):123-136

Conference abstracts:

AGU 2010 Fall meeting [*Oral presentation on Dec 16, 2010*], San Francisco, CA

Focused Fluid Flow and Gas Hydrate Distribution in Heterogeneous Marine Sediments

Sayantana Chatterjee, Guangsheng Gu, Gaurav Bhatnagar, Walter G. Chapman, Gerald R. Dickens, Brandon Dugan, George J. Hirasaki

We simulate gas hydrate and free gas accumulation in heterogeneous marine sediments over geologic time scales. Simulations with a vertical fracture network, which extends through the gas hydrate stability zone and has permeability 100 times greater than the surrounding shale, show that focused fluid flow causes higher hydrate and free gas saturation within the fracture network compared to the surrounding, lower permeability shale. Systems with dipping, highly permeability sand layers show similar localized, elevated concentrations of hydrate and free gas within the high permeability conduit. Anisotropic cases with a lower ratio of vertical to horizontal permeability (order of 10^{-2}) show even higher hydrate saturations within the high permeability conduits because anisotropy focuses more methane-charged fluid into the high permeability conduit. We are also exploring fracture connectivity of sand layers with vertical fracture networks. These 2D, heterogeneous models quantify how focused fluid flow through vertical fracture networks or high permeability sand layers affects regional and local hydrate accumulation and saturation. Simulations are being extended with specified fluid flux and methane input from deeper sources, thus allowing comparison of local methanogenesis and deeper methane sources on flow pathways and hydrate/free gas accumulation. We expect that increased fluid flux from external sources would result in enhanced concentrations of hydrate and free gas. This builds on our previous one-dimensional work that shows hydrate saturation is dependent on Peclet number, the ratio of advective flux to the diffusive flux of methane. In our two-dimensional work, we show it is the local advective flux relative to diffusion (local Peclet number) that influences the hydrate and free gas saturation.

7th International Conference on Gas Hydrates July 17-21, Edinburgh, Scotland [Submitted]

Effects of Heterogeneous Lithology and Focused Fluid Flow on Gas Hydrate Distribution in Marine Sediments

Sayantana Chatterjee, Guangsheng Gu, Gaurav Bhatnagar, Walter G. Chapman, Gerald R. Dickens, Brandon Dugan, George J. Hirasaki

We develop numerical models to simulate gas hydrate and free gas accumulation in lithologically heterogeneous marine sediments over geologic time scales. Simulations with a vertical fracture network, which extends through

the gas hydrate stability zone and has permeability 100 times greater than the surrounding shale, show that focused fluid flow causes higher hydrate (20-30%) and free gas saturation (40-50%) within the fracture network compared to the surrounding, lower permeability shale. Systems with dipping, high permeability sand layers also show localized, elevated saturations of hydrate and free gas within the high permeability conduits. Permeability anisotropy, with a ratio of vertical to horizontal permeability (order of 10^{-2}) show even higher hydrate concentrations within the high permeability conduits because anisotropy focuses more methane-charged fluid into the high permeability conduits. We are also exploring how fracture connectivity of sand layers affects flow paths and hydrate saturation. These 2-D, heterogeneous models quantify how focused fluid flow through high permeability zones affects regional and local hydrate accumulation and saturation. Simulations are being extended with specified fluid flux and methane input from deeper sources, which allows comparison of local methanogenesis and deeper methane sources on flow pathways and hydrate/free gas accumulation. We show that increased fluid flux from external sources would result in enhanced concentrations of hydrate and free gas. This builds on our previous one-dimensional work that shows hydrate saturation is dependent on Peclet number, the ratio of advective flux to the diffusive flux of methane. In our two-dimensional work, we show it is the local advective flux relative to diffusion (local Peclet number) that influences the hydrate and free gas saturation. We relate average local Peclet numbers and average hydrate flux ($Pe_1 < S_h >$) within high permeability conduits which compare favorably with our previously published 1-D results. We intend to adapt our generalized model to specific field examples such as Walker Ridge in the Gulf of Mexico where enhanced hydrate saturation is noted in dipping sand layers.

Subtask 6.8b Carbon cycling across SMT above marine gas hydrate systems (Sayantan Chatterjee)

Manuscripts drafts in preparation

- S. Chatterjee, G. Bhatnagar, W.G. Chapman, B. Dugan, G.R. Dickens, G.T. Snyder, G.J. Hirasaki, "*Pore water chemistry profiles above marine gas hydrates systems: A numerical modeling perspective.*" [To be submitted in Journal of Geophysical research]
- G. Bhatnagar, S. Chatterjee, W.G. Chapman, B. Dugan, G.R. Dickens, G.J. Hirasaki, "*Analytical theory relating the depth of the sulfate-methane transition to gas hydrate saturation.*" [Submitted in *Geochemistry, Geophysics, Geosystems*, under review]

Conference presentations

- S. Chatterjee, G. Bhatnagar, W. G. Chapman, B. Dugan, G. R. Dickens, G. J. Hirasaki, "*Sulfate-Methane Transition depth as a proxy for methane flux above gas hydrate systems*", (poster) Gordon Research Conference – Natural gas hydrate systems, Waterville, ME, June 2010

Task 7: Analysis of Production Strategy

J. Phirani & K. K. Mohanty, University of Texas at Austin

Introduction

In previous studies, we have shown that depressurization is ineffective in unconfined reservoirs; horizontal wells are more effective than vertical wells. In this study, we consider reservoirs with a limited aquifer. We assume that the un-confinement of the aquifer is not at the bottom but on one side of the aquifer. For the limited aquifer case we study only horizontal wells, and that makes the reservoir translationally symmetric. So, for this case we study the reservoir in 2 dimensions but the total amount of hydrates and hydrate to water ratio are same as in our previous case of unconfined reservoir. The initial conditions and rock properties are the same as in the previous case. The injection well conditions are also same with injection pressure of 50MPa, and injection temperature of 50°C. Production well pressure is 4MPa. Circle shows the producer and X shows the injector in the figures.

Reservoir description

We consider a hydrate block similar to the block AC 818 in the Gulf of Mexico. The block is a 1200m long and 500m wide reservoir, as shown in Figure 7.1. It has a 18m thick hydrate layer which is underlain by an infinite aquifer. In the hydrate zone, hydrate saturation is 0.75 and water saturation is 0.25. Initial pressure at the bottom of the reservoir is 31.4MPa and initial temperature is 294.88K which vary in the reservoir according to hydrostatic pressure drop and geothermal gradient, respectively. To model the infinite aquifer a 12m thick aquifer zone is considered for simulation in which the bottom most 3m layer was assumed to have a permeability $1/10^{\text{th}}$ of the hydrate layer absolute permeability. The water saturation is 1.0 for the aquifer layer. For over-burden, no mass flow is allowed while heat can transfer with a specified heat transfer coefficient. At the under-burden, we have an infinite aquifer, so, heat transfer is allowed and the pressure is specified at the bottom boundary. The water can come into the reservoir or go out according to the pressure difference between the bottom most grid layer and the boundary pressure. For lateral boundaries no heat or mass flow is considered, due to symmetry.

Results

Horizontal reservoir

Figure 7.1 shows the well configurations we study for the horizontal reservoirs. The bold line at the bottom shows the un-confinement where constant pressure condition is maintained. The pressure maintained is equal to the initial pressure of the reservoir. Water can flow in or flow out of the reservoir depending on the difference between reservoir pressure and boundary pressure at un-confinement. The under-burden in this case is an impermeable shale layer so no mass flow boundary condition is applied. The horizontal wells are in perpendicular direction to the face shown in the figure.

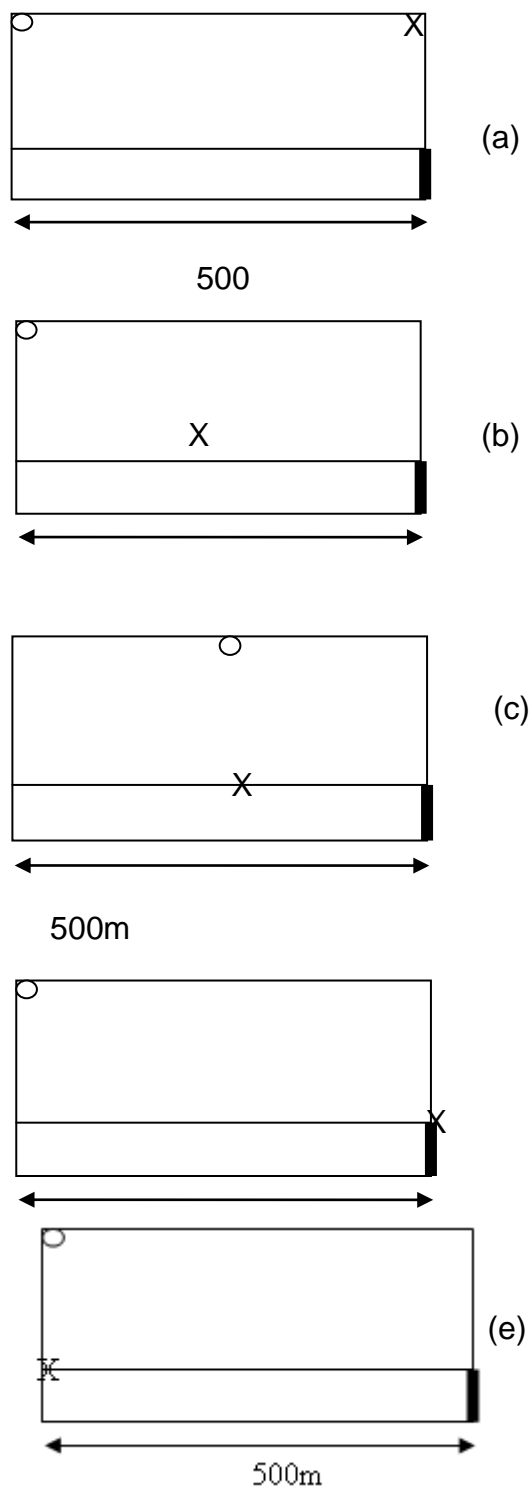


Figure 7.1: Schematic of 2-d reservoir showing (a) 'injector_up_producer_up', (b) 'injector_downmid_producer_up', (c) 'inline_mid', (d) 'opposite' and (e) 'inline_side'

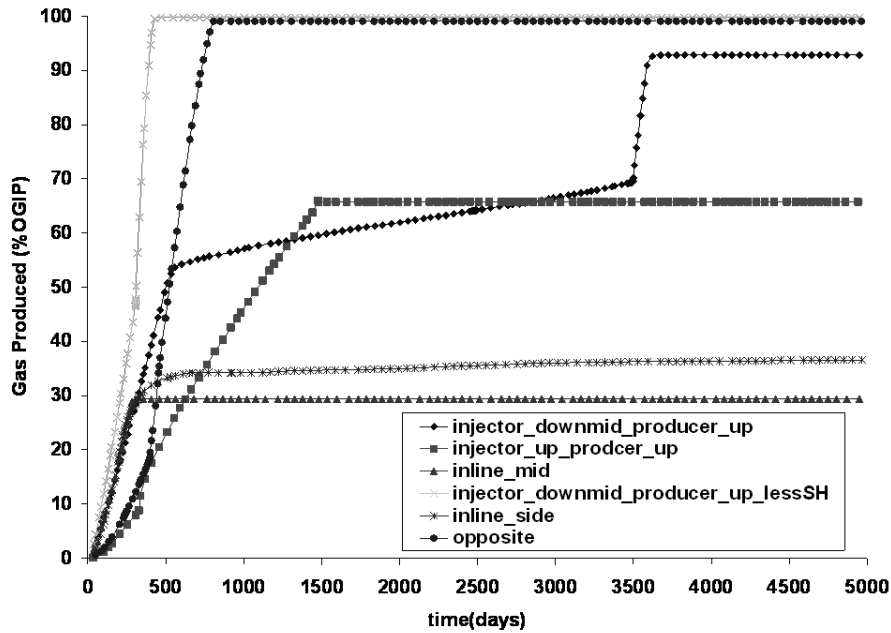


Figure 7.2: Production curves for different well configurations

First we compare the two cases with different hydrate saturations for which the well configuration is shown in Fig 7.1(b). If hydrate saturation is low then the permeability of hydrate bearing layer is high and the mobility of the fluids in the hydrate bearing layer is high. Hence the flow of the injected water is high in the low hydrate saturation (0.6) case and gas is produced at a high rate. Figure 7.2 shows the cumulative production of gas. Also less heat is needed to dissociate less amount of hydrate in the same pore volume. Figure 7.3a shows the in-situ profiles for high hydrate saturation case 'injector_downmid_producer_up'. Initially all the hydrates on the right of the injection well are dissociated (Fig 7.3a). Due to presence of the un-confinement on the right side in the aquifer we are able to maintain a pressure drop on the right side so water is flowing and is dissociating hydrate.

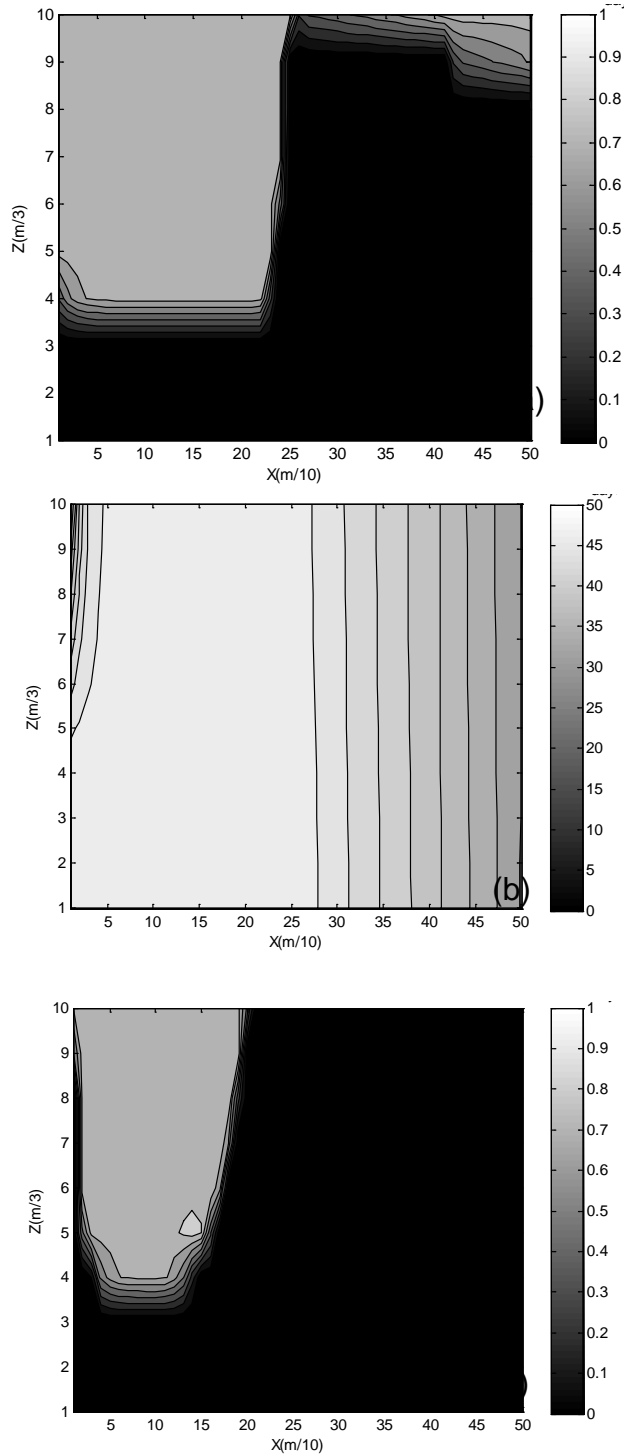


Figure 7.3: (a) Hydrate saturation profile after 450 days (b) pressure profile after 450 days (c) hydrate saturation profile after 3300 days for 'injector_downmid_producer_up'

On the left side the pressure in the aquifer zone is almost same and hence no water flow towards left (Fig 7.3b). The production well is not able to depressurize a whole lot due to high hydrate saturation leading to low permeability. When all the hydrates on the right side of the injection well have dissociated the gas production rate decreases as the hydrate dissociation rate on the left side is very slow. After about 3500 days some hydrate dissociates on the left most boundary and a water channel forms to the production well (Fig 7.3c). This increases the flow of warm water through the channel in the left direction and hence an increase production rate is seen after 3500 days. But still

we are not able to recover 100% of OGIP in 5000 days because some of the hydrates on the top left side are bypassed by formation of the channel.

Due to formation of water channel in the cases 'inline_mid' and 'inline_side' warm water flows from injector to producer bypassing most of the hydrates. Figure 7.4(a) and (b) shows the hydrate saturation profile after 5000 days for the case 'inline' and 'inline_side' respectively, showing water channel formation. In these cases injector and producer are very close to each other; so we produce only 30-35% of original gas in place.

In the case when injector and producer both are on the top of the hydrate bearing layer 'injector_up_producer_up' the injection is very difficult in the hydrate layer. But the aquifer unconfined is limited to only one side so we are able to depressurize the reservoir slowly. Figure 7.4(c) shows the in-situ profile of hydrate saturation after 5000 days for this case. A lot of hydrates are left undissociated.

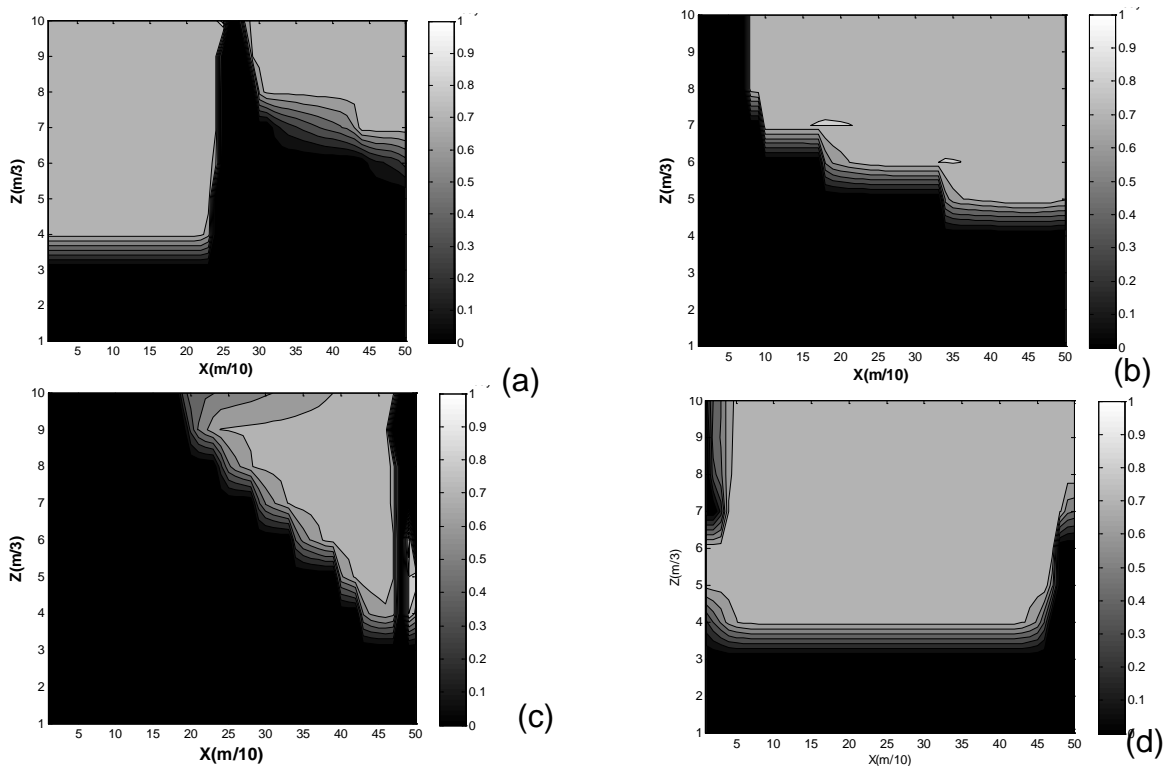


Figure 7.4: Hydrate saturation profile (a) after 5000 days for the case 'inline', (b) after 5000 days for the case 'inline_side', (c) after 5000 days for the case 'injector_up_producer_up' and (d) after 200 days for 'opposite'

In the case named 'opposite', we are able to take advantage of both warm water flooding as well as depressurization as the wells are far apart. In this case no channel is formed due to large distance between the wells. Figure 7.4(d) shows the hydrate saturation profile after 200 days showing the depressurization and warm water flooding effect.

For the horizontal reservoirs where the aquifer is limited, the depressurization helps and the above study shows that it is better to keep the injector and producer at a horizontal distance so that water channel does not form to bypass the hydrate bearing sediments. Injector near the aquifer helps to transfer heat due to high permeability of aquifer zone. High hydrate saturation also affects the mobility of the fluids; depressurization is more effective when hydrate saturation is low in the sediments.

Dipping reservoirs

To study the effect of dip (20°) and to find the optimum well configuration for dipping unconfined reservoirs with limited aquifer, we study configurations shown in Figure 7.5.

In the dipping reservoirs, the over-burden and under-burden are impermeable shale layers. The ratio of initial hydrate to water is same as in the horizontal reservoir. The reservoir is unconfined along the depth and a pressure boundary condition is applied to model the limited aquifer. Gas rises due to gravity so the production well has to be at the top of the reservoir. From the simulation of horizontal reservoirs, we found that warm water injection helps when the injection well is near to the limited aquifer, as mobility of water is higher in the aquifer. Using this information we try two limiting cases of injection well on the water hydrate contact boundary. In the case 'production_top_injection_top' the injection well is near overburden while in the case 'production_top_injection_bottom' the injection well is near underburden. For dipping the reservoir, we try depressurization in the 'no_injection' case.

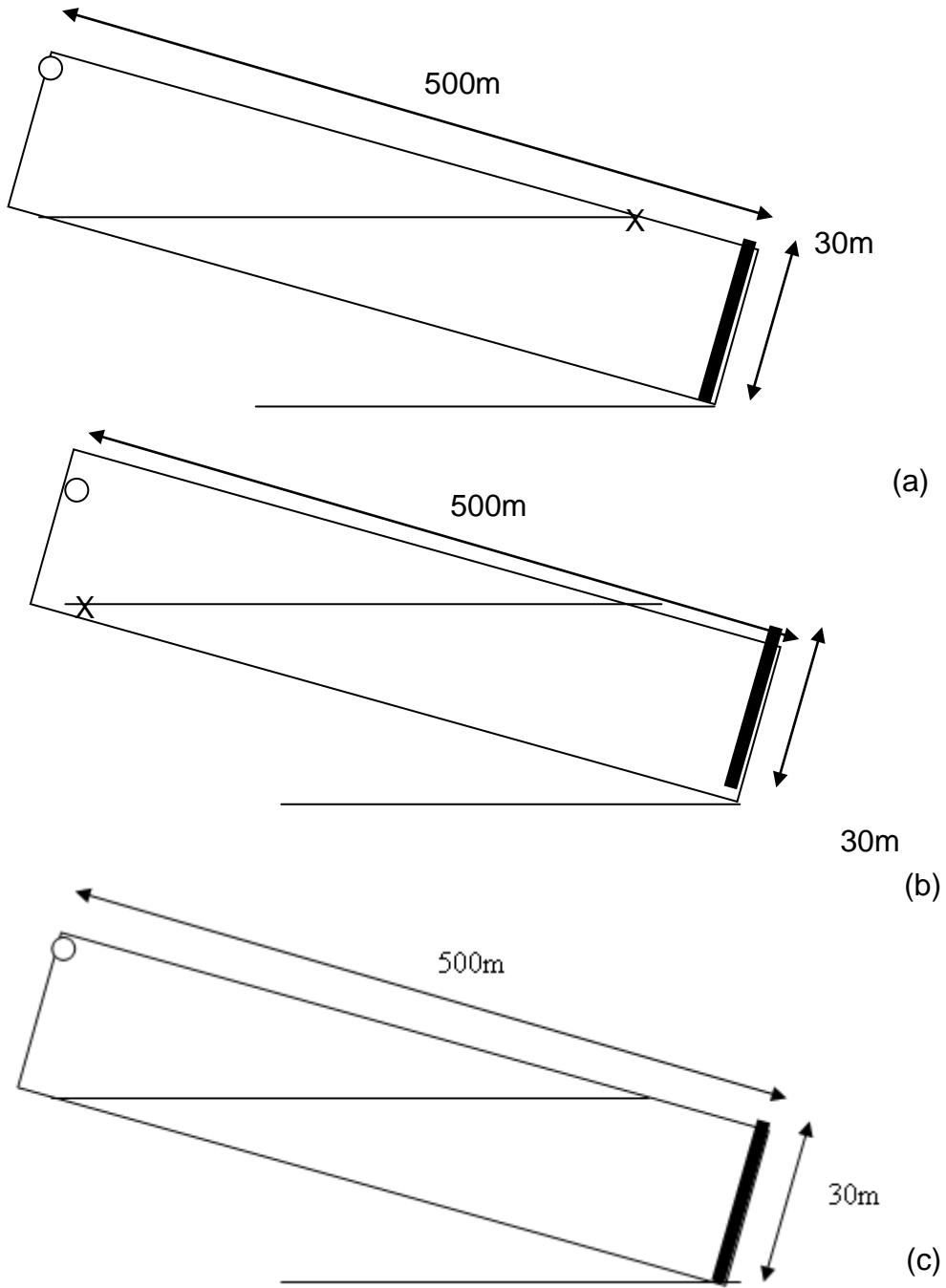


Figure 7.5: Dipping hydrate reservoir (a) 'production_top_injection_top', (b) 'production_top_injection_bottom' and (c) 'no_injection'

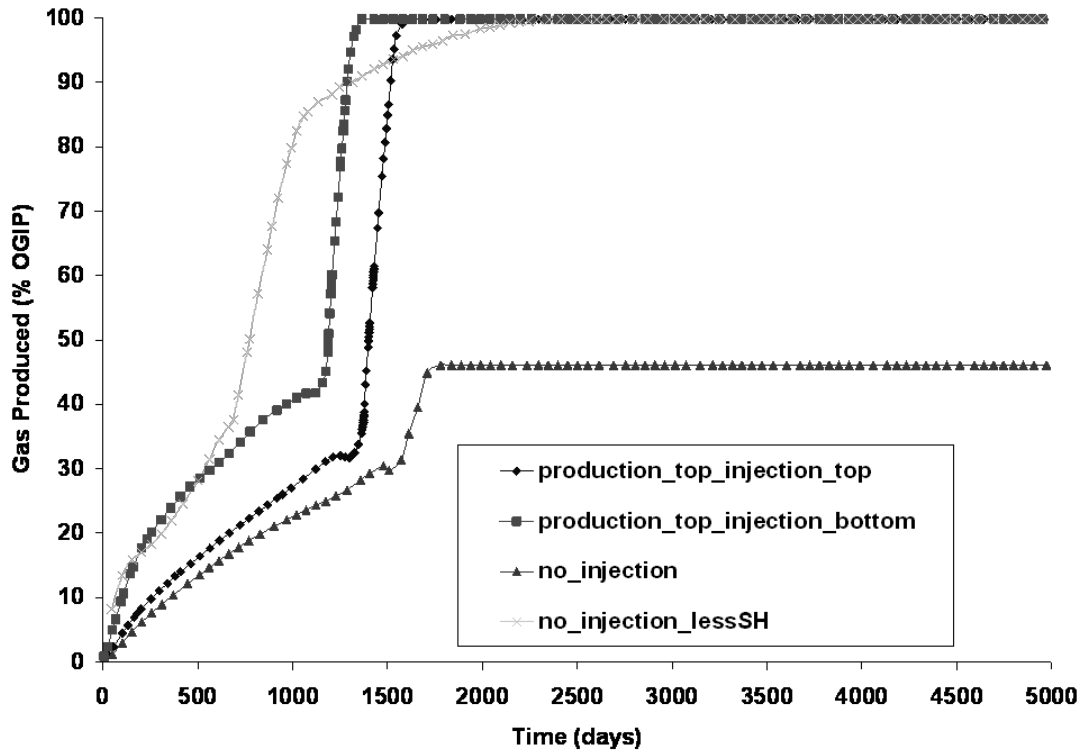


Figure 7.6: Cumulative gas production for dipping reservoir

Figure 7.6 shows the cumulative gas production using different well configurations. The production curves for the cases 'production_top_injection_top' and 'production_top_injection_bottom' are comparable. In both these cases initial production is due to depressurization at the production well. Figure 7.7 shows the hydrate saturation profiles after 1200 days for both the cases. For the case 'production_top_injection_top' the depressurization front is about to reach the aquifer layer after which the production rate increases. In the case 'production_top_injection_bottom' the depressurization dissociation front has reached the aquifer and the warm water flow becomes easy after that in the hydrate bearing zone and hence the production rate increases.

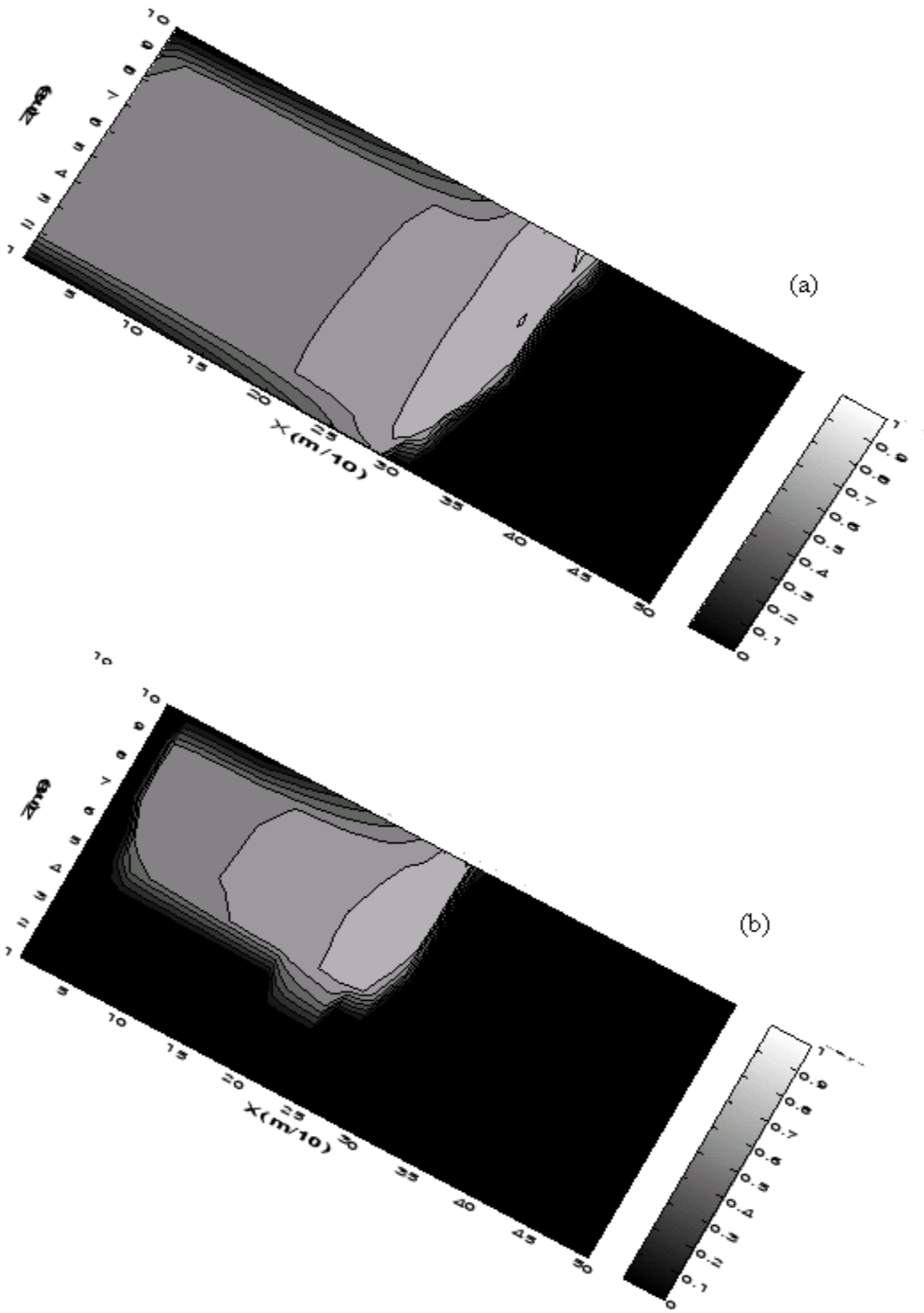


Figure 7.7: Hydrate saturation profile after 1200 days for (a) 'production_top_injection_top' and (b) 'production_top_injection_bottom'

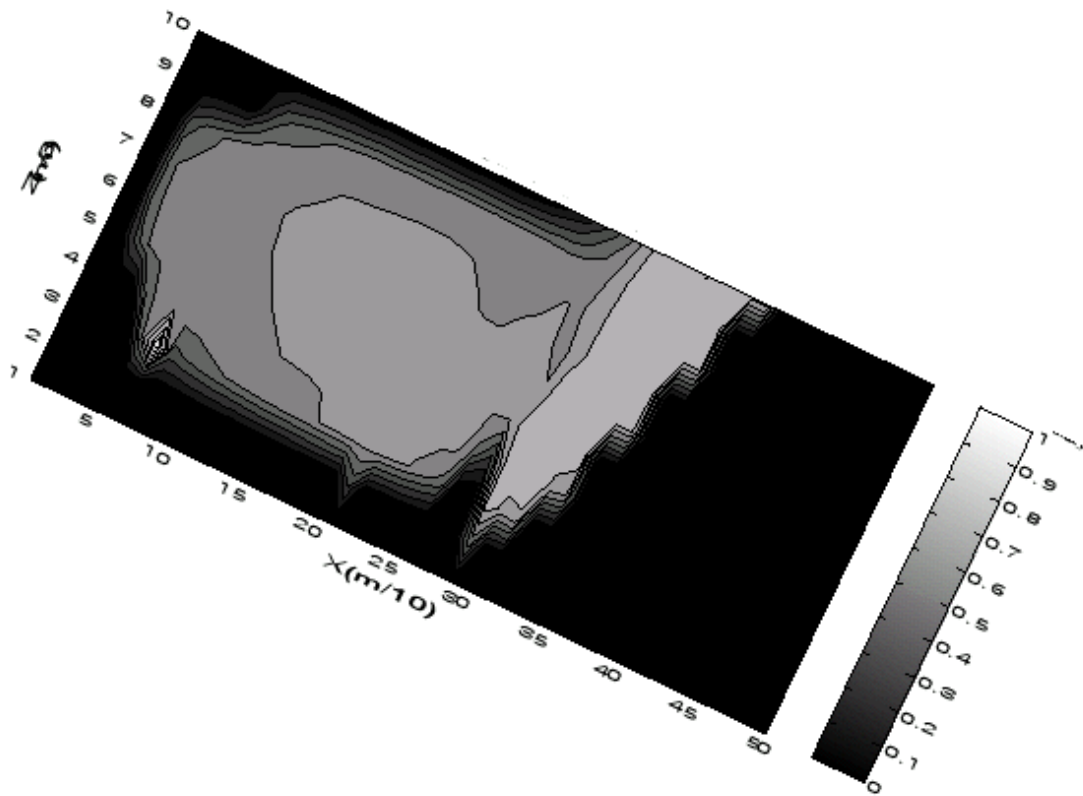


Figure 7.8: Hydrate saturation profile after 5000 days for 'no_injection'

In the 'no_injection' case initially the production is similar to the other two cases till the depressurization front reaches the aquifer. But in the no injection case no warm water is available to heat the reservoir. The channels of water zone formed along the periphery bypass the hydrate bearing zone due to its low permeability and production stops after 45% of OGIP is produced. Figure 7.8 shows the hydrate saturation profile after 5000 days.

When the saturation of hydrate is low, then depressurization is effective as the permeability of hydrate bearing zone is not as low as in the case of 0.75 hydrate saturation. So, in the low hydrate saturation case 'no_injection_lessSH' we are able to produce 100% of the original gas in place.

For dipping reservoirs, depressurization is not effective in limited aquifer if the hydrate saturation is high. The cumulative production and production rates are similar if the injection well is on the hydrate water contact zone.

Conclusions

Three types of reservoirs have been studied to find the optimum production strategy for different conditions. For the horizontal reservoir if the aquifer attached is at the under-burden and large then depressurization is ineffective. The injection well should be near the aquifer zone for the mobility of the water injected. The position and the orientation of the production well are not that important as the production is due to thermal stimulation by warm water injection. Horizontal wells are better as they increase the area of warm water reach. More injection wells can be used for increasing the production rate and cumulative production for a field.

When the aquifer is limited and on the down dip side of the reservoir, the reservoir can be depressurized but the warm water injection is necessary for high production rate. Aquifer helps to mobilize the hot water injected. For limited aquifer case, the distance between the injection and

production well should be increased so that water channel bypassing the hydrate bearing sediments does not form.

When we have a dipping formation the production well should be at the top and the injection well should be on the contact of hydrate and water zones for optimum production.

Thus in all the cases discussed, the injection well should be on the contact of hydrate and water zones for high production rate, the production well should be on the top of the hydrate bearing layer. The distance between the production well and the injection well should be optimized based on the hydrate saturation and the aquifer size.

Future Work

In the last 6 months we have also added CO₂ as a component to the present simulator and are simulating core scale displacement of methane by CO₂.

Task 8: Seafloor and Borehole Stability

Summary

Our efforts have been entirely on Subtask 8.2: Sediment (In)Stability. The two-dimensional geological accumulations models (Task 6) include stability calculations and we are ready to begin simulating the general conditions for failure and apply them to field cases. We have benchmarked our 2D accumulations against 1D solutions, so a parameter study on stability is the next step. Our advancements on instability have isolated the effects of fracturing on hydrate accumulation via 1D models based on fluid flux, multi-phase fluid flow, sediment properties (Subtask 8.1). We are now looking at transient effects of fracturing and will soon start looking at how fracturing mechanisms may contribute to geophysical anomalies because of their effects on heterogeneous hydrate accumulations. We continue to collaborate with colleagues, especially those with field data, to allow integration of our models with field studies (Subtask 8.3). This includes collaborations with the University of Texas at Austin Institute for Geophysics (UTIG) in an effort to understand transient fluid flow, instability, and gas discharge at Hydrate Ridge and with the University of Victoria and Geological Survey of Canada to look at hydrate-related failures (Lopez slide, Slipstream slide) at Cascadia.

Milestone Status

8.2c Conditions for (in)stability – We are nearly completed disseminating the research results on 1D instability related to gas hydrate accumulations (Daigle and Dugan, 2010; Daigle and Dugan, in press; Daigle and Dugan, in review). In the coming months we will focus on 2D failure problems and publish results on general failure problems and applications to field data. 2D results will be completed by mid-2011.

Subtask 8.2: Modeling (In)stability

Introduction

At the pore scale, sediment physical properties exert a strong influence on hydrate formation and distribution [Clennell *et al.*, 1999]. Many investigations have focused on the nature of these influences theoretically [e.g., Clennell *et al.*, 1999; Henry *et al.*, 1999; Turner *et al.*, 2005; Sun and Mohanty, 2006; Anderson *et al.*, 2009; Jain and Juanes, 2009; Kvamme *et al.*, 2009] and in the laboratory [e.g., Handa and Stupin, 1992; Uchida *et al.*, 1999; Tohidi *et al.*, 2001; Uchida *et al.*, 2002; Anderson *et al.*, 2003a; Anderson *et al.*, 2003b; Uchida *et al.*, 2004; Hyodo *et al.*, 2005; Lee *et al.*, 2007; Yun *et al.*, 2007; Lee *et al.*, 2008; Masui *et al.*, 2008]. Sediment physical properties can influence hydrate distribution by influencing fluid flow pathways, which affects methane supply, and by changing the local conditions for hydrate stability. Permeable layers can act as preferential conduits for flow of methane gas and methane-charged pore water [e.g., Weinberger and Brown, 2006], making these layers preferential sites for hydrate formation. This effect has been invoked to explain preferential hydrate occurrence in sand layers on scales of 10-100 m [e.g., Boswell *et al.*, 2010; Dai *et al.*, in press]. At the pore scale, fine-grained sediments can inhibit hydrate formation through capillary-induced freezing point depression [e.g., Clennell *et al.*, 1999]; this effect is known as the Gibbs-Thomson effect. We focus on the Gibbs-Thomson effect because it has recently been invoked to explain cm-scale partitioning of hydrates in coarse-grained turbidite layers [Torres *et al.*, 2008; Malinverno, 2010], and thus influences pore pressure distribution and fracturing. This represents an important modeling step to move beyond the steady-state stability assumptions that have been made in previous models [e.g., Rempel and Buffett, 1997; Xu and Ruppel, 1999; Davie and Buffett, 2001; Nimblett and Ruppel, 2003; Bhatnagar *et al.*, 2007; Daigle and Dugan, in press].

We extend the model of Daigle and Dugan [in press] to include solubility changes in fine-grained sediments caused by the Gibbs-Thomson effect. This new model simulates 1-D flow of a

constant fluid flux through a layered porous medium with alternating silt and clay layers. We include poromechanical coupling to allow hydraulic fracturing if pore pressure exceeds the minimum horizontal stress. Pore pressure increase is computed from Darcy's law as hydrate occludes the sediment pore space using our assumption of constant flux. We apply this model to two locations where hydrates have been observed preferentially filling thin, coarser-grained layers: Hydrate Ridge offshore Oregon (Ocean Drilling Program (ODP) Leg 204 Site 1250), and northern Cascadia offshore Vancouver Island (Integrated Ocean Drilling Program (IODP) Expedition 311 Site U1325). We show that after 10,000 years, thin silt layer at Hydrate Ridge fill with hydrate and increased pore pressure causes fractures to form through the intervening clay layers. This hydrate distribution matches the heuristic model proposed for hydrate accumulation at Hydrate Ridge [Weinberger *et al.*, 2005; Weinberger and Brown, 2006] and the time scale is consistent with sediment ages [Chevallier *et al.*, 2006]. At northern Cascadia, we predict that 2×10^5 years are required to match the hydrate saturation in the silt layers, and that the intervening clays do not fracture. The lack of fractures is consistent with observations from image logs, but the time scale is too long given constraints on sediment ages [Riedel *et al.*, 2006]. Hydrate accumulation at this site is likely enhanced by in situ production of biogenic methane in the clays [Malinverno, 2010]. We use our methodology to determine the maximum thickness of hydrate-free clay layers between silts; the set of sediment physical properties and methane supply rates necessary to produce hydrate-filled silt layers connected by fractured clays; and the conditions required for sediments to experience capillary-induced shutdown of hydrate formation as hydrate constricts pores and drives solubility upwards. Our results outline the conditions required to develop hydrate-filled silts interbedded with hydrate-free clays, and to develop throughgoing fractures through the clays. This work provides insight into the processes controlling hydrate formation in sediments of different pore sizes and helps advance our understanding of lithologically-partitioned methane hydrate accumulations.

Model details

When a liquid undergoes a phase change to the solid state in a small (micro- to nanometer-scale) pore, the resulting solid particle has a high surface area to volume ratio, and the solid-liquid interfacial energy becomes an important contribution to the total Gibbs free energy of the system. In porous media, the activity of the remaining liquid in the pore decreases because of adsorption of liquid molecules onto the pore walls [Handa and Stupin, 1992; Clennell *et al.*, 1999]. The decreased liquid activity and increased Gibbs free energy increases the solubility of the solid phase in the liquid and depresses the freezing point of the solid [Thomson, 1871; Porter and Easterling, 1992], and has been observed in laboratory experiments involving dissociation of methane hydrate [e.g., Handa and Stupin, 1992; Berge *et al.*, 1999; Uchida *et al.*, 1999; Winters *et al.*, 1999; Tohidi *et al.*, 2001; Uchida *et al.*, 2002; Anderson *et al.*, 2003a; Anderson *et al.*, 2003b; Uchida *et al.*, 2004; Anderson *et al.*, 2009]. The freezing point depression ΔT_f [K] can be computed by [Anderson *et al.*, 2009]

$$\Delta T_f = -T_{f,b} \frac{F \gamma_{sl}}{r \rho_s \Delta H_{sl}}, \quad (\text{Equation 1})$$

where $T_{f,b}$ is the freezing point in free liquid [K], F is a geometric factor that depends on interfacial curvature, γ_{sl} is the interfacial energy between the solid and liquid phases [J m^{-2}], r is the pore radius [m], ρ_s is the bulk density of the solid phase [kg m^{-3}], and ΔH_{sl} is the latent heat of fusion of the solid phase [J mol^{-1}]. The geometric factor F is related to the curvature of the solid-liquid interface by

$$F = r \left(\frac{1}{r_1} + \frac{1}{r_2} \right), \quad (\text{Equation 2})$$

where r_1 and r_2 are orthogonal radii of curvature [m]. In spherical and cylindrical pores, $r_1 = r_2 = r$ so $F = 2$ [Anderson *et al.*, 2009]. In methane hydrate systems, the depression in freezing point results in an increase in methane solubility at constant temperature and pressure [Davie and Buffett, 2001].

We simulate one-dimensional flow of pore water with dissolved methane upwards through a porous medium (Figure 2). We prescribe seafloor depth and temperature d_{sf} [m] and T_{sf} [K], and a constant geothermal gradient dT/dz [K m⁻¹]. These parameters define the thickness of the RHSZ along with assumptions of hydrostatic conditions at the seafloor and seawater salinity (3.35% by mass) through the RHSZ. The model domain is a 1-20 m-thick subsection of the RHSZ. We assign porosity ϕ and grain radius r_g [m] in the model domain. We assume that the porous medium can be represented by a packing of uniform spheres and compute permeability k [m²] using the formula of *Bryant et al.* [1993a] where $k = 0.00272r_g^2$. This assumption results in non-spherical pores. We assume that the pore radius in Equation 1 can be represented by the radius of an inscribed sphere in the pore, an assumption made by other investigations of spherical packs [e.g., *Prodanović and Bryant*, 2006; *Behseresht*, 2008]. Fluid flow is assigned a constant value, and the pore pressure in excess of hydrostatic is computed from Darcy's law and the permeability values. We assume that constant fluid flow is a reasonable approximation for short length and time scales.

For simplicity, we assume that the pores in the system are bounded by tetrahedra composed of four grains (Figure 1b). The radius of the pore in such a system is given by $(1-\sqrt{2})r_g$. We compute the triple point temperature for dissolved methane-methane hydrate-methane gas equilibrium T_{3P} [K] at in situ temperature and pressure using the method of *Duan et al.* [1992]. We then compute the change in T_{3P} due to the Gibbs-Thomson effect using Equation 1 with $F = 2$, $\gamma_{sl} = 0.027$ J m⁻² [*Clennell et al.*, 1999], $\rho_s = 925$ kg m⁻³, and $\Delta H = 5.45 \times 10^4$ J mol⁻¹ [*Waite et al.*, 2009]. Using the Gibbs-Thomson-corrected T_{3P} , we compute methane solubility in the RHSZ using the method of *Bhatnagar et al.* [2007].

Hydrate formation is computed by solving a mass balance for methane, assuming that methane is only present as hydrate or dissolved in the pore water:

$$\frac{\partial}{\partial t} [\phi(1 - S_h)\rho_w c_m^l + \phi S_h c_m^h \rho_h] - \frac{\partial}{\partial z} [\bar{\mathbf{q}}_f |c_m^l \rho_w|] = \frac{\partial}{\partial z} \left[\phi(1 - S_h) D_m \rho_w \frac{\partial c_m^l}{\partial z} \right], \quad (\text{Equation 3})$$

where S_h is hydrate saturation, ρ_w and ρ_h are the bulk densities of water and hydrate [kg m⁻³], c_m^l and c_m^h are the mass fractions of methane in water and hydrate [kg kg⁻¹], $\bar{\mathbf{q}}_f$ is the rate of fluid flow [m s⁻¹], and D_m is the coefficient of diffusion for methane in water [m² s⁻¹]. We assume $\rho_w = 1024$ kg m⁻³, $\rho_h = 925$ kg m⁻³ [*Waite et al.*, 2009], $c_m^h = 0.134$ kg kg⁻¹, and $D_m = 10^{-9}$ m² s⁻¹ [*Davie and Buffett*, 2001]. We solve Equation 3 using an explicit, forward-in-time, centered-in-space (FTCS) finite-difference scheme with the initial condition $c_m^l = 0$ and $S_h = 0$ throughout the domain, and the boundary conditions that c_m^l is 0 at the seafloor and is the value for solubility in free water at the base of the domain.

As hydrate forms in the porous medium, the pore system is occluded, reducing the permeability. We assume the hydrate forms a uniform coating around the sediment grains analogous to an isopachous cement (Figure 1a). Following the cementation model of *Bryant et al.* [1993b] we compute the reduced permeability k' [m²] as

$$k' = k(1 - S_h)^4. \quad (\text{Equation 4})$$

This permeability model results in more rapid permeability reduction with hydrate saturation than the cylindrical pore-coating model that has been used in other investigations [e.g., *Kleinberg et al.*, 2003; *Nimblett and Ruppel*, 2003; *Liu and Flemings*, 2007; *Crutchley et al.*, 2010; *Daigle and Dugan*, in press], but a less rapid reduction than the cylindrical pore-filling model (Figure 3) [*Kleinberg et al.*, 2003]. As hydrate forms and pore space is occluded, our assumption of constant fluid flux results in an increase in pore fluid pressure. In addition to the reduction in permeability, the pore radius is also reduced as a result of hydrate formation by a factor of $(1 - S_h)^{1/3}$, such that the reduced pore radius is

$(1 - \sqrt{2})(1 - S_h)^{1/3} r_g$. We continually update T_{3P} and methane solubility for changes in pore fluid pressure and pore radius.

We include poroelastic coupling to investigate whether the Gibbs-Thomson effect can produce a hydrate distribution characterized by hydrate filling the pore space in coarser-grained intervals and hydrate-filled fractures in finer-grained intervals. Hydraulic fracturing can be approximated as an elastic phenomenon. For a non-cohesive sediment with zero tensile strength, hydraulic fracturing will occur when the pore pressure exceeds the minimum principal stress [Valkó and Economides, 1995]. In passive margins and shallow sediments of active margins, the maximum principal stress is typically vertical and the minimum principal stress horizontal. We compute σ_{vh}' [Pa], the vertical effective stress under hydrostatic conditions, at each depth by integrating the buoyant unit weight from the seafloor to that depth. Assuming linear elasticity, the horizontal effective stress under hydrostatic conditions σ_{hh}' [Pa] is related to σ_{vh}' by

$$\sigma_{hh}' = \frac{\nu}{1 - \nu} \sigma_{vh}', \quad (\text{Equation 5})$$

where ν is Poisson's ratio. For fractures to form, P^* must overcome σ_{hh}' . The overpressure ratio λ^* is the ratio of P^* to σ_{vh}' :

$$\lambda^* = \frac{P^*}{\sigma_{vh}'} = \frac{\nu}{1 - \nu} \frac{P^*}{\sigma_{hh}'}. \quad (\text{Equation 6})$$

By combining Equations 5 and 6, when $P^* = \sigma_{hh}'$, fracturing occurs; thus the fracture criterion is that $\lambda^* \geq \frac{\nu}{1 - \nu}$. We assume $\nu = 0.4$, which is a typical value for loosely consolidated silt or clay [e.g., Karig and Hou, 1992; Reynolds, 1997]. This results in a fracture criterion of $\lambda^* \geq 0.67$.

Once fractures form, we compute the equivalent fracture permeability by

$$k = \frac{a^3}{12l}, \quad (\text{Equation 7})$$

where a is the fracture aperture [m] and l is the inter-fracture spacing of the fracture system [m] [Snow, 1968]; we assume that the fracture system that forms has $a = 1$ mm and $l = 1$ m [e.g., Weinberger and Brown, 2006; Cook et al., 2008]. Because the fracture width is large compared to the size of pores, the methane solubility in the fractures is reduced to the value in free water (i.e. no capillary effects). If hydrate forms in the fractures, the fracture aperture is decreased by a factor of $1 - S_h$, and the expression for reduced permeability in the fracture system is

$$k' = k(1 - S_h)^3. \quad (\text{Equation 8})$$

Our assumption of cohesionless sediment with zero tensile strength may introduce small errors into the results. Tensile strength of soft sediments may range from 0 to 0.05 MPa, and cohesion is typically less than 0.5 MPa [Behrmann, 1991; Day, 1992]. Including these effects would result in higher pore pressure necessary for fractures to form. This effect is most important at higher hydrate saturations ($S_h > 0.40$) [Yun et al., 2007] and certain hydrate habits (e.g. cementing at grain contacts). In general, by neglecting tensile strength and cohesion the time scales we compute are minimum endmembers.

Results

Hydrate Ridge

Our Hydrate Ridge model is based on ODP Leg 204 Site 1250, located near the crest of southern Hydrate Ridge. We assume $d_{sf} = 800$ m, $T_{sf} = 277$ K, and $dT/dz = 0.053$ K m⁻¹ [Tréhu, 2006]. The model domain consists of a 5 m-thick section with its base at 100 mbsf, composed of alternating layers of 1.5 m-thick clay and 0.25 m-thick silt. This is representative of a zone with lithologically partitioned hydrate identified on image logs from Hole 1250B [Weinberger and Brown, 2006]. To

determine silt and clay porosities, we used the gamma ray log from Site 1250 to differentiate silt and clay using a cutoff value of 60 GAPI (silt < 60 GAPI < clay). We then determined porosities by taking the average values of the bulk density log over the silt and clay zones and computing porosity assuming a grain density of 2700 kg m^{-3} . This yielded $\phi = 0.55$ in silt and $\phi = 0.52$ in clay. Grain sizes were determined from median grain size and silt content at Site 1250 [Gràcia *et al.*, 2006]; this yielded a silt grain diameter of $30 \text{ }\mu\text{m}$ and a clay grain diameter of $0.5 \text{ }\mu\text{m}$. The corresponding initial permeabilities using $k = 0.000272r_g^2$ [Bryant *et al.*, 1993a] were $6 \times 10^{-13} \text{ m}^2$ in silt and $2 \times 10^{-16} \text{ m}^2$ in clay, which agree with laboratory measurements of permeability by Tan *et al.* [2006]. We assume a flow rate of 430 mm yr^{-1} , which is in the range $300\text{-}1000 \text{ mm yr}^{-1}$ inferred near the crest of Hydrate Ridge from porewater chloride concentration profiles [Torres *et al.*, 2002].

After 2000 years, $S_h \approx 0.90$ in both silt layers, and no hydrate has accumulated in the intervening clay layers (Figure 4a). As a result of hydrate forming in the silt and occluding the pore space, methane solubility in the silt layers increases by $\sim 0.015 \text{ g kg}^{-1}$ (Figure 4b). The lowermost clay layer develops throughgoing fractures; λ^* equals the fracture criterion from the base of the domain to the top of this clay layer, and fractures begin forming in the next clay layer at 98.25 mbsf, bypassing the intervening silt layer (Figure 4c). Solubility in the fractured clay drops to the value in free water (Figure 4b); the increase in solubility in the unfractured clay is a result of the increase in pore fluid pressure as hydrate occludes pores in the overlying silt layer, reducing the silt permeability. After 10,000 years, the middle clay layer (96.75-98.25 mbsf) develops throughgoing fractures (Figure 4c). Solubility in the silts increases an additional 0.01 g kg^{-1} due to further formation of hydrate (Figure 4b).

Hydrate accumulates first at the base of the lower silt. The accumulation rate decreases with time and S_h is nearly constant after 1800 years (Figure 4d). This is due to fractures opening in the clay layer below the lowermost silt. Prior to fracture formation, hydrate cannot form in the clay because the solubility is too high, so the pore fluid flow through the clay without any decrease in dissolved methane concentration and enters the base of the silt layer with sufficient dissolved methane for hydrate to precipitate in the silt. However, methane solubility in fractures is lower than in the silts, so hydrate will form in the fractures, and the pore fluid entering the base of the silt will no longer have enough dissolved methane to allow hydrate formation in the silt. Solubility in the lower silt increases slowly at first (Figure 4e), but the rate increases rapidly when $S_h > 0.80$. This is due to the fact that the pore throats are constricted most rapidly at high S_h , driving solubility upwards because of the Gibbs-Thomson effect.

Northern Cascadia

Our northern Cascadia model is based on IODP Expedition 311 Site U1325, which is located in a depositional basin $\sim 11 \text{ km}$ landward from the deformation front. We assume $d_{sf} = 2195 \text{ m}$, $T_{sf} = 276 \text{ K}$, and $dT/dz = 0.06 \text{ K m}^{-1}$ [Riedel *et al.*, 2006]. The model domain consists of a 7.6 m -thick section with its base at 200 mbsf, composed of alternating 2.5 m -thick clay layers and 0.05 m -thick silt layers. This is representative of the conditions in the turbidite sequence containing lithologically-bound hydrates [Malinverno, 2010]. We assumed silt and clay porosities of 0.35 and 0.60, and silt and clay grain diameters of $80 \text{ }\mu\text{m}$ and $16 \text{ }\mu\text{m}$ [Torres *et al.*, 2008]; despite the larger grain sizes, we refer to these as “silt” and “clay” for comparison with Hydrate Ridge and the heuristic model of Weinberger *et al.* [2005]. The corresponding silt and clay permeabilities from $k = 0.000272r_g^2$ [Bryant *et al.*, 1993a] were $4 \times 10^{-12} \text{ m}^2$ and $2 \times 10^{-13} \text{ m}^2$. Vertical fluid flow rates in this area have been estimated at between 0.17 mm yr^{-1} [Malinverno *et al.*, 2008] and 1 mm yr^{-1} [Bekins and Dreiss, 1992; Wang *et al.*, 1993]; we consider the upper limit to obtain a minimum estimate of time.

After 2×10^5 years, $S_h \approx 0.40$ in the silts (Figure 5), which matches the range $S_h = 0.20\text{-}0.60$ obtained from log data in the silt layers [Malinverno *et al.*, 2008]. Unlike Hydrate Ridge, λ^* remains very small (Figure 5c), and the clay layers in northern Cascadia do not develop fractures. This is due to the combination of high permeability and low flow rate [e.g., Daigle and Dugan, in press]. Hydrate accumulates steadily in the lowermost silt (Figure 5d) but causes almost no solubility increase (Figure

5e). This is due to the large pore size. Even with $S_h = 0.40$, the pore space remains large enough that the triple point depression is very small ($\sim 0.01\%$ in the clays), so the change in solubility is negligible.

Conclusions

We considered changes in three-phase equilibrium temperature and solubility due to the Gibbs-Thomson effect in a 1-D model of hydrate formation from methane supplied by pore fluid advection. We applied this model to Hydrate Ridge and northern Cascadia, two field sites where hydrate has been observed preferentially in thin, coarser-grained layers in the sedimentary column. In both cases, increased solubility in the clay layers is sufficient to inhibit hydrate formation in the clays, resulting in hydrate formation only in the silt layers. However, 2×10^5 years are required at northern Cascadia to generate the observed hydrate saturations due to low fluid advection rates. We conclude that hydrate formation at this site is enhanced by in situ production of biogenic methane in the clay layers, which is then transported into the silt layers by diffusive flux as modeled by *Malinverno* [2010]. At Hydrate Ridge, advective methane transport is rapid enough to fill the silt layers almost completely with hydrate after 10,000 years, a reasonable time scale given constraints on sediment age [*Chevallier et al.*, 2006] and the age of the current configuration of the hydrate stability zone [*Bangs et al.*, 2005]. Our predicted hydrate saturations are significantly higher than saturations inferred from log and porewater chlorinity data, but this may be due to the spatial resolution of tools or transient fluid pulses that allow fractures to form at lower S_h . Development of fractures in the clay layers limits hydrate formation in the silts by allowing hydrate to form in the fractures, thus removing dissolved methane from the water exiting the fractured clay layers. Fractures develop through the clay layers at Hydrate Ridge, but no fractures develop at northern Cascadia; this difference in behavior is driven by contrasts in permeability and flow rate between the two sites. Our work helps advance our understanding of these feedbacks and our general understanding of factors that control hydrate accumulation and distribution.

Ongoing and future work

We are working with Nathan Bangs of the Institute for Geophysics at the University of Texas at Austin to model the effects of transient gas pressure in the methane gas reservoir beneath the summit of southern Hydrate Ridge. Two collocated seismic surveys acquired 8 years apart at Hydrate Ridge offshore Oregon, USA, showed migration of free gas in a permeable conduit, Horizon A, that feeds the summit of southern Hydrate Ridge. The surveys also revealed differences in the location and flux of active gas venting to the water column. We propose that episodic gas migration and pressure fluctuations in the reservoir underlying the regional hydrate stability zone (RHSZ) at southern Hydrate Ridge influence methane supply pathways to the RHSZ and are linked with periodic fracturing and release of methane into the water column by complex feedback processes. We model the effect of pore pressure variations within the deep methane source on fracturing behavior with a 1D model coupling multiphase flow, hydrate accumulation, and pore pressure buildup. Fractures open when the pore pressure exceeds the fracture criterion, which we assume is the vertical effective stress. We define a rate of pressure increase and a maximum pressure. The rate of pressure increase determines the time required to reach the fracture criterion, and the pressure increase rate and maximum pressure determine how long fractures will remain open once they form. Once fractures open, the gas pressure is depleted quickly because the high gas pressure drives rapid gas flux through the fracture system. This results in gas venting at the seafloor and accumulation of hydrate in the fracture system. If the amplitude of pressure oscillation is near the vertical effective stress in Horizon A (~ 0.87 MPa) and the time for pressure increase is on the order of years, the gas pressure will meet the fracture criterion on a time scale of months to a few years. The high gas pressure is then depleted over a time scale of a few months. Thus we conclude that gas migration pathways at southern Hydrate Ridge may evolve on a time scale of months to years. This provides

important constraints on the time scale of transient effects on the methane hydrate system at southern Hydrate Ridge, and illustrates how pore pressure pulses affect fluid flow and fracturing behavior in active methane hydrate provinces. We will present our results at the International Conference on Gas Hydrates in July 2011 in Edinburgh.

Presentations and Abstracts

- Daigle, H., 2010, Lithologically partitioned hydrates in advective systems, Gordon Research Conference: Natural Gas Hydrate Systems, Waterville, ME (6-11 June 2010).
- Daigle, H., Dugan, B., 2010. Free gas in the methane hydrate stability zone: Implications for hydrate distribution and fracture behavior. 2010 Fall Meeting, American Geophysical Union, San Francisco, CA (17 December 2010).
- Daigle, H., Bangs, N., Dugan, B., 2011. Transient pressures, hydraulic fracturing, and gas migration at southern Hydrate Ridge: Geophysical observations and flow modeling. 7th International Conference on Gas Hydrates, International Conference on Gas Hydrates, Edinburgh, Scotland, 17-21 July 2011.
- Dugan, B., 2010, Continuum Models of Large-Scale Phenomena Associated with Hydrate-Bearing Sediments, Gordon Research Conference: Natural Gas Hydrate Systems, Waterville, ME (6-11 June 2010).
- Scholz, N., Riedel, M., Spence, G., Dugan, B., Daigle, H., Hyndman, R.D., James, T.S., Naegeli, K., 2010. Slope failure of continental frontal ridges offshore Vancouver Island, British Columbia. 2010 Fall Meeting, American Geophysical Union, San Francisco, CA (13 December 2010).

Publications

- Daigle, H., Dugan, B., 2010, Effects of multiphase methane supply on hydrate accumulation and fracture generation, *Geophysical Research Letters*, 37, L20301, doi:10.1029/2010GL044970.
- Daigle, H., Dugan, B., in press, Origin and evolution of fracture-hosted methane hydrate deposits, *Journal of Geophysical Research*, doi:10.1029/2010JB007492.
- Daigle, H., Dugan, B., in review, Capillary controls on methane hydrate distribution and fracturing in advective systems, *Geochemistry, Geophysics, Geosystems*.

References

- Anderson, R., Llamedo, M., Tohidi, B., and R.W. Burgass (2003a), Experimental measurement of methane and carbon dioxide clathrate hydrate equilibria in mesoporous silica, *J. Phys. Chem. B*, 107(15), 3507-3514, doi:10.1021/jp0263370.
- Anderson, R., Llamedo, M., Tohidi, B., and R.W. Burgass (2003b), Characteristics of clathrate hydrate equilibria in mesopores and interpretation of experimental data, *J. Phys. Chem. B*, 107(15), 3506-3509, doi:10.1021/jp0263368.
- Anderson, R., Tohidi, B., and J.B.W. Webber (2009), Gas hydrate growth and dissociation in narrow pore networks: Capillary inhibition and hysteresis phenomena, in *Sediment-Hosted Gas Hydrates: New Insights on Natural and Synthetic Systems*, *Geol. Soc. London Spec. Pub. Ser.*, vol. 319, edited by D. Long et al., pp. 145-159, The Geological Society, London.

- Archer, D., and B. Buffett (2005), Time-dependent response of the global ocean clathrate reservoir to climatic and anthropogenic forcing, *Geochem. Geophys. Geosyst.*, 6(3), Q03002 doi:10.1029/2004GC000854.
- Bangs, N.L., Musgrave, R.L., and A.M. Tréhu (2005), Upward shifts in the Southern Hydrate Ridge gas hydrate stability zone following postglacial warming, offshore Oregon, *J. Geophys. Res.*, 110, B03102, doi:10.1029/2004JB003293.
- Behrmann, J.H. (1991), Conditions for hydrofracture and the fluid permeability of accretionary wedges, *Earth Planet. Sci. Lett.*, 107, 550-558.
- Bekins, B.A., and S.J. Dreiss (1992), A simplified analysis of parameters controlling dewatering in accretionary prisms, *Earth Planet. Sci. Lett.*, 109, 275-287.
- Berge, L.I., Jacobsen, K.A., and A. Solstad (1999), Measured acoustic wave velocities of R11 (CCl₃F) hydrate samples with and without sand as a function of hydrate concentration, *J. Geophys. Res.*, 104(B7), 15415-15424.
- Behseresht, J. (2008), Infinite-Acting Physically Representative Networks for Capillarity-Controlled Displacements, M.S. thesis, Dept. of Petrol. and Geosystems Eng., Univ. of Texas, Austin, TX, USA.
- Bhatnagar, G., Chapman, W.G., Dickens, G.R., Dugan, B., and G.J. Hirasaki (2007), Generalization of gas hydrate distribution and saturation in marine sediments by scaling of thermodynamic and transport processes, *Am. J. Sci.*, 307, 861-900, doi:10.2475/06.2007.01.
- Boswell, R., Collett, T.S., McConnell, D., Frye, M., Shedd, W., Mrozewski, S., Guerin, G., Cook, A., Shelander, D., Dai, J., Godfriaux, P., Dufrene, R., Jones, E., and R. Roy (2010), Gulf of Mexico Gas Hydrates Joint Industry Project: Overview of Leg II LWD results, paper presented at 2010 Offshore Technology Conference, Offshore Tech. Conf., Houston, TX.
- Bryant, S.L., King, P.R., and D.W. Mellor (1993a), Network model evaluation of permeability and spatial correlation in a real random sphere packing, *Transport Porous Med.*, 11, 53-70.
- Bryant, S.L., Mellor, D.W., and C.A. Cade (1993b), Physically representative network models of transport in porous media, *AIChE J.*, 39(3), 387-396.
- Chevallier, J., Tréhu, A.M., Bangs, N.L., Johnson, J.E., and H.J. Meyer (2006), Seismic sequence stratigraphy and tectonic evolution of southern Hydrate Ridge, edited by A.M. Tréhu et al., *Proc. Ocean Drill. Program Sci. Results*, 204, 1-29, doi:10.2973/odp.proc.sr.204.121.2006.
- Clennell, M.B., Hovland, M., Booth, J.S., Henry, P., and W.J. Winters (1999), Formation of natural gas hydrates in marine sediments 1: Conceptual model of gas hydrate growth conditioned by host sediment properties, *J. Geophys. Res.*, 104(B10), 22985-23003.
- Collett, T.S. (1992), Potential of gas hydrates outlined, *Oil Gas J.*, 90(25), 84-87.

- Cook, A.E., Goldberg, D., and R.L. Kleinberg (2008), Fracture-controlled gas hydrate systems in the northern Gulf of Mexico, *Mar. Petrol. Geol.*, 25(9), 932-941, doi:10.1016/j.marpetgeo.2008.01.013.
- Crutchley, G.J., Geiger, S., Pecher, I.A., Gorman, A.R., Zhu, H., and S.A. Henrys (2010), The potential influence of shallow gas and gas hydrates on sea floor erosion of Rock Garden, an uplifted ridge offshore New Zealand, *Geo-Mar. Lett.*, doi:10.1007/s00367-010-0186-y.
- Dai, S., Lee, C., and J.C. Santamarina (in press), Formation history and physical properties of sediments from the Mount Elbert gas hydrate stratigraphic test well, Alaska North Slope, *Mar. Petrol. Geol.*, doi:10.1016/j.marpetgeo.2010.03.005.
- Daigle, H., and B. Dugan (in press), Origin and evolution of fracture-hosted methane hydrate deposits, *J. Geophys. Res.*, doi:10.1029/2010JB007492.
- Davie, M.K., and B.A. Buffett (2001), A numerical model for the formation of gas hydrate below the seafloor, *J. Geophys. Res.*, 106(B1), 497-514.
- Day, R.W. (1992), Effective cohesion for compacted clay, *J. Geotech. Eng.*, 118(4), 611-619.
- Dickens, G.R., Castillo, M.M., and J.C. G. Walker (1997), A blast of gas in the latest Paleocene: Simulating first-order effects of massive dissociation of oceanic methane hydrate, *Geology*, 25(3), 259-262.
- Dillon, W.P., Danforth, W.W., Hutchinson, D.R., Drury, R.M., Taylor, M.H., and J.S. Booth (1998), Evidence for faulting related to dissociation of gas hydrate and release of methane off the southeastern United States, in *Gas Hydrates: Relevance to World Margin Stability and Climate Change*, *Geological Society Special Publication 137*, edited by J.-P. Henriot and J. Mienert, pp. 293-302, The Geological Society, London.
- Duan, Z., Møller, N., Greenberg, J., and J.H. Weare (1992), The prediction of methane solubility in natural waters to high ionic strength from 0 to 250°C and from 0 to 1600 bar, *Geochim. Cosmochim. Acta*, 56, 1451-1460.
- Gràcia, E., Martínez-Ruiz, F., Piñero, E., Larrasoña, J.C., Vizcaino, A., and G. Ercilla (2006), Data report: Grain-size and bulk and clay mineralogy of sediments from the summit and flanks of southern Hydrate Ridge, Sites 1244-1250, ODP Leg 204, edited by A.M. Tréhu et al., *Proc. Ocean Drill. Program Sci. Results*, 204, 1-19, doi:10.2973/odp.proc.sr.204.110.2006.
- Handa, Y.P., and D. Stupin (1992), Thermodynamic properties and dissociation characteristics of methane and propane hydrates in 70-Å-radius silica gel pores, *J. Phys. Chem.*, 96(21), 8599-8603.
- Hyodo, M., Nakata, Y., Yoshimoto, N., and T. Ebinuma (2005), Basic research on the mechanical behavior of methane hydrate-sediments mixture, *Soils Found.*, 45(1), 75-85.

- Karig, D.E., and G. Hou (1992), High-stress consolidation experiments and their geologic implications, *J. Geophys. Res.*, 97(B1), 289-300.
- Kleinberg, R.L., Flaum, C., Griffin, D.D., Brewer, P.G., Malby, G.E., Peltzer, E.T., and J.P. Yesinowski (2003), Deep sea NMR: Methane hydrate growth habit in porous media and its relationship to hydraulic permeability, deposit accumulation, and submarine slope stability, *J. Geophys. Res.*, 108(B10), 2508, doi:10.1029/2003JB002389.
- Kvamme, B., Graue, A., Buanes, T., Kuznetsova, T., and G. Ersland (2009), Effects of solid surfaces on hydrate kinetics and stability, in *Sediment-Hosted Gas Hydrates: New Insights on Natural and Synthetic Systems*, *Geol. Soc. London Spec. Pub. Ser.*, vol. 319, edited by D. Long et al., pp. 131-144, The Geological Society, London.
- Kvenvolden, K.A. (1993), Gas hydrates – geological perspective and global change, *Rev. Geophys.*, 31(2), 173-187.
- Lee, J.Y., Santamarina, J.C., and C. Ruppel (2008), Mechanical and electromagnetic properties of northern Gulf of Mexico sediments with and without THF hydrates, *Mar. Petrol. Geol.*, 25(9), 884-895, doi:10.1016/j.marpetgeo.2008.01.019.
- Lee, J.Y., Yun, T.S., Santamarina, J.C., and C. Ruppel (2007), Observations related to tetrahydrofuran and methane hydrates for laboratory studies of hydrate-bearing sediments, *Geochem. Geophys. Geosyst.*, 8(6), Q06003, doi:10.1029/2006GC001531.
- Liu, X., and P.B. Flemings (2007), Dynamic multiphase flow model of hydrate formation in marine sediments, *J. Geophys. Res.*, 112, B03101, doi:10.1029/2005JB004227.
- Malinverno, A. (2010), Marine gas hydrates in thin sand layers that soak up microbial methane, *Earth Planet. Sci. Lett.*, 292, 399-408, doi:10.1016/j.epsl.2010.02.008.
- Malinverno, A., Kastner, M., Torres, M.E., and U.G. Wortmann (2008), Gas hydrate occurrence from pore water chlorinity and downhole logs in a transect across the northern Cascadia margin (Integrated Ocean Drilling Program Expedition 311), *J. Geophys. Res.*, 113, B08103, doi:10.1029/2008JB005702.
- Masui, A., Miyazaki, K., Haneda, H., Ogata, Y., and K. Aoki (2008), Mechanical characteristics of natural and artificial gas hydrate bearing sediments, paper 5697 presented at 6th International Conference on Gas Hydrates, Int. Conf. on Gas Hydrates, Vancouver, British Columbia, Canada.
- Nimblett, J., and C. Ruppel (2003), Permeability evolution during the formation of gas hydrates in marine sediments, *J. Geophys. Res.*, 108(B9), 2420, doi:10.1029/2001JB001650.
- Porter, D.A., and K.E. Easterling (1992), *Phase Transformations in Metals and Alloys*, 514 pp., Chapman and Hall, London.

- Prodanović, M., and S.L. Bryant (2006), A level set method for determining critical curvatures for drainage and imbibitions, *J. Colloid Interface Sci.*, 304(2), 442-458, doi:10.1016/j.jcis.2006.08.048.
- Rempel, A.W., and B.A. Buffett (1997), Formation and accumulation of gas hydrate in porous media, *J. Geophys. Res.*, 102(B5), 10151-10164.
- Reynolds, J.M. (1997), *An Introduction to Applied and Environmental Geophysics*, 796 pp., John Wiley and Sons, Chichester, England.
- Riedel, M., Collett, T.S., Malone, M.J., and Expedition 311 Scientists (2006), *Proceedings of the Integrated Ocean Drilling Program Expedition 311*, Integrated Ocean Drill. Program, Washington, DC.
- Snow, D.T. (1968), Rock fracture spacings, openings, and porosities, *J. Soil Mech. Found. Div. Am. Soc. Civ. Eng.*, 94(SM1), 73-91.
- Sun, X., and K.K. Mohanty (2006), Kinetic simulation of methane hydrate formation and dissociation in porous media, *Chem. Eng. Sci.*, 61(11), 3476-3495, doi:10.1016/j.ces.2005.12.017.
- Tan, B., Germaine, J.T., and P.B. Flemings (2006), Data report: Consolidation and strength characteristics of sediments from ODP Site 1244, Hydrate Ridge, Cascadia continental margin, edited by A.M. Tréhu et al., *Proc. Ocean Drill. Program Sci. Results*, 204, 1-148, doi:10.2973/odp.proc.sr.204.102.2006.
- Thomson, W. (1871). On the equilibrium of vapour at a curved surface of liquid, *Philos. Mag.*, 42(282), 448-452, doi:10.1080/14786447108640606.
- Tohidi, B., Anderson, R., Clennell, M.B., Burgass, R.W., and A.B. Biderkab (2001), Visual observation of gas-hydrate formation and dissociation in synthetic porous media by means of glass micromodels, *Geology*, 29(9), 867-870, doi:10.1130/0091-7613(2001)029<0867:VOOGHF>2.0.CO;2.
- Torres, M.E., McManus, J., Hammond, D.E., de Angelis, M.A., Heeschen, K.E., Colbert, S.L., Tryon, M.D., Brown, K.M., and E. Suess (2002), Fluid and chemical fluxes in and out of sediments hosting methane hydrate deposits on Hydrate Ridge, OR, II: Hydrological provinces, *Earth Planet. Sci. Lett.*, 201, 525-540.
- Torres, M.E., Tréhu, A.M., Cespedes, N., Kastner, M., Wortmann, U.G., Kim, J.-H., Long, P., Malinverno, A., Pohlmann, J.W., Riedel, M., and T. Collett (2008), Methane hydrate formation in turbidite sediments of northern Cascadia, IODP Expedition 311, *Earth Planet. Sci. Lett.*, 271, 170-180, doi:10.1016/j.epsl.2008.03.061.
- Tréhu, A.M. (2006), Subsurface temperatures beneath southern Hydrate Ridge, edited by A.M. Tréhu et al., *Proc. Ocean Drill. Program Sci. Results*, 204, 1-26, doi:10.2973/odp.proc.sr.204.114.2006.

- Tréhu, A.M., Ruppel, C., Holland, M., Dickens, G.R., Torres, M.E., Collett, T.S., Goldberg, D., Riedel, M., and P. Schultheiss (2006), Gas hydrates in marine sediments: Lessons from scientific ocean drilling, *Oceanography*, 19(4), 124-142.
- Turner, D.J., Cherry, R.S., and E.D. Sloan (2006), Sensitivity of methane hydrate equilibria to sediment pore size, *Fluid Phase Equilib.*, 228-229, 505-510, doi:10.1016/j.fluid.2005.09.025.
- Uchida, T., Ebinuma, T., and T. Ishizaki (1999), Dissociation condition measurements of methane hydrate in confined small pores of porous glass, *J. Phys. Chem. B*, 103(18), 3659-3662, doi:10.1021/jp984559l.
- Uchida, T., Ebinuma, T., Takeya, S., Nagao, J., and H. Narita (2002), Effects of pore sizes on dissociation temperatures and pressures of methane, carbon dioxide, and propane hydrates in porous media, *J. Phys. Chem. B*, 106(4), 820-826, doi:10.1021/jp012823w.
- Uchida, T., Takeya, S., Chuvilin, E.M., Ohmura, R., Nagao, J., Yakushev, V.S., Istomin, V.A., Minagawa, H., Ebinuma, T., and Narita, H. (2004), Decomposition of methane hydrates in sand, sandstone, clays, and glass beads, *J. Geophys. Res.*, 109, B05206, doi:10.1029/2003JB002771.
- Valkó, P., and M.J. Economides (1995), *Hydraulic Fracture Mechanics*, 298 pp., John Wiley and Sons, Chichester, England.
- Waite, W.F., Santamarina, J.C., Cortes, D.D., Dugan, B., Espinoza, D.N., Germaine, J., Jang, J., Jung, J.W., Kneafsey, T.J., Shin, H., Soga, K., Winters, W.J., and T.-S. Yun (2009), Physical properties of hydrate-bearing sediments, *Rev. Geophys.*, 47, RG4003, doi:10.1029/2008RG000279.
- Wang, K., Hyndman, R.D., and E.E. Davis (1993), Thermal effects of sediment thickening and fluid expulsion in accretionary prisms: Model and parameter analysis, *J. Geophys. Res.*, 98(B6), 9975-9984.
- Weinberger, J.L., and K.M. Brown (2006), Fracture networks and hydrate distribution at Hydrate Ridge, Oregon, *Earth Planet. Sci. Lett.*, 245, 123-136, doi:10.1016/j.epsl.2006.03.012.
- Weinberger, J.L., Brown, K.M., and P.E. Long (2005), Painting a picture of gas hydrate distribution with thermal images, *Geophys. Res. Lett.*, 32, L04609, doi:10.1029/2004GL021437.
- Winters, W.J., Dallimore, S.R., Collett, T.S., Katsube, T.J., Jenner, K.A., Cranston, R.E., Wright, J.F., Dixon, F.M., and T. Uchida (1999), Physical properties of sediments from the JAPEX/JNOC/GSC Mallik 2L-38 gas hydrate research well, *Geol. Surv. Can. Bull.*, 544, 95-100.
- Xu, W., and C. Ruppel (1999), Predicting the occurrence, distribution, and evolution of methane gas hydrate in porous marine sediments, *J. Geophys. Res.*, 104(B3), 5081-5095.

Yun, T.S., Santamarina, J.C., and C. Ruppel (2007), Mechanical properties of sand, silt, and clay containing tetrahydrofuran hydrate, *J. Geophys. Res.*, 112, B04106, doi:10.1029/2006JB004484.

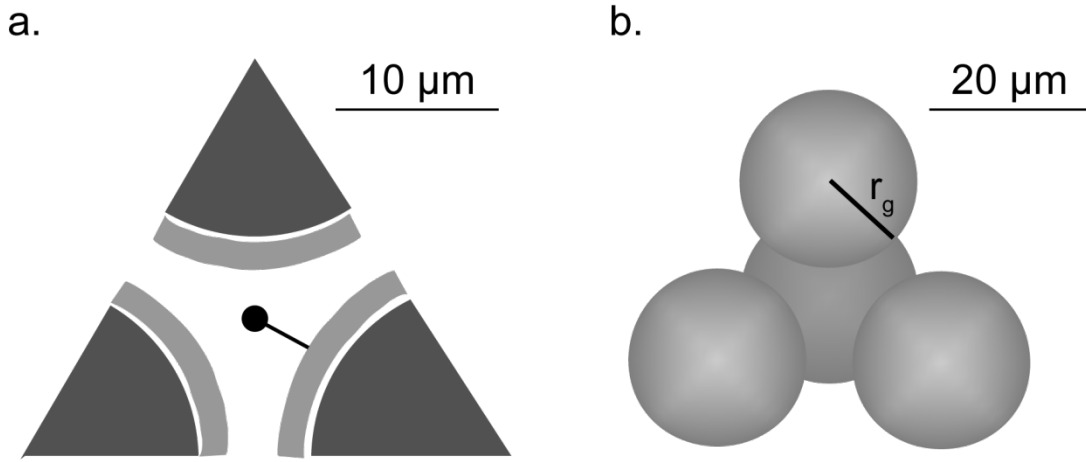


Figure 1. (a) Cross-section through a plane defined by the centers of three adjacent grains showing hydrate growth habit and pore size. Hydrate is assumed to grow as a uniform coating around the grains with a thin film of water between hydrate and grain. The pore radius is shown by the black line normal to the surface of the hydrate. Hydrate growth occurs inward towards the center of the pore. (b) Illustration of pore surrounded by four spherical grains. The grains have radius r_g .

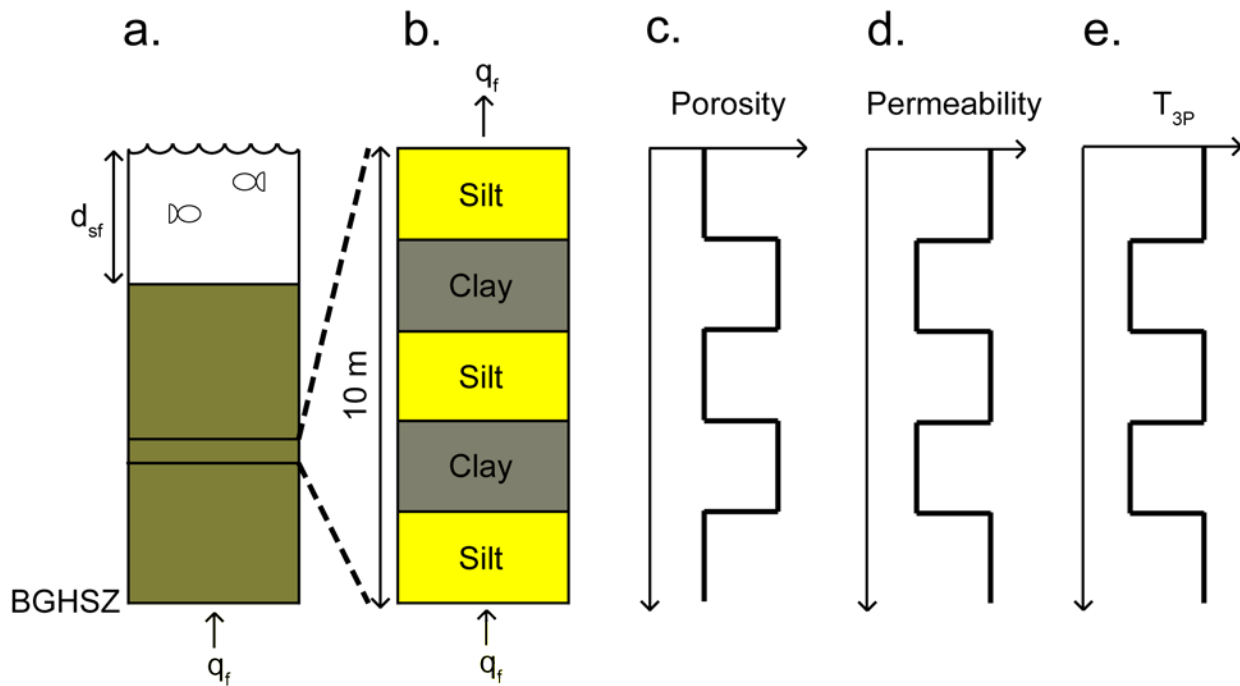


Figure 2. Illustration of model domain. (a) We first define a seafloor depth, seafloor temperature, and geothermal gradient, which in turn define the depth to the base of the gas hydrate stability zone (BGHSZ). (b) Fluid flows at a constant rate q_f into the base of the system. We select a smaller section of the RHSZ for modeling, and define thicknesses of silt and clay layers. We assign porosity (c) and initial permeability (d) in each layer. The grain size in each layer determines the change in the methane triple point temperature $\Delta(T_{3P})$ from the Gibbs-Thomson effect (Equation 1), which we subtract from the free water triple point temperature to obtain the initial triple point temperature (T_{3P}) curve (e).

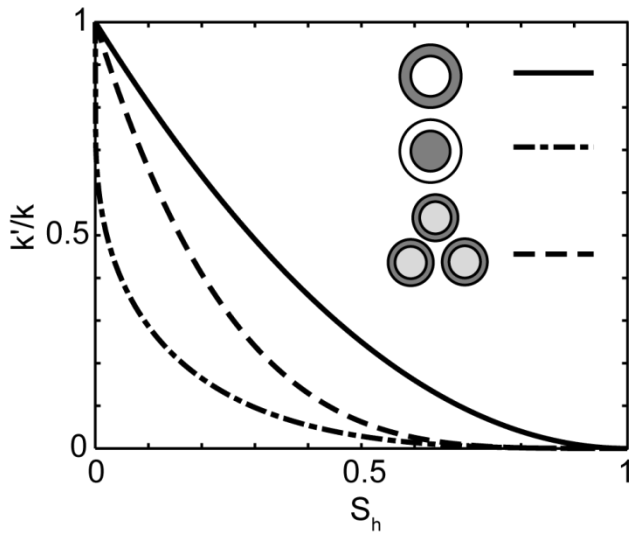


Figure 3. Permeability reduction k'/k with increased hydrate saturation S_h for three different pore models. Solid line: cylindrical pores with hydrate coating the pore walls uniformly (Equation B10 of *Kleinberg et al.* [2003]). Dashed-dotted line, cylindrical pores with hydrate forming in the middle of the pores (Equation B14 of *Kleinberg et al.* [2003]). Dashed line: hydrate forming an isopachous cement on spherical grains (Equation 4). We use this isopachous cement model as the representation of the pore space because it is more realistic than parallel, cylindrical capillary tubes. The permeability reduction at a given S_h for this model is greater than for the cylinder wall-coating model but less than for the cylinder pore-filling model.

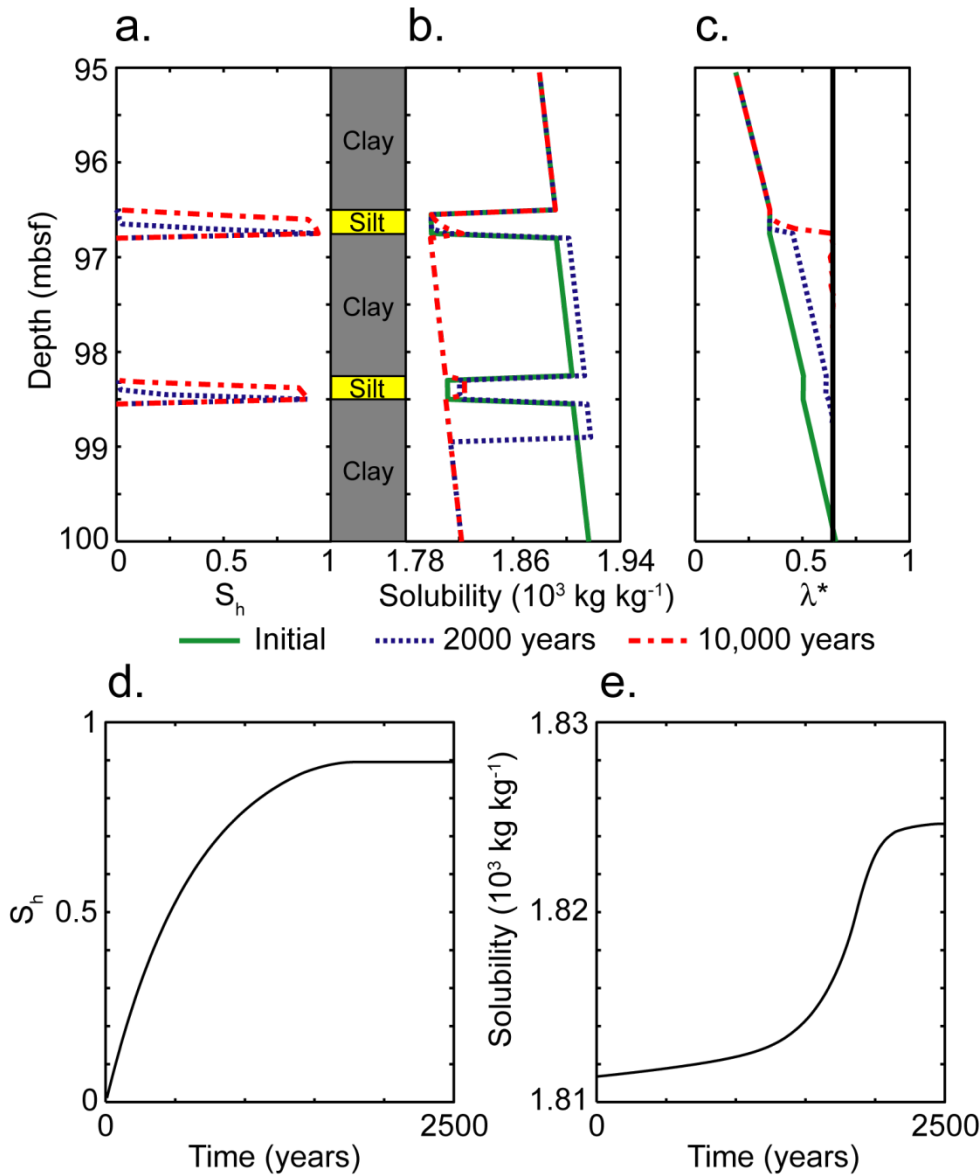


Figure 4. Model results for Hydrate Ridge. (a) Hydrate saturation. Both silt layers fill with hydrate to $S_h \approx 0.90$ after 2000 years, with little increase in S_h between 2000 and 10,000 years. This is attributable to fractures opening in the clays after 2000 years and hydrate forming in the fracture system, reducing the amount of dissolved methane that reaches the silts. (b) Methane solubility in the pore fluid. Initially the solubility in the clays is greater than that in the silts. After 2000 years, hydrate has formed in the silts and the solubility has increased slightly; the solubility in the clays has increased slightly as well due to the increase in pore fluid pressure as hydrate occludes the pore space in the silts. Fractures have developed over the lowest 1 m of the lower clay layer, and the solubility values reflect this as they have decreased to the value for free water. After 10,000 years, solubility in the silts has increased slightly again as some additional hydrate has formed; fractures have developed in the clays up to the base of the upper silt layer, and the solubility in this interval has dropped accordingly. (c) Overpressure ratio. The critical value is marked by the solid line at $\lambda^* = 0.67$. After 2000 years, the lowest 1 m of the system has reached the fracture criterion; after 10,000 years, the clays up to the base of the upper silt have reached the fracture criterion, but the lower silt remains slightly below the fracture criterion. (d) Hydrate saturation versus time in the lower silt layer. S_h increases rapidly for ~ 1800 years, when fractures form and reduce the amount of methane reaching the silt layer. After this point, S_h increases very slowly. (e) Change in solubility versus time in the lower silt. The solubility increase that results from hydrate clogging the pores is small until $S_h \approx 0.80$, but solubility increases rapidly after this point as the pore space is occluded more quickly.

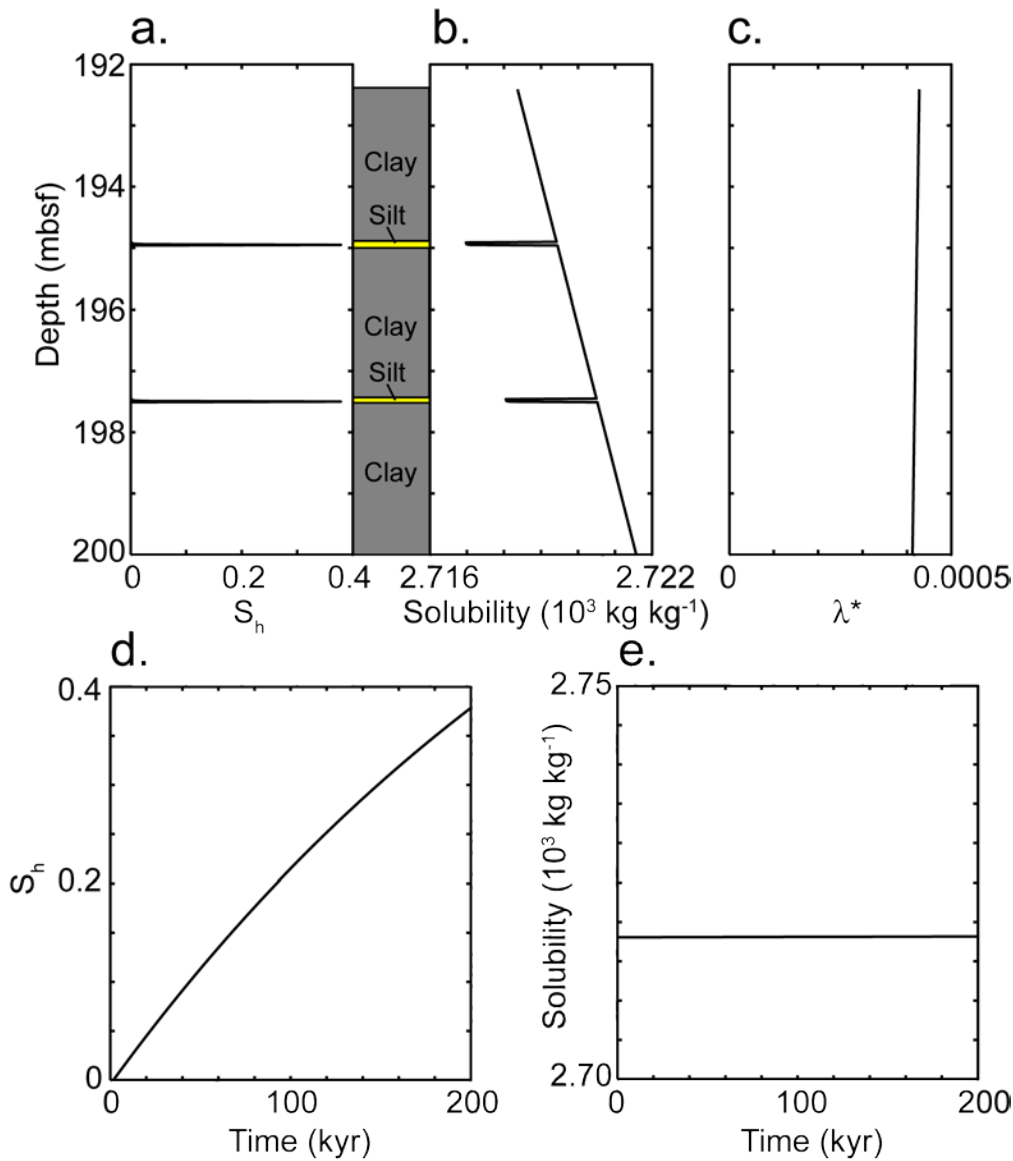


Figure 5. Model results for northern Cascadia after 2×10^5 years. (a) Hydrate saturation. S_h reaches nearly 0.40 in both silt layers, which matches observations [Malinverno *et al.*, 2008]. No hydrate forms in the intervening clays. (b) Methane solubility in the pore fluid. There is almost no change in solubility from the initial conditions. This is due to the relatively large pore sizes at this site; not even filling the pore space to $S_h = 0.40$ reduces the pore size sufficiently to cause an appreciable change in solubility. (c) Overpressure ratio. The high permeability and low flow rate at this site result in very low λ^* . After 2×10^5 years, the system is not close to failure. (d) Hydrate saturation versus time in the lower silt layer. S_h increases nearly linearly with time; this rate is controlled by the low pore fluid flow rate since methane is only supplied by pore fluid flux. (e) Solubility in the lower silt layer versus time. The solubility value remains nearly constant because of the large pore size.

Task 9.0: Geophysical Imaging

2010-2011 Mid-Year Report

Priyank Jaiswal¹ and Colin A. Zelt²

¹Oklahoma State University

²Rice University

Milestone Chart

Task	Date	Status
9.1 Preliminary processing and inversion of seismic data.	08/08 – 08/09	Completed.
9.2: Final 1-D elastic and 2-D acoustic waveform inversion.	08/09 – 08/10	2-D acoustic inversion completed. Full task completion anticipated by 12/10
9.3: Rock physics modeling (in collaboration with other groups funded by DOE)	08/10 – 08/11	On target

Summary:

We have performed full-waveform inversion in this period. Although we had completed traveltimes inversion and depth migration in Year 1, we found it necessary to revisit the model and re-create it with 20% more traveltimes picks to improve its overall resolution. The resolution improvement enabled us to a) reconcile observations in three wells that were drilled near the seismic line; and b) start the waveform inversion from the lowest usable frequency of 8 Hz. The waveform inversion was implemented in frequency domain. Five groups of frequencies, each group comprising 3 frequencies separated by 0.4 Hz, were inverted beginning from 8Hz up to 15Hz. In an ongoing study, the preferred waveform model is being assessed using checkerboard tests and their overall geological sensibility. For interpretation purposes velocities within the hydrate stability zone are considered proportional to hydrate concentration; higher velocities imply higher hydrate concentration. The preferred waveform model show lateral velocity variation within the hydrate stability zone probably due to variation in hydrate concentration. A combination of waveform model and depth image indicates that in parts of model that have structural discontinuities, hydrates may have a preferred orientation. The reasons for a preferred orientation are currently unknown and under investigation.

Study Area

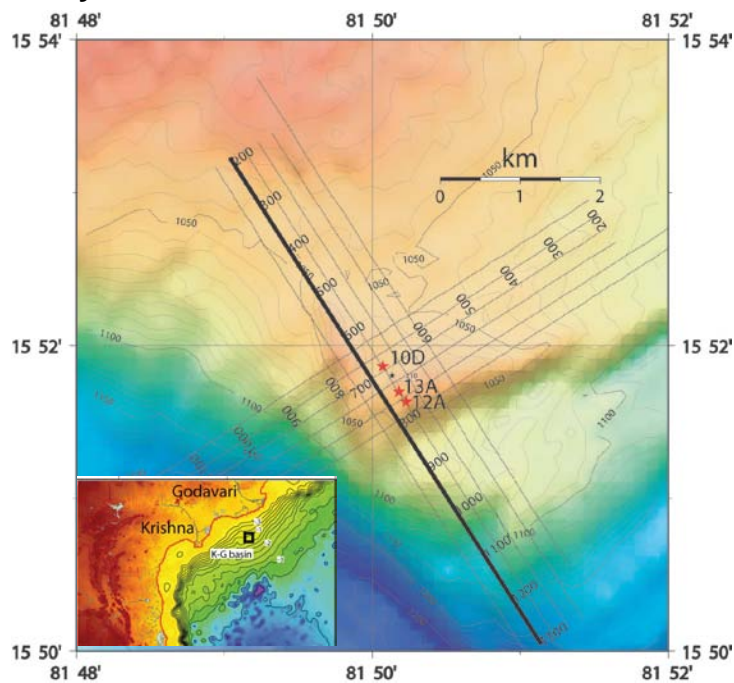


Figure 1. Bathymetry map of the study area. Location with respect to the Indian east-coast is shown in inset. Seismic line released for this study by Indian Govt. is shown in bold. Other available survey lines for future release are shown in grey. Wells 10D, 13A, and 12A, were logged/cored during NGHP-01 expedition. Data from these wells are in public domain.

Observation in wells 10D, 12A, and 13A

From the NGHP-01 well report released by the Govt. of India, following inferences relevant to our subtask are as follows:

1. None of the three wells (10D, 12A, and 13A) showed any obvious lithological control on hydrate distribution.
2. Of the three wells only 10D penetrated the BSR; no free-gas was encountered.
3. Well 12A which was drilled 500m SE of 10D could only be cored (no logging was done). Chlorinity analysis suggests hydrates in 10D do not extend to 12A
4. In the de-pressurization test, 12A recovered ~20% of hydrates as compared to 10D.
5. Well 13A which was drilled 150m SE of 10D could only be logged (no cores were available). The volume of hydrates in 13A was similar to that in 10D.

Traveltime Inversion and Pre-Stack Depth Migration

The composite inversion-migration method used in this work is same as the Unified Imaging (UI) method developed by [Jaiswal and Zelt, 2008]. This method estimates a structurally consistent velocity and reflectivity model starting with standard processing methods. UI, in this work, is essentially a composite of reflection tomography and Kirchoff's pre-stack depth migration (PSDM).

UI begins with generation of the stack (Figure 2) using the best possible stacking velocity model and interpretation of events to be used in inversion. Interpretation of the stacked data (Figure 2) is inverted as zero-offsets arrival times. The stacking velocity model is converted to depth using Dix's smooth gradient method [Dix, 1955], V_{el0} (Figure 3a). This model is used for depth migration and identifying the same events that were interpreted in the stacked data. Following this, wide-angle traveltimes corresponding to these reflectors are picked in the raw shot gathers. The geometry of the reflectors for inversion of wide angle data are interpretation of the depth migrated images (Figure 4).

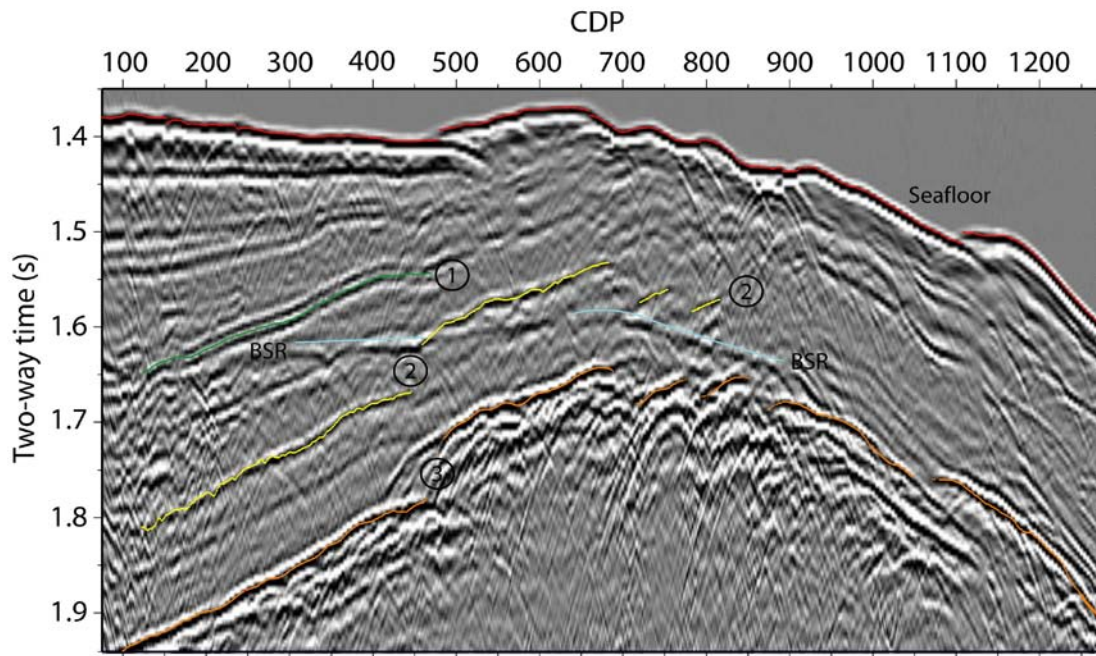


Figure 3. Stacked data. Seafloor, and reflectors labeled 1 – 3 are used in inversion. The BSR is interpreted in blue and is not used in inversion.

By inverting the wide-angle traveltimes, UI updates the interval velocity model. Repeated cycles of traveltime inversion and depth migration are performed; a “cycle” refers to a single run of joint inversion followed by depth migration. The horizons are modeled as floating reflectors [Zelt, 1999]. The updated velocity model is then used for depth migration and zero-offset inversion. For the zero-offset inversion, the velocity model is maintained stationary. The interpreted horizons are compared with the corresponding inverted horizons by computing their normalized RMS distance, j . In case this distance is found to exceed unity, the updated velocity model and interpretation from the current cycle is used as the initial velocity model and horizon depths for the next cycle. The cycles are repeated until a value of unity is achieved for j . In this paper three cycles were required for j to converge to unity.

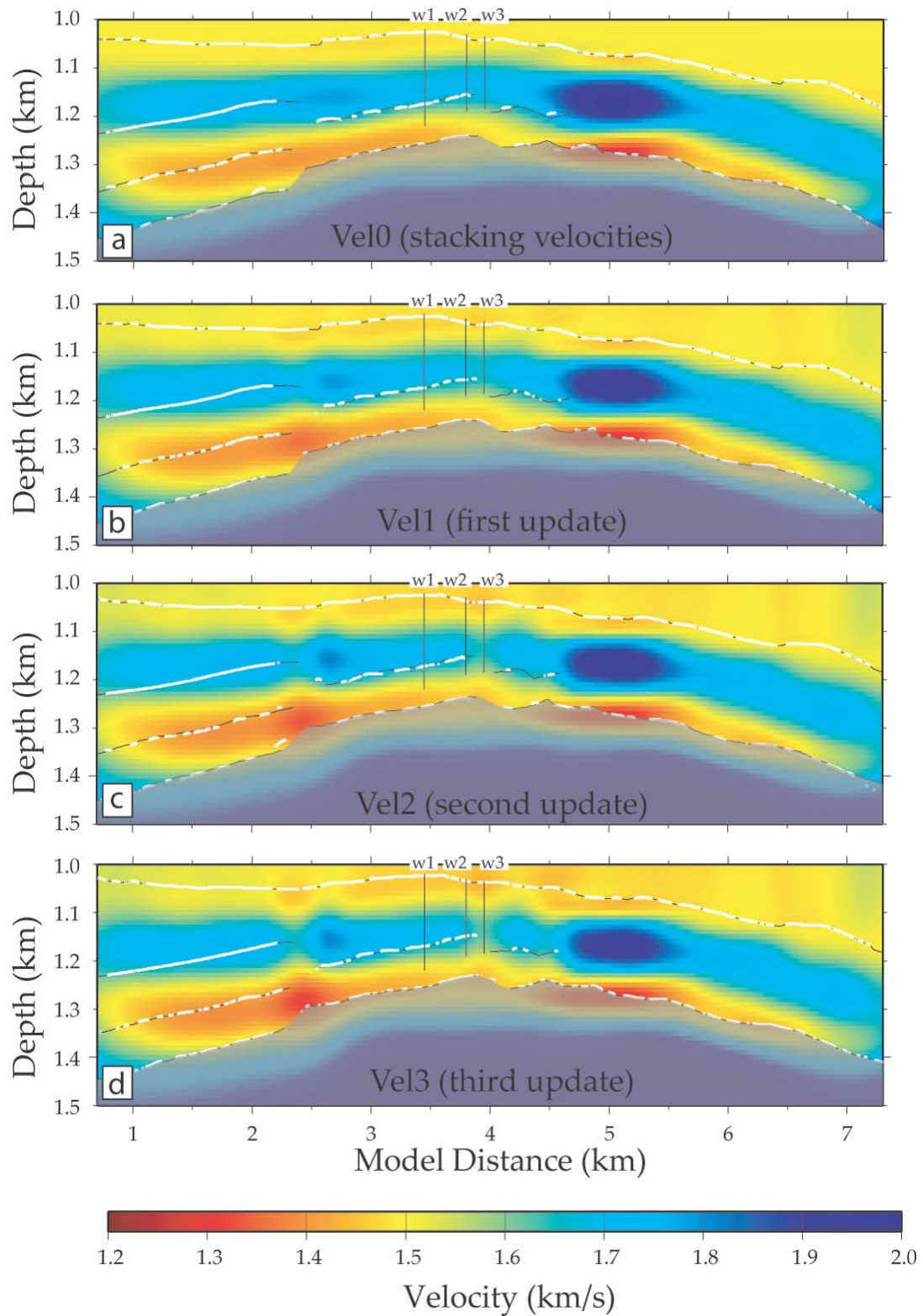


Figure 3. Velocity models from composite inversion-migration method. A) Starting velocity model from conventional processing. B) – D) Updated models from inversion of reflection traveltimes. In A) – D) the horizons picked for inversion are shown in with solid black line. The inverted horizons are overlaid in white. Model in d) is considered preferred as the picked and inverted horizons have reasonable overlap. In A–D, parts of the model not covered by rays are shaded in grey. W1 – 3 represent wells 10D, 13A, and 12A respectively. As observed in the cores, 10D and 13A (W1 and W2) appear to sample the same hydrate patch while 12A (W3) appears to be disconnected.

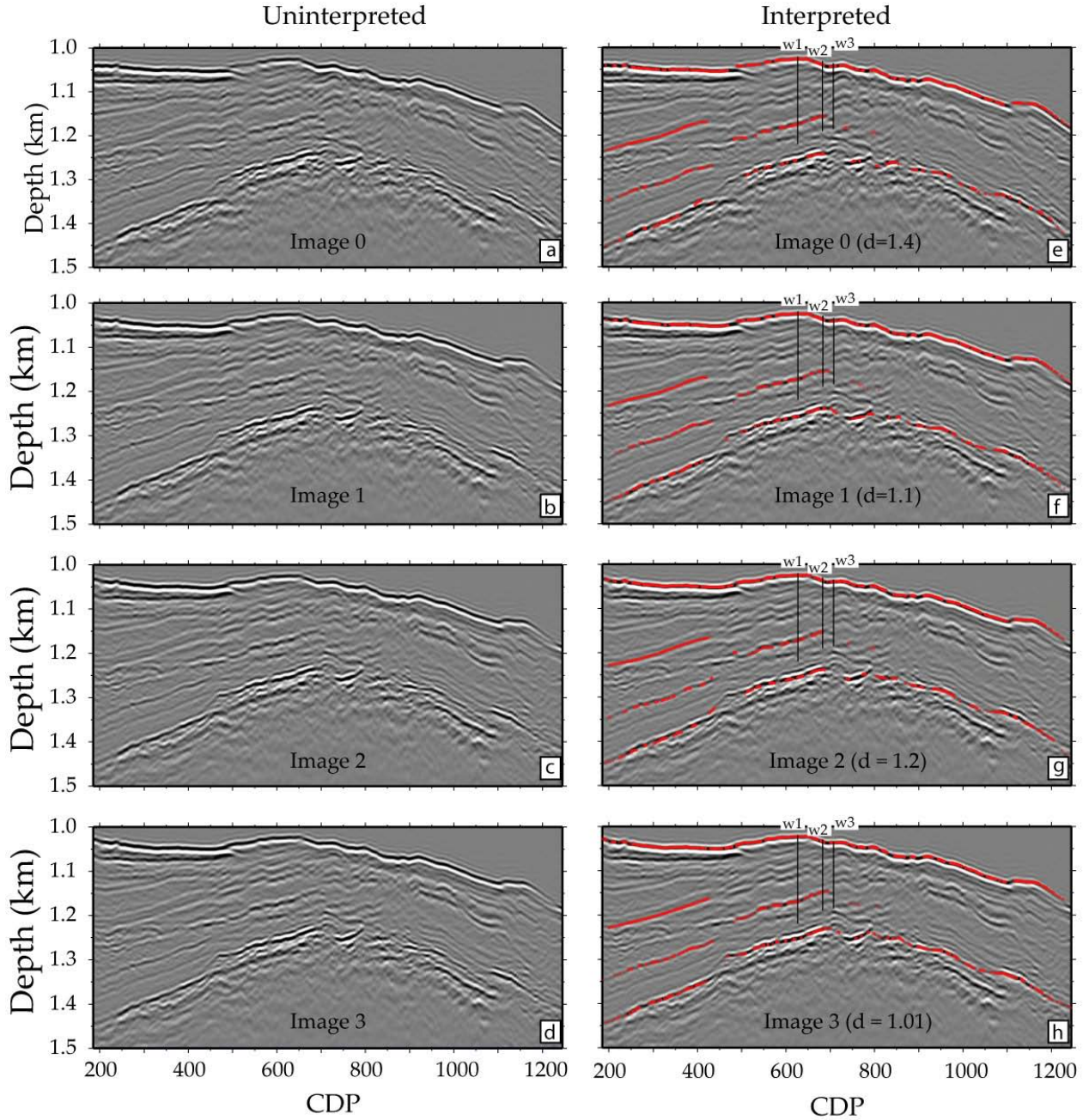


Figure 4. Depth Migrated Image. A) Image0 – D) Image3 are pre-stack depth-migrated reflectivity images using Vel0 – Vel3 velocity models in Figure 2 respectively. E) – H) are same as A) – D) with inverted interface (in red) and well overlaid. In E) – H) d is a parameter for congruency test. Note that Image 3 has the best agreement between observed and inverted interfaces. W1 – W3 are wells 10D, 13A, and 12A respectively.

In UI, the root-mean-square (RMS) distance, d , between the interfaces from the zero-offset inversion and the corresponding interfaces from the interpretation of the depth migrated image;

$$d = \frac{1}{n} \sqrt{\sum_{i=1}^n (z_i^p - z_i^v)^2} \quad (1)$$

In equation (1) z^p and z^v are the interpreted and inverted interfaces and n is the number of nodes at which the interfaces are compared. Due to the limited frequency bandwidth of the depth image and the presence of random and coherent noise, the interpreted horizons in the depth image are

associated with uncertainties. A coefficient of congruence, j , is therefore defined to account for the uncertainties and used as a measurement of the proximity of a given velocity model to the true velocity model;

$$j = \frac{1}{n} \sqrt{\sum_{i=1}^n \left(\frac{z_i^p - z_i^v}{\sigma_i} \right)^2} \quad (2)$$

In equation (2) σ_i is the uncertainty assigned at the i^{th} node (5m in the work). A value of unity for j implies that the structural discrepancies have been fit to the level of the interpretational uncertainties and the unified imaging is said to have converged at this point. Similarly, a value of j greater than unity implies that the velocity model requires improvement and a value less than unity suggests that the data have been overfit.

Unified imaging utilizes [Zelt *et al.*, 2006] method of traveltimes inversion; only a brief overview of the two methods is provided and the readers are guided to the original publication for details. Traveltimes in this method are computed on a regular grid by solving the Eikonal equation using the finite-difference scheme of [Vidale, 1988] modified to account for large velocity gradients [Hole and Zelt, 1995]. Raypaths, in accordance with Fermat's principle, are determined by following the steepest gradient of the time field from a receiver to a source. The inverse modeling part linearizes the non-linear traveltimes inverse problem with the help of an initial model that is iteratively updated based on the discrepancy between the observed and the predicted traveltimes.

The inverse modeling formulates an objective function which is the L_2 norm of a combination of data errors and model roughness (second-order partial derivative) and minimizes it to compute the model updates. For a given observed data vector d_{obs} and predicted data vector d_{pre} , the objective function for simultaneously constraining the velocities and the interfaces is expressed as:

$$E(s, z) = \delta d^T C_d^{-1} \delta d + \lambda \{ \beta [\delta s^T C_{s,h}^{-1} \delta s + s_z \delta s^T C_{s,v}^{-1} \delta s] + (1 - \beta) [\delta z^T C_{z,h}^{-1} \delta z] \} \quad (3)$$

In equations (3) $\delta d = d_{pre} - d_{obs}$ are the data errors and $\delta s = s - s_0$ is the slowness perturbation vector being solved for; s_0 is the starting slowness vector, C_d is the data covariance matrix; covariance matrices $C_{s,h}$ and $C_{s,v}$ measure horizontal and vertical roughness of the slowness perturbation, respectively, λ is the trade-off parameter, and s_z determines the relative importance of maintaining vertical versus horizontal model smoothness. $\delta z = z_0 - z$ is the interface depth perturbation vector being solved for; z_0 is the starting interface vector and $C_{z,h}$ is the covariance matrix that measures the interface roughness. β determines the relative weights of slowness and interface regularizations. Regularization is implemented by scaling with the inverses of the data and model (slowness and interface) space covariance matrices in an attempt to obtain the smoothest model appropriate for the data errors [Scales *et al.*, 1990]. The data misfit in traveltimes inversion is assessed using the normalized form of the misfit parameter, the chi-squared error, χ^2 [Zelt, 1999]. Assuming the errors in the observed picks are uncorrelated and Gaussian in nature, a value of χ^2 equal to 1 indicates that the observed traveltimes have been fit to within their assigned uncertainties.

Due to the inherent velocity-depth tradeoff in the joint inversion, achieving a χ^2 value of unity in every cycle is not the ultimate goal. Instead the overall geological sensibility of the updated velocity model is given more emphasis. The joint inversion is halted when the updates start yielding structures that appear to be geologically implausible even if the convergence has not been reached. For given updates in the velocity model, updates in the corresponding interface depths are sought through PSDM. As the velocity model progressively becomes close to the true velocity model, the migrated image also positions the interfaces closer to their true depth locations. Thus, the non-linear and non-unique nature of unified imaging as a whole calls for close monitoring.

A combination of preferred velocity model (Vel3; Figure 3d) and the corresponding depth image is displayed in Figure 5. Region shaded in blue above the BSR could represent hydrate bearing sediments. The dark blue patch at CDP ~900 coincides with a zone of low reflectivity and could represent concentrated hydrate deposits. The exact character of the resistivity log cannot be explained with the velocity model from UI. It could be partly due to lateral changes in hydrate concentration that do not allow a proper well projection on the seismic line or low resolution of the velocity model itself. The resolution of the velocity model is improved using waveform inversion.

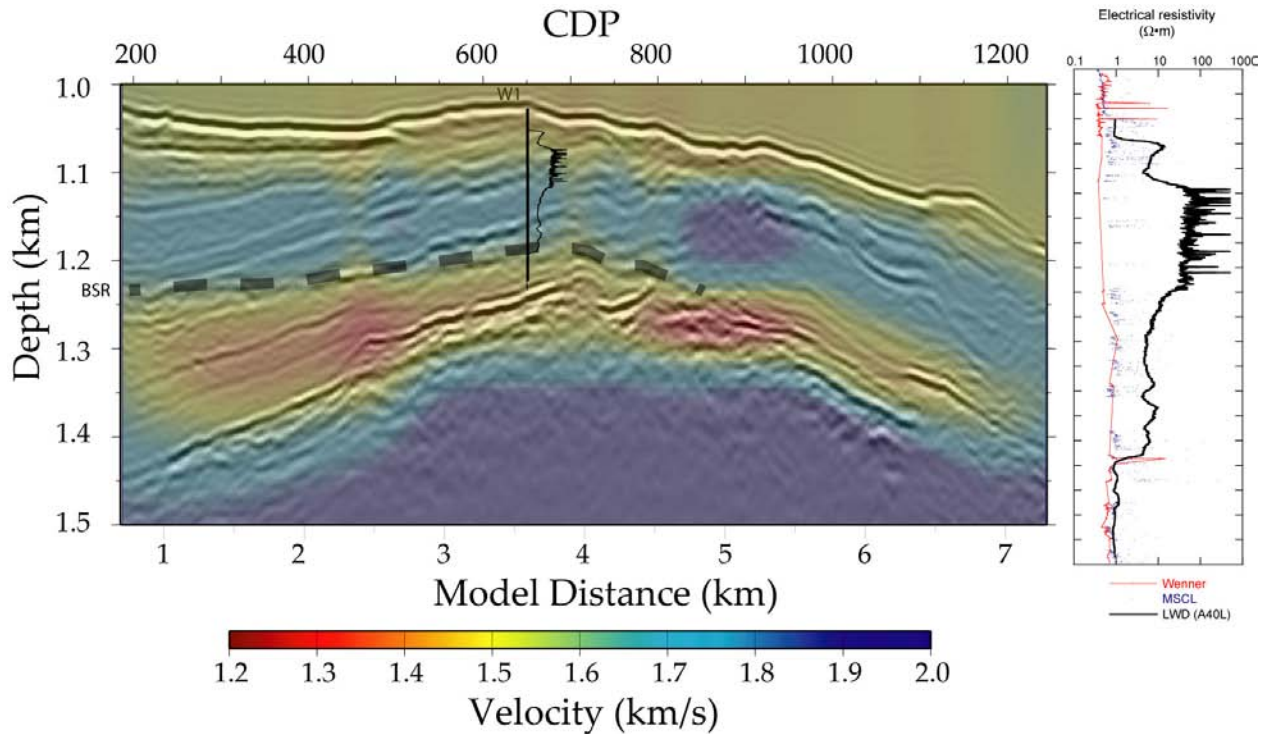


Figure 5. Composite of preferred velocity model and the corresponding depth image from Unified Imaging. BSR is marked in grey dashed line. The resistivity log from 10D is overlaid. The BSR in the log coincides with the BSR in seismic image validating the velocity model. The well log is displayed beside the composite image.

Waveform Inversion

Similar to travelt ime inversion, waveform inversion estimates an earth model that will simulate a seismogram that matches the observed seismogram. In this work, waveform inversion is performed in the frequency domain. This paper uses the [Pratt, 1999] method of waveform inversion. The method begins with an initial guess of the earth model, known as the starting model, and iteratively improves it based on the differences between the predicted and real wavefield, known as the data errors. Model updates in the method are estimated by correlating the back-propagating data residuals with the forward-propagated wavefields. The method operates in the frequency domain. A brief overview of the method is provided here and the reader is guided to the original paper for the complete details.

The wavefield in the forward problem is computed by solving the wave equation in the frequency domain using the finite-difference mixed-grid approach of [Jo et al., 1996]. The wave equation used in the Pratt (1999) method automatically accounts for backscattering and wide-angle effects. For an individual angular frequency ω the wave equation is expressed as:

Error! Bookmark not defined. $\mathbf{d}_{\text{pre}}(\omega) = \mathbf{S}^{-1}(\omega)\mathbf{f}(\omega)$
(4)

In equation (4), \mathbf{d}_{pre} is the complex-valued predicted wavefield vector from the model vector \mathbf{m} , \mathbf{S} is a complex valued impedance matrix that contains information about the physical properties of \mathbf{m} , and \mathbf{f} is the source term vector. In this paper a 2-D acoustic, isotropic approximation of the wave equation is made. Additionally, a relation between density and velocity was estimated from the well logs and attenuation is ignored.

The inverse problem minimizes the L_2 norm of the data errors, expressed in an objective function, E .

$$E(\mathbf{m}) = \frac{1}{2} \delta \mathbf{d}^t \delta \mathbf{d}^* \quad (5)$$

In equation (5), the data errors $\delta \mathbf{d} = \mathbf{d}_{\text{pre}} - \mathbf{d}_{\text{obs}}$ where \mathbf{d}_{obs} is the observed wavefield. In equation (5) \mathbf{d} is a vector comprising strength of the frequency components obtained by a Fourier transform of the time domain data, the superscript t represents matrix transpose, and the superscript $*$ represents the complex conjugate. The Taylor series expansion and simplification of equation (5) in the neighborhood of the model, \mathbf{m} , leads to the following relationship in the k^{th} iteration between the starting, \mathbf{m}^k , and the updated, \mathbf{m}^{k+1} , model:

$$\mathbf{m}^{k+1} = \mathbf{m}^k - \alpha^k \nabla E^k(\mathbf{m}) \quad (6)$$

In equation (6), $\nabla E(\mathbf{m})$ is the gradient direction and α is the step length that is chosen by a line search method. The key in the Pratt (1999) method is to express the gradient direction as:

$$\nabla E(\mathbf{m}) = \frac{\partial E}{\partial \mathbf{m}} = \text{Real}\{\mathbf{F}^t [\mathbf{S}^{-1}]^t \delta \mathbf{d}^*\} \quad (7)$$

In equation (7), \mathbf{F} is known as a virtual source which can be understood as the interaction of the observed wavefield, \mathbf{d}_{obs} , with the perturbations in the model, \mathbf{m} . Individual elements of the virtual source are defined as $\mathbf{f}^i = -\frac{\partial \mathbf{S}}{\partial \mathbf{m}_i} \mathbf{d}_{\text{obs}}$, where \mathbf{f}^i and \mathbf{m}_i are the i^{th} virtual source and model parameter.

Equation (4) is the mathematical expression of the back-propagated residual wavefield, $[\mathbf{S}^{-1}] \delta \mathbf{d}$, being correlated with the forward propagated wavefield, \mathbf{F} . The computational complexity in waveform inversion dominantly rests on the computation of \mathbf{S}^{-1} . For multiple source problems, \mathbf{S}^{-1} is best solved using LU decomposition [Press et al., 1992] and ordering schemes such as nested dissection that take advantage of the sparse nature of \mathbf{S} [Marfurt and Shin, 1989].

Imaging through waveform inversion requires that wavenumbers from zero to the highest value in the data be present in a continuum; the desired resolution dictates the choice of the highest wavenumber and *vice versa*. [Wu and Toksoz, 1987] demonstrated that inversion of a single frequency covers a finite range of wavenumbers. Following their results, [Sirgue and Pratt, 2004] demonstrated that inverting a few carefully chosen frequencies is equivalent to inverting all frequencies available in the seismic survey; they referred to the strategy as efficient waveform inversion. We have used a similar strategy to determine groups of frequencies (Table 1) that can be inverted to image the required range of wavenumbers.

Group	Frequencies (Hz)
1	8, 8.4, 8.8
2	9.6, 10.0, 10.4
3	11.2, 11.6, 12.0

4	12.8, 13.2, 13.6
5	14.8, 15.2, 15.6

Table1. frequency groups used for waveform inversion.

Waveform inversion also requires a source function to compute the model updates. The Pratt (1999) method estimates the source function with the help of the current model. Thus, waveform inversion begins not only with a starting model but also a starting source signature. For a given data bandwidth, the velocity model is updated using the *a priori* source signature, following which the source signature is updated using the updated velocity model. As waveform inversion iteratively incorporates higher wavenumbers, higher frequencies are incorporated in the source signature and the resolution of the recovered model is enhanced.

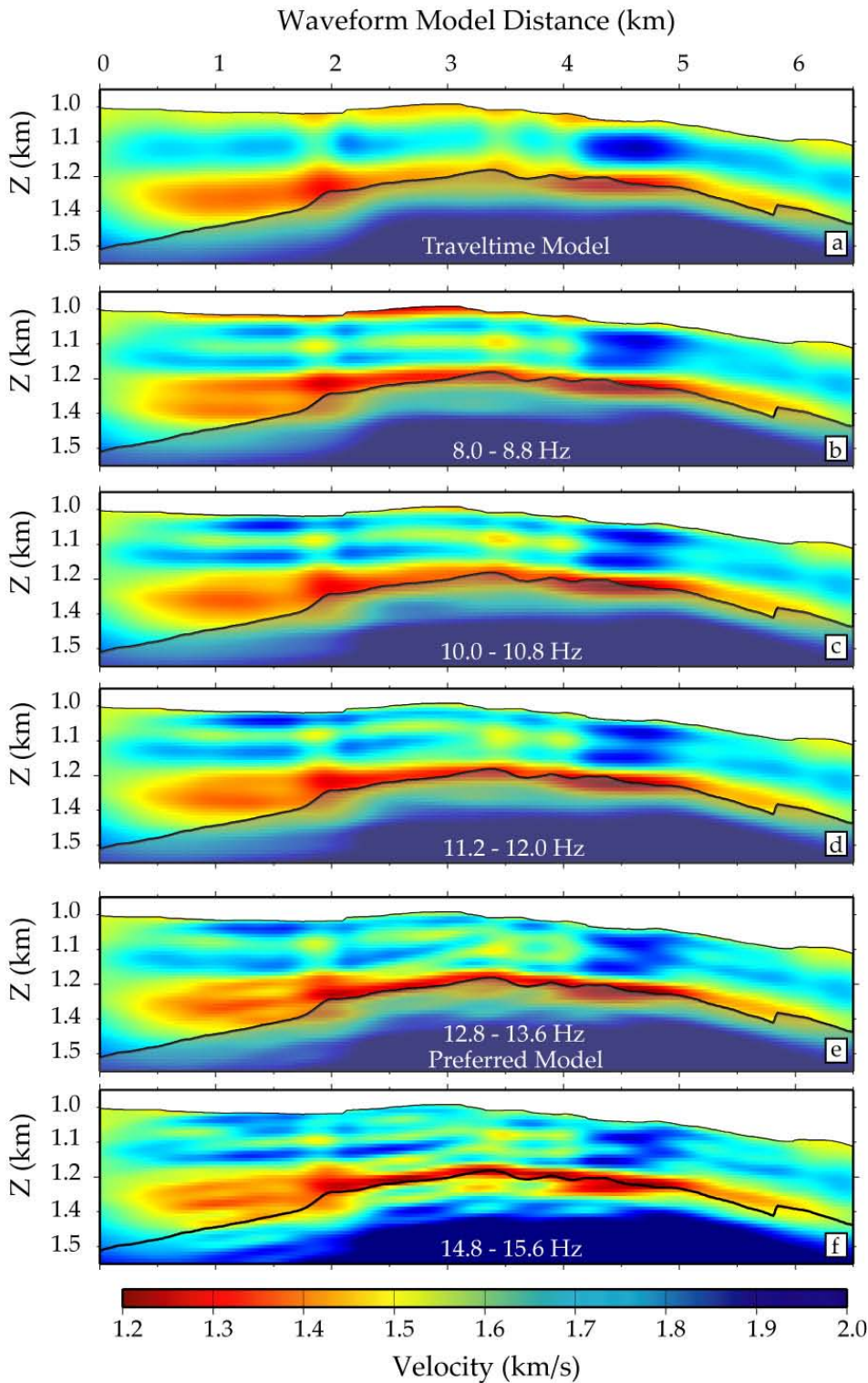


Figure 6. Models from waveform inversion. Model from inversion of 12.8 – 13.6 Hz is chosen as the preferred model.

The waveform inversion started with the preferred velocity model from UI (Figure 3d) as the starting model. The UI model was spatially windowed so as to include on the best resolved parts; resolution was determined using checkerboard tests. As a first step a source wavelet was estimated following which the lowest frequency group (Group1; Table 1) was inverted. A new source was estimated using the inverted model and the process was repeated with 4 groups of frequencies (Figure 6) until data artifacts started contaminating the model (Figure 6e). At this point waveform inversion was halted and a preferred model was selected (Figure 6d) based on its overall geological reasonability.

The preferred waveform model (Figure 6d) is jointly interpreted with the depth image (Figure 7). The composite image suggests that in parts of the model between CDPs 500 and 900 a) hydrates prefer

certain stratigraphic sections; and b) some parts appear to be hydrate-free. The reasons behind variation of hydrate concentration are currently under investigation. Further, we have not accounted for fault in our interpretation. However, it can be concluded that waveform inversion has provided deeper insight into the hydrate distribution along the seismic line. It also appears that the variation of hydrates within well 10D can be better explained with the waveform model.

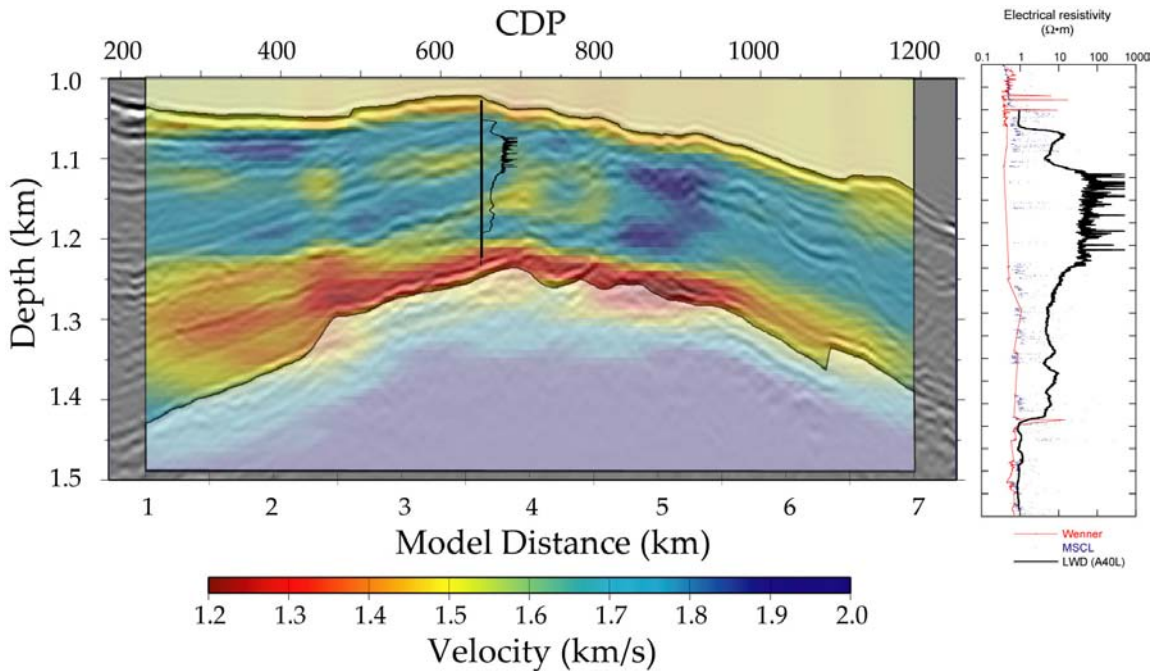


Figure 7. Composite of the preferred waveform model and preferred depth image. Interpretation and reconciliation with the wells logs is in progress. For clarity part of the model not included in waveform inversion is covered with transparent white.

Ongoing work:

Improvement of waveform model is in progress. Future plans are to invert for attenuation as well. Following aspects regarding interpretation are under investigation:

1. Why do hydrate show preferred orientation below the structurally deformed part of the seafloor?
2. Can fracture zones (not interpreted) and fluid flow give hydrate a preferred orientation?
3. Are hydrate re-precipitated, and if so, is it as a result of structural deformation?

References:

- Dix, C. H. (1955), Seismic velocities from surface measurements., *Geophysics*, 20, 68 - 86
- Hole, J. A., and B. C. Zelt (1995), 3D finite-difference reflection traveltimes, *Geophysical Journal International* 121, 427-434
- Jaiswal, P., and C. A. Zelt (2008), Unified Imaging of Multichannel Seismic Data: Combining Traveltime Inversion and Pre-Stack Depth Migration, *Geophysics*, 73, DOI: 10.1190/1.2957761
- Jo, C.-H., C. Shin, and J. H. Suh (1996), An optimal 9-point, finite-difference, frequency-space, 2-D scalar wave extrapolator, *Geophysics*, 61(2), 529-537
- Marfurt, K. J., and C. S. Shin (1989), *The future of iterative modeling of geophysical exploration*, Livrenoir, Brooklyn, NY.
- Pratt, R. G. (1999), Seismic waveform inversion in the frequency domain, Part 1: Theory and verification in a physical scale model, *Geophysics*, 64(3), 888-901
- Press, W. H., S. A. Teukolsky, W. T. Vetterling, and B. P. Flannery (1992), *Numerical Recipes in C : the art of scientific computing*, 2nd ed., University Press.
- Scales, J. A., P. Docherty, and A. Gersztenkorn (1990), Regularization of nonlinear inverse problems-imaging the near-surface weathering layer, *Inverse Problems*, 6, 115-131
- Sirgue, L., and R. G. Pratt (2004), Efficient waveform inversion and imaging: A strategy for selecting temporal frequencies, *Geophysics*, 69(1), 231-248
- Vidale, J. (1988), Finite-difference travel time calculation, *Bull. Seism. Soc. Am.*, 78(8), 2062-2076
- Wu, R.-S., and M. N. Toksoz (1987), Diffraction tomography and multisource holography applied to seismic imaging, *Geophysics*, 52(1), 11-25
- Zelt, C. A. (1999), Modelling strategies and model assessment for wide-angle seismic traveltimes data, *Geophysical Journal International*, 139(1), 183-204
- Zelt, C. A., R. M. Ellis, and B. C. Zelt (2006), Three-dimensional structure across the Tintina strike-slip fault, northern Canadian Cordillera, from seismic refraction and reflection tomography, *Geophysical Journal International*, 167(3), 1292-1308, 10.1111/j.1365-246X.2006.03090.x

COST PLAN / STATUS

DOE Grants R15620, RO15621, RO15622
11/3/2010

COST PLAN / STATUS	Phase 1	Phase 2	Phase 3	Phase 4	Deobligation	Phase 5	Project Total
Phase	10/06-6/07	7/07-6/08	7/08-6/09	Totals 7/01/09- 7/16/10		7/17/10 – 7/16/11	
Baseline Cost Plan Allocation							
Federal Share	\$ 3,624	\$320,010	\$ 331,135	\$ 356,049	\$ (109,098)	\$259,335	\$ 1,161,055
Non-Federal Share	\$ 1,004	\$114,613	\$ 107,630	\$ 110,489	\$ 23,415	\$114,363	\$ 471,514
Total Planned	\$ 4,628	\$434,623	\$ 438,765	\$ 466,538	\$ (85,683)	\$373,698	\$ 1,632,569
Cumulative Baseline Cost	\$ 4,628	\$439,251	\$ 878,016	\$ 1,344,554	\$ 1,258,871	\$1,632,569	
Actual Incurred Cost							
Federal Share	\$ 3,082	\$295,415	\$ 249,125	\$ 354,098			
Non-Federal Share	\$ 1,091	\$117,053	\$ 96,346	\$ 155,580			
Total Incurred	\$ 4,173	\$412,468	\$ 345,471	\$ 509,678			
Cumulative Costs	\$ 4,173	\$416,641	\$ 762,112	\$ 1,271,790			
Variance (plan-actual)							
Federal Share	\$ 542	\$ 24,595	\$ 82,010	\$ 1,951	\$ (109,098)		
Non-Federal Share	\$ (87)	\$ (2,440)	\$ 11,284	\$ (45,091)	\$ 23,415		
Total Variance	\$ 455	\$ 22,155	\$ 93,294	\$ (43,140)	\$ (85,683)		
Cumulative Variance	\$ 455	\$ 22,610	\$ 115,904	\$ 72,764			

Milestone Plan/Status

Task	Milestone: Status and Results	Date	Status
5. Carbon inputs and outputs to gas hydrate systems	5.1a Measure iodine in sediments We have measured iodine concentrations in pore waters and sediments from 4 gas hydrate systems.	12/07	Done (except writing)
	5.1b Constrain C_{org} inputs from iodine We have measured the content and isotopic composition of organic carbon and carbonate in sediment from cores of several gas hydrate systems. We are beginning to incorporate the results into models.	10/08	Partly Done
	5.2a Construct metal profiles in sediments We have measured metal contents in pore water and sediment from cores of two gas hydrate systems along the Peru Margin and in the Sea of Japan. The Sea of Japan work has been published (Snyder et al., 2007).	12/09	Done (except writing)
	5.2b Modeling/integrating profiles We are beginning to incorporate the results into models. We have written an article defending our use of the SMT as a proxy for methane loss through AOM.	12/10	Begun

6. Numerical models for quantification of hydrate and free gas accumulations	6.1 Model development. The recipient shall develop finite difference models for the accumulation of gas hydrate and free gas in natural sediment sequences on geologically relevant time scales.	9/07	Done
	6.2: Conditions for existence of gas hydrate The recipient shall summarize, quantitatively, the	3/07	Done

	conditions for the absence, presence, and distribution of gas hydrates and free gas in 1-D systems by expressing the conditions in terms of dimensionless groups that combine thermodynamic, biological and lithologic transformation, and transport parameters.		
	<p>6.3 Compositional effect on BSR</p> <p>The recipient shall add to the numerical model, developed under this task, multi-hydrocarbon capability specifically to investigate how existence of multi-hydrocarbon components might affect Bottom Simulating Reflectors (BSRs).</p>	7/07 (new: 6/11)	Simple case done (writing manuscript); complex cases on going
	<p>6.4: Amplitude Attenuation and chaotic zones due to hydrate distribution</p> <p>The recipient shall simulate preferential formation of gas hydrate in coarse-grained, porous sediment in 1-D and 2-D by linking fluid flux to the permeability distribution and evolution.</p>	3/09 (new: 6/11)	ongoing
	<p>6.5: Processes leading to overpressure</p> <p>The recipient shall quantify, by simulation and summarize by combination of responsible dimensionless groups, the conditions leading to overpressure to the point of sediment failure.</p>	3/08 (new: 6/11)	1D written and published; 2D near completion and need to write results (Collaborating with task 8)
	<p>6.6 Concentrated hydrate and free gas</p> <p>The recipient shall, using 2-D models, simulate lateral migration and concentration of gas hydrate and free gas in structural and stratigraphic traps.</p>	3/08 (new: 6/11)	Ongoing; one manuscript in press (Daigle et al.)

	<p>6.7 Focused free gas, heat and salinity</p> <p>The recipient shall quantify, using 1-D and 2-D model simulations and comparisons to available observations, the factors controlling the process of localized upward migration of free gas along faults and lateral transfer to dipping strata that can lead to chaotic zones and possible accumulations of concentrated hydrate.</p>	9/09 (new: 6/11)	Ongoing case studies, models work and general results near submission
	<p>6.8a Sulfate profile as indicator of methane flux</p> <p>The recipient shall compute, for systems where data on the sulfate profile is available, the oxidation of methane by sulfate and shall indicate the perceived level of effect on gas hydrate accumulation and the data's value as an indicator of methane flux.</p>	7/07	Done, and published
	<p>6.8b Carbon cycling across SMT above marine gas hydrate systems.</p> <p>The recipient shall compute, for systems where data on the sulfate, bicarbonate (DIC), calcium, carbon isotope profiles are available, the reduction of sulfate by methane and by particulate organic carbon and shall indicate the perceived level of effect on gas hydrate accumulation and the depth to the SMT as an indicator of methane flux.</p>	6/10	Done, finalizing manuscript for submission
	<p>6.9 Application of models to interpretation of case studies.</p> <p>The models developed in Task 6 will be applied to case studies in the interpretation of each of the other tasks.</p>	6/11	Started and working 2D system, manuscripts should be submitted by 06/11
7. Analysis of production strategy	<p>7.1a Pore scale model development and Hydrate code comparison</p> <p>For this milestone, we will develop pore-scale models of hydrate accumulation by simulation. Our hydrate code will be used to solve a set of problems formulated by the</p>	1/08	6/08 This task is complete

	<p>Code Comparison Study group. Our results will be compared with those of other hydrate codes.</p> <p>Should be changed to: 6/08 Reason: The starting date was moved to 6/07 Status: Code comparison study is 100% complete.</p>		
	<p>7.1b Petrophysical and thermophysical properties of hydrate sediments from pore-scale model</p> <p>For this milestone, we will assume the pore-scale models of hydrate accumulation developed in the last milestone and estimate transport properties as a function of hydrate and gas saturations.</p> <p>Should be changed to: 6/09 Reason: The starting date was moved to 6/07</p>	1/09	<p>6/09</p> <p>This task is complete</p>
	<p>7.2a Modeling of several production strategies to recover gas from marine hydrates</p> <p>Several production strategies would be modelled using the transport property correlations developed in the previous milestone. Optimal strategies will be identified.</p> <p>Should be changed to: 6/10</p>	6/10	<p>7/10</p> <p>This task is complete</p>
	<p>7.2b Effect of marine reservoir heterogeneities on production of methane</p> <p>Reservoir heterogeneity anticipated in marine environments (known or determined through other tasks) would be incorporated. Appropriate hydrate distributions, either constrained from experimental data or mechanistic simulations (Task 5) would be used. Sensitivity of gas production to the heterogeneities would be calculated.</p> <p>Should be changed to: 6/11 Reason: The starting date was moved to 6/07 Status: Have not started</p>	6/11	<p>On schedule</p>
8. Seafloor and borehole stability	<p>8.1a Collection of data</p> <p>We have collected the published data and are working it into a data base. We are also working on a review paper summarizing the state of the art settings. This will include laboratory experiments, field data, published results, and unpublished data.</p>	05/08	<p>Completed</p>
	<p>8.1c Complete database</p>	6/10	<p>Done</p>

	<p>We are organizing the data from task 8.1a into a format that can be searched and used by researchers trying to understand mechanical behavior of hydrate-bearing sediment. We will also identify key gaps in the database for focusing future hydrate research endeavors. We have started exchanging these data with the modeling components of this project.</p>		
	<p>8.2a Link database with models</p> <p>We have started passing data along to the modeling groups so they can use sediment properties from hydrate provinces as they simulate hydrate accumulation and production.</p>	6/11	Done, by 6/11 will be done with very high permeability contrasts
	<p>8.2b Add sediment stability to models</p> <p>Standard stability calculations have been implemented in a standard basin model. Now that it is functional we will work with the hydrate accumulation model to add a stability calculation to the 2-D models.</p>	6/10	Done
	<p>8.2c Conditions for (in)stability</p> <p>After implementing the stability model in the hydrate accumulation code, we can explore the conditions (e.g., hydrate dissociation, sea-level fall) that could drive slope failure and hydrate/methane release or lead to borehole failures during production.</p>	6/11	Ongoing, and will have general and case studies by 06/11
9 Geophysical imaging of hydrate and free gas	<p>9.1 Preliminary processing and inversion of seismic data.</p> <p>Perform conventional seismic reflection processing, velocity analysis, travel time tomography, and other analyses as deemed appropriate and necessary.</p>	8/08	Done Article in progress.
	<p>9.2: Final 1-D elastic and 2-D acoustic waveform inversion.</p> <p>Apply 1-D elastic and 2D acoustic inversions on data obtained from subtask 9.1 to derive determine high-resolution elastic and acoustic properties.</p>	8/09	Ongoing. Results expected by December 2010.
	<p>9.3: Rock physics modeling.</p> <p>Apply rock physics models to the developed seismic</p>	8/10	Begun

	<p>models to estimate hydrate saturation and lithology through application of well log data in conjunction with data from subtask 9.2. For this subtask we shall seek to collaborate with research being conducted under separately funded DOE-NETL projects (DE-FC26-05NT42663 with Stanford University, "Seismic-Scale Rock Physics of Methane Hydrate" and others as applicable).</p>		
--	--	--	--

National Energy Technology Laboratory

626 Cochrans Mill Road
P.O. Box 10940
Pittsburgh, PA 15236-0940

3610 Collins Ferry Road
P.O. Box 880
Morgantown, WV 26507-0880

One West Third Street, Suite 1400
Tulsa, OK 74103-3519

1450 Queen Avenue SW
Albany, OR 97321-2198

539 Duckering Bldg./UAF Campus
P.O. Box 750172
Fairbanks, AK 99775-0172

Visit the NETL website at:
www.netl.doe.gov

Customer Service:
1-800-553-7681

